The structure of ^{20}C using proton removal reactions

Liam Gawan Atkins

Doctor of Philosophy

University of York
Physics, Engineering and Technology

August 2022

Abstract

The carbon isotopic chain is accessible experimentally up to the neutron drip line and provides a unique opportunity to study the evolution of shell structure with isospin asymmetry. Of particular interest is the proton component of the 2^+ state along the carbon isotopic chain, which can shed light to the evolution of the Z=6 spin-orbit shell gap. The bound state of ^{20}C, following a proton knockout reaction from a ^{21}N beam can yield information on the proton component of the first 2^+ state. The experiment was performed at RIKEN during the Day-One campaign and the SAMURAI setup is used to measure the inclusive and exclusive cross section of the bound 2^+ state from the $C\left(^{21}N,^{20}C\right)X$ reaction.

The model used to interpret the results describes the excited 2^+ state in terms of a mixing of pure proton and pure neutron excitation, where the proton amplitude is a measure of the amount of proton excitation. Following a proton removal reaction from ^{21}N which populates both the ground and excited 2^+ state in ^{20}C, the proton amplitude was determined by measuring the inclusive cross section and exclusive cross section of the 2^+ state.

Previous work has shown the existence of the Z=6 sub-shell closure, with evidence suggesting a weakening of the sub-shell closure as the neutron drip line is approached because of a reduction in the splitting of the $1p_{1/2}$ and $1p_{3/2}$ proton orbits. The deduced proton amplitude of $\beta^2 = 13.73 \pm 1.16_{(stat)} \pm 0.26_{(sys)}$% shows that the amount of proton excitation of the first excited 2^+ state in ^{20}C is moderately increased. This value represents a moderate increase when compared to the proton amplitude of lighter neutron rich even-even ^{16,18}C, supporting the previous work suggesting a weakening of the Z=6 sub-shell closure. This thesis presents the analysis of the data obtained during the Day-One campaign at SAMURAI.

Acknowledgements

I would first like to thank my supervisors, Dr. Marina Petri and Dr. Stefanos Paschalis for the opportunity to work on this project. I would also like to express my gratitude for their supervision and guidance over the past four years. I would also like to give an extra thanks to Dr. Stefanos Paschalis for running a summer project on muon tomography during my undergrad, which set me down the path of nuclear physics.

I would also like to give my thanks to my collaborators, Dr. Nigel Orr and Prof. Julien Gibelin at LPC Caen. The opportunity to visit them at LPC Caen was a great start to the project. I would also like to thank them for their discussion and support at various parts of the project.

A huge thanks goes to Dr. Ryo Taniuchi for his support with the analysis, his expertise with the RIKEN analysis code along with discussions of the analysis was invaluable. I would also like to thank my friends and colleagues at York and LPC Caen for their discussions over the course of this research project.

Finally, I would like to give my huge appreciation to Emma, for her unwavering support throughout this project. A huge thanks also goes to my Mum and Dad, and to Carenza for their support over the years, both in this research project, and at all previous stages. Thank you very much to everyone.

Declaration

I declare that this thesis is a presentation of original work and I am the sole author. This work has not previously been presented for a degree or other qualification at this University or elsewhere. All sources are acknowledged as references.

Contents

List of Figures

List of Tables

Chapter 1

Introduction

1.1 The nuclear shell model

Nuclear physicists have tried to understand the way a nucleus is constructed. An early primitive model of an atom, described in 1904 by J. J. Thompson [1], was the plum pudding model. The plum pudding model takes the knowledge that atoms are neutrally charged, and that electrons are negatively charged particles. To account for this, the plum pudding model describes an atom as electronsmoving in a volume of positive charge. However, this model predates the discovery of the proton and neutron. Further, the α scattering experiment, performed by Ernest Rutherford , and named after him, in 1911, determined that the plum pudding model could not explain the large scattering angles of α particles. The conclusion was that the atom was better described as a minute nucleus, that contains most of the mass, and is positively charged, surrounded by the negatively charged electrons [2], where the number of electrons must be equal to the charge of the nucleus. The observation by Rutherford in 1919 [3] that the firing of α particles into air (which is mostly comprised of nitrogen), and then later into pure nitrogen resulted in the emission of "hydrogen atoms", actually protons, is attributed to the discovery of the proton. It is also the first reported nuclear reaction, ^{14}N(α,p)^{17}O. In 1920, Rutherford proposed the existence of a neutrally charged particle [4], composed of a bound proton and electron in order to account for the emission of electrons (β radiation) from the nucleus. It was noted however that this description of a possible neutron composition did not satisfy the basic principles of quantum mechanics, so a different explanation of the neutron was necessary. The observation by Walter Bothe and Herbert Becker in 1931 [5] of the emission of an unusually penetrating radiation when α particles fell on elements such as polonium was initially explained as γ radiation due to the observation of it not being influenced by electric fields. However this was not a satisfactory explanation, and the observation of the emission of protons when the new radiation fell on hydrogen bearing materials such as paraffin added to the suspicion that the new radiation was not γ

radiation. A series of experiments by James Chadwick [6] determined that the new radiation was composed of a particle with no charge, and a mass similar to the mass of a proton, which are neutrons.

The shell model, as used in atomic physics, was applied to the nucleus in an attempt to describe the ordering of nucleons. In the atomic shell model, orbitals are filled with electrons in shells with increasing energy and in a way that is consistent with the Pauli exclusion principle. As a result, smooth changes are seen as orbitals are filled, with abrupt changes seen when entering a new shell. In nuclear physics, evidence for this shell model is seen with the magic numbers. The magic numbers have Z or N=2,8,20,28,50,82,126 (although as will be discussed later, the addition of protons and neutrons can lead to the formation of new shell gaps, otherwise known as magic numbers). When these magic numbers are reached, a sudden discontinuous behaviour is observed in various nuclear observables, such as the separation energies, large excitation energies of the first excited state, enhanced abundances of nuclei with shell closures and near zero electric quadrupole moments [7].

In the nuclear shell model, the potential is caused by the other nucleons, and within the shell, nucleons are transparent to one another. This is an example of the Pauli exclusion principle, where two fermions cannot occupy the same quantum state. The energy of a collision is relatively low, and if there are no nearby unfilled quantum states (holes) then the collision will not occur, and the nucleons are therefore transparent to one another [7]. In the shell model, states have a degeneracy of $2(2l+1)$, however this can vary depending on the model. The earliest potentials investigated were the infinite square well and the harmonic oscillator. These basic models for the potential give the early magic numbers 2,8 and 20, but fail with higher magic numbers. In the case of the harmonic oscillator, this is due to the degeneracy being determined by (n+1)(n+2), where n is the principle quantum number, representing the level. The harmonic oscillator potential correctly predicts the early magic numbers (2,8,20), but fails above this point. The harmonic oscillator potential at a given radius is given by equation 1.1.

$$V(r) = \frac{1}{2} m\omega^2 r^2 \tag{1.1}$$

Where m is the mass, ω is the harmonic oscillator frequency and r is the distance. These models do not perform well as they are unrealistic potentials which do not replicate the nucleus. A better description of the nuclear potential is the Woods-Saxon potential [8], shown in equation 1.2.

$$V_0(r) = \frac{-V_0}{1 + exp[\frac{r-R}{a}]} \tag{1.2}$$

The Woods-Saxon model is a better representation of the nuclear potential because it

contains real information of the nucleus, where R is the radius of a nuclei, given by equation 1.3.

$$R = 1.25A^{1/3}\ fm \tag{1.3}$$

Where A is the mass number of the nucleus. The Woods-Saxon model also gives the diffusivity, a = 0.524 fm, which represents the surface thickness, and is defined as the distance over which the charge density falls from 90% to 10% [7]. This value is not the same for each nuclei, and will be larger for nuclei with a larger number of neutrons. The potential depth, V_0 is chosen to be realistic, with a depth of ~50 MeV. Using the Woods-Saxon model however, the magic numbers above 20 are once again not predicted. The Woods-Saxon model is already a good estimate of the potential as it contains physical information of the nucleus, therefore modifications of the potential were investigated in order to reproduce the higher magic numbers.

The correction that was needed was the spin-orbit potential, proposed by Mayer and Haxel in 1949 [9] Adding the spin orbit term splits the existing levels into two different levels, with $j = l + \frac{1}{2}$ and $j = l - \frac{1}{2}$. Each of these states can then be filled with $2j + 1$ protons or neutrons. It is also necessary to include the Coulomb potential. By including the spin-orbit potential, the shell model now predicts the correct magic numbers. It is possible to describe the potential of a nucleus that is near to a closed shell using equation 1.4 [7].

$$V(r) = V_0(r) + V_{ls}(r)\,l.s + V_C(r) \tag{1.4}$$

In equation 1.4, V_0(r) is the Woods-Saxon potential, $V_{ls}(r)$ is the spin orbit potential, and $V_C(r)$ is the Coulomb potential. The evolution of the different models, resulting in the correct magic numbers is shown in figure 1.1. However, this model does not hold up for nuclei far away from closed shells, such as ^{20}C.

1.2 States in a nucleus

1.2.1 The ground state

The ground state of a nucleus is the lowest energy at which the nucleus can be. It is described by the spin and parity that nucleons are in. In any nuclei, completely full, closed shells form inert cores that do not contribute to the behaviour of the nucleus. In shells that aren't closed, nucleons pair together with equal and opposite angular momentum vectors. Therefore in the case of even-even nuclei, the ground state is $J^\pi = 0^+$. This is relevant in the case of ^{20}C, which is an even-even nucleus.

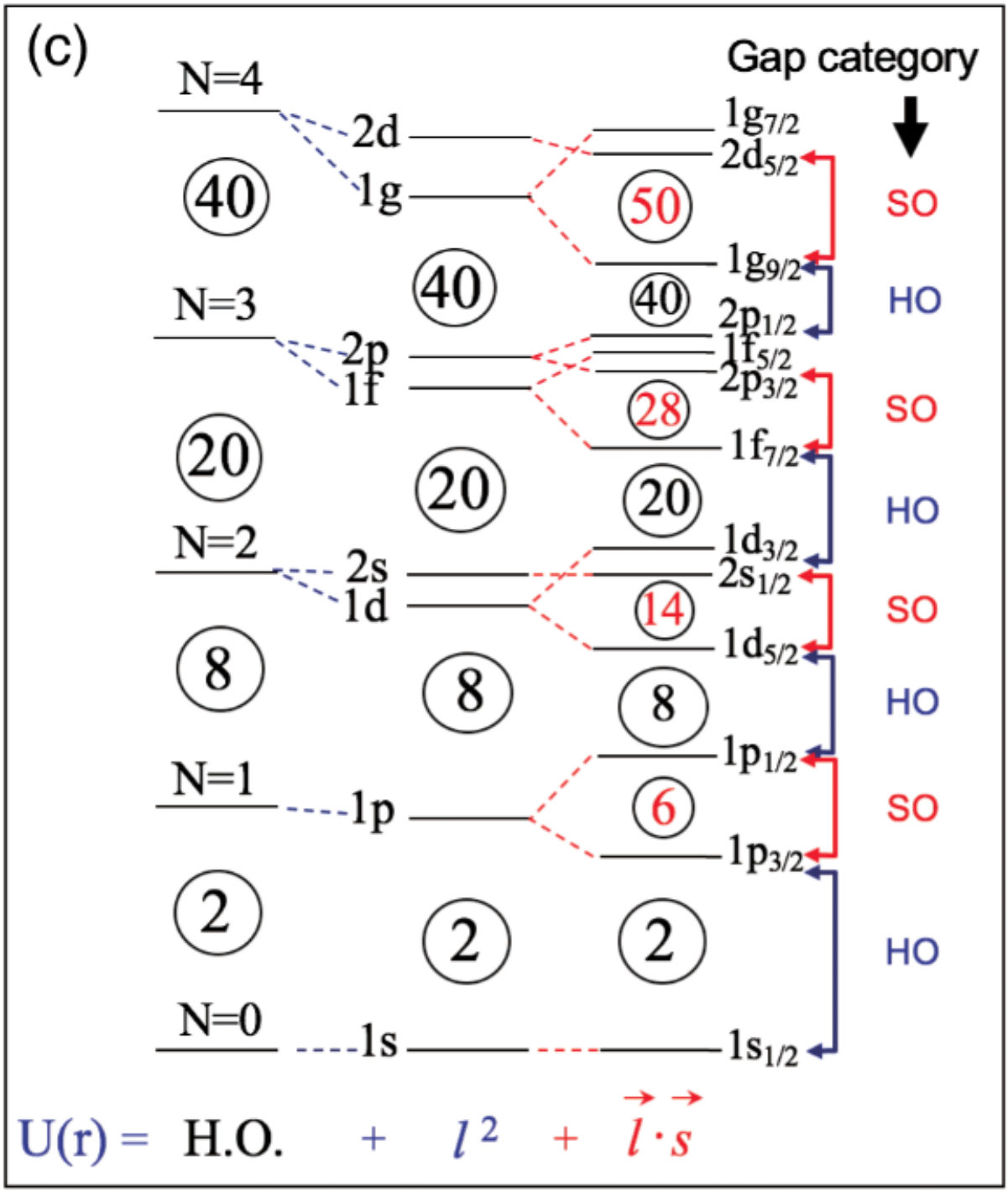

Figure 1.1: On the left shows an attempt at deriving the magic numbers using a harmonic oscillator potential, in the middle, the effect of the orbital angular momentum is added, and on the right, the effect of the spin orbit term can be seen to split the levels, and recreate the magic numbers. Of note are the relatively large energy gaps seen when the spin orbit term is introduced, such as 6 and 14. This figure was adopted from[10].

For odd-A nuclei, the ground state is described by the spin and parity of the valence nucleon. Therefore the ground state of a nucleus with an odd nucleon in the $d_{5/2}$ state would be $J^{\pi} = \frac{5}{2}^{+}$. The parity is given by $\pi = (-1)^{l}$ and for the d orbital, $l = 2$, therefore $\pi = 1$ so the parity is positive (+).

In the case of odd-odd nuclei, there will always be an unpaired proton and neutron. In this case, the allowed spin values are a combination of the odd protons and odd neutrons angular momentum, which is given in equation 1.5.

$$J = (j_p + j_n), ..., |j_p - j_n| \tag{1.5}$$

The parity of the state is determined using equation 1.6.

$$\pi = \pi_p \times \pi_n \tag{1.6}$$

1.2.2 Bound excited states

An excited state in the nucleus is a configuration where the energy of the nucleus is greater than the ground state. As shown in figure 1.2, this can occur when one or more nucleons are excited from the ground state configuration to a higher energy level. This can happen when an odd (valence) nucleon is excited, or by breaking a pair and exciting one of the nucleons to a higher energy level. When this happens, the state is described by the spin and parity of the nucleon in its new level. When a pair is broken, it is possible that the excited nucleon will then form a pair with an odd nucleon in a higher shell. This will result in a closed, inert pair and an odd nucleon left behind from the original pair.

It is also possible that the nucleon from a broken pair will go to a higher energy level than any odd nucleon, this will result in multiple odd particles. When this happens, the maximum spin is the sum of the angular momentum vectors of the odd nucleons. The minimum spin is the modulus of the different angular momentum vectors subtracted from one another, similar to equation 1.5. The spin values are then in steps of one between the maximum and minimum possible values.

A further way of generating excited states in even-even nuclei does not involve breaking a pair. Instead it can be explained by collective structure. It typically takes approximately 2 MeV to break a pair [7], however in all even-even nuclei in the entire mass range, a 2^{+} state is seen at approximately half the energy required to break a pair. An example of this, as discussed in Introductory Nuclear Physics by Krane [7] is ^{130}Sn. This is explained as the result of a collective excitation of the entire nucleus. Collective excitation of the nucleus can be split into two major types, vibrational and rotational. These two types of excitation occur at different regions as shown by figure 1.3 by plotting mass against the ratio of the

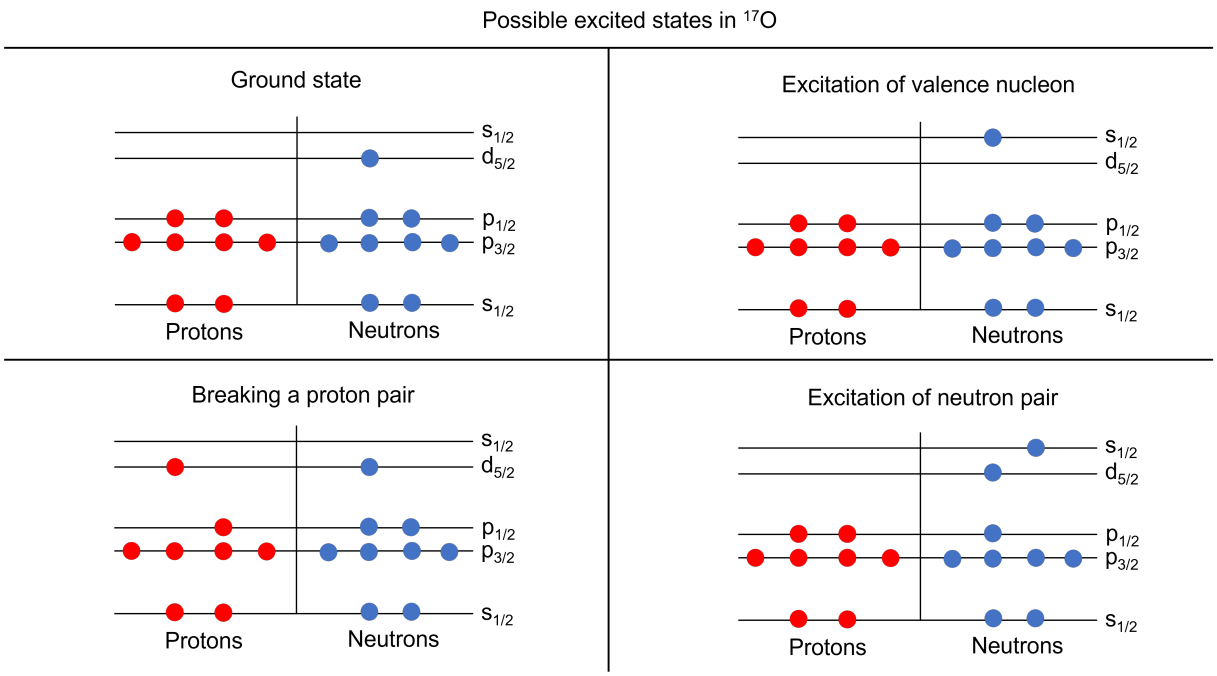

Figure 1.2: A sketch showing the ground state and different ways of exciting the ^{17}O nucleus. In ^{17}O, it is possible to excite the nucleus by exciting the valence neutron, or by breaking a proton or neutron pair, and exciting one of the nucleons from the broken pair.

excitation energy of the 4^+ to 2^+ state, determined using equation 1.7, where J is the moment of inertia, and I is the angular momentum quantum number. The first region, seen with A<150 can be described by vibrations of the nucleus, while nuclei with 150<A<190 and A>230 have $E(4^+)/E2^+$ values a little over three which can be described by rotation of the nucleus.

$$E = \frac{\hbar^2}{2J} I(I+1) \tag{1.7}$$

In order to explain these collective excitations, the nucleus can be thought of as a liquid drop, where the average shape of a nucleus is spherical. The addition of a unit of vibrational energy, called a phonon results in the vibration of the nucleus. The addition of a single unit of λ=2 nuclear vibration, a quadrupole phonon, results in quadrupole deformation. This state must observe spin and parity, just like a state formed by the breaking of a pair of nucleons. In general, although there are exceptions such as the cadmium chain, the addition of these two units of angular momentum to the 0^+ ground state of an even-even nucleus results in the production of a 2^+ state, which is the first observed 2^+ state with an energy of approximately half of the 2 MeV required to break a pair. It is possible that more than one phonon will be added to the nucleus, resulting in other states being produced.

In the case of nuclear rotations, in order to observe an excited state, the nucleus must be non spherical so that it has a preferred axis. Nuclear rotations are seen in nuclei with 150<A<190 and A>230, these nuclei are mid-shell and have substantial deformation which

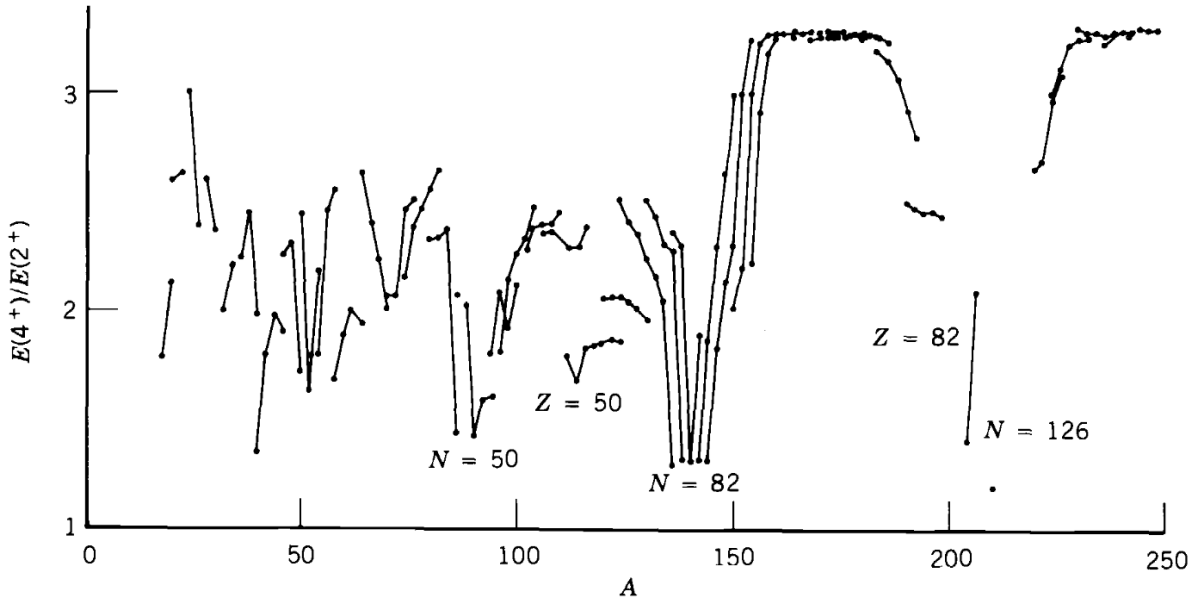

Figure 1.3: The ratio of $E(4^+)/E(2^+)$ for even-even nuclei is shown. Nuclei with A<150 show a ratio of approximately two. In this region, the collective excitation can be described by vibrations of the nucleus. Nuclei with 150<A<190 and A>230 have a ratio a little over three. For these nuclei, the collective excitation is described as rotations of the nucleus. This figure was adopted from [7].

can allow for rotations. For these even-even nuclei, the addition of rotational energy (increasing I, the angular momentum quantum number) forms a sequence of excited states, known as a rotational band. The sequence of states is given by equation 1.7.

1.2.3 Binding of a nucleus

A nucleus is a quantum object, consisting of protons and neutrons. Protons, with a positive charge should therefore repel one another. However the nucleus is a bound system, and therefore there must be some force that overcomes this repulsion to hold it together. This force is the nuclear force and its strength is shown in figure 1.4. The nuclear force is a very short range force that is attractive at ranges of approximately 1.7 fm and less, with the force being most attractive at a range of approximately 0.9fm. At separations of less than 0.7 fm the nuclear force becomes repulsive. At ranges greater than 2.5 fm, the nuclear force is so weak that the only significant force between nucleons is the Coulomb repulsion between protons.

Other properties of the nuclear force show that it is strongly spin dependent, and results in the force being stronger between nucleons that are spin aligned. There is also a tensor potential, which has a similar form as the force acting between two magnetic dipoles. The proton-proton and neutron-neutron interactions due to the nuclear force are also approximately equal due to the charge symmetry of the nuclear force. Similarly the proton-neutron

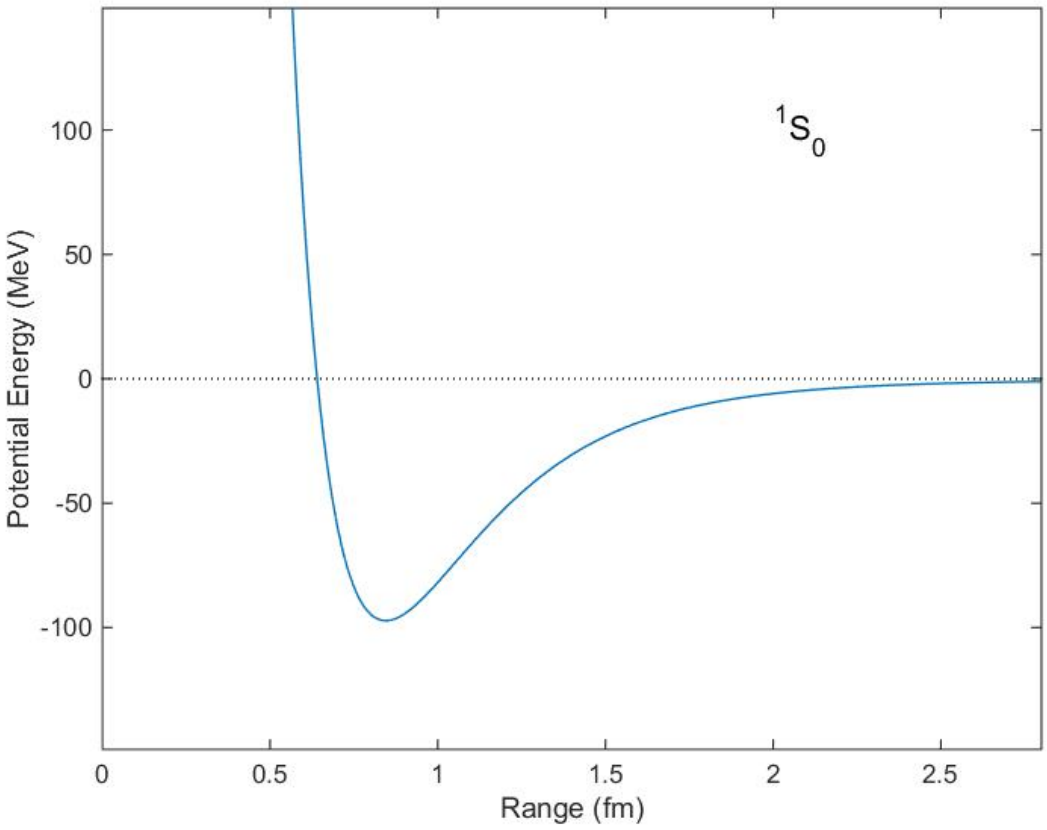

Figure 1.4: A figure showing the strength of the nuclear force between two nucleons calculated using the Reid Potential. This figure was adopted from [11].

interaction is also similar to the pp and nn interaction. Evidence for this comes from the scattering length, which for both pp, and nn interactions, have a scattering length of approximately -17 fm ($\alpha_{pp} = -17.1 \pm 0.2$ fm, $\alpha_{nn} = -16.6 \pm 0.5$ fm [7].

In nuclei, the drip line is located at the point where a nucleus will immediately decay via the emission of a proton or neutron (depending on the drip line). This occurs when the separation energy crosses 0. An unbound system can exist for a relatively long time, and not decay instantly. This happens when there is a resonance, which can occur due to the Coulomb barrier and the angular momentum providing a further barrier. This can significantly hinder the emission of a proton from an unbound system. In the case of ^{20}C, the second 2^+ state is a neutron unbound state, so the only hindrance it will see is the barrier created by the angular momentum, which has a much smaller effect than the Coulomb barrier [12]. The spectroscopy of 4<N<8 isotones has been performed as this is the location of the neutron drip line for very low values of Z. Typical lifetimes of these states are inferred from the width of the resonance, predicting a lifetime of a few zs (1 zs = 1×10^{-21} s) [12].

1.2.4 Unbound excited states

The limits of bound nuclei is found by following the trend of the neutron or proton separation energies, defined in equation 1.9. The point at which the proton or neutron separation energy becomes negative identifies the drip line [13].

The binding energy (in MeV) of a nucleus is given by equation 1.8.

$$B(N,Z) = ZM_H + NM_n - M(N,Z) \tag{1.8}$$

Where Z is the atomic number, M_H is the mass of a hydrogen atom, N is the number of neutrons, M_n is the mass of a neutron and M(N,Z) is the mass of the nucleus [13]. From this, the neutron separation energy can be determined using equation 1.9.

$$S_n(N,Z) = B(N,Z) - B(N-1,Z) \tag{1.9}$$

In a bound nuclei, such as ^{20}C, it is possible to form the nucleus with an excitation energy greater than the neutron separation energy. If this is the case, then the state is not bound and will result in a neutron being emitted. A γ-ray may also be emitted if the unbound state decays to an excited state in the daughter nucleus. In ^{20}C, the neutron separation energy as determined by experiment is 2.980 MeV [14]. Theoretical studies also predict the neutron separation energy to be 2.9014 MeV [15], so the predicted 2^+_2 state in ^{20}C at approximately 7 MeV (discussed later) is an unbound state.

1.3 Sub-shell Closures

As seen in figure 1.1, the introduction of spin orbit splitting results in the formation of relatively large energy gaps, which are indicative of possible sub-shell closures. The nucleus of ^{20}C is comprised of 6 protons (Z=6) and 14 neutrons (N=14), which are two of the numbers predicted by the introduction of the spin orbit splitting to exhibit sub-shell closures.

1.3.1 N=14 sub-shell closure

The prevalence of the N=14 sub-shell closure, which is first seen in oxygen, will be discussed first. This has been observed by measuring the 2^+_1 state in ^{22}O (Z=8, N=14), which was measured to be 3170 keV. This measurement is significantly higher than the observed energy for the same transition in ^{18}O (Z=8, N=10) and ^{20}O (Z=8, N=12). The excitation energies of the first 2^+ state is shown in figure 1.5. This provides an indication that there is a sub-shell closure at N=14 [16]. Further evidence comes from shell model calculations, which suggest a shell gap of 4 MeV for the N=14 sub-shell closure in ^{22}O [17].

The existence of the N=14 sub-shell closure has been investigated further by looking at the N=14 isotones ^{21}N (Z=7, N=14) and ^{20}C (Z=6, N=14). In the case of ^{20}C, multiple studies have found the first 2^+ state to have an energy of approximately 1.6 MeV. In the study by M. Stanoiu [18], the first 2^+ states of ^{18}C and ^{20}C (N=12 and 14 respectively) were measured. They determined the states to have energies of 1585(10) keV and 1588(20) keV respectively. These values show no significant change in the energy of the first 2^+ state, providing evidence that the N=14 sub-shell closure does not exist in ^{20}C [18]. In the case of ^{22}O, the energy of the first 2^+ to ground state transition was approximately two times larger than the state in ^{20}O [16]. However, studies of nitrogen isotopes suggest that the shell gap exists to some extent. In the investigation carried out by D. Sohler et al. [19], a similar procedure was followed to M. Stanoiu, with the first 2^+ states in nitrogen with N=10,12 and 14 measured. As these isotopes are odd-even nuclei, the excited states will not be described by an integer for the excited states, as discussed in section 1.2.2. Therefore in order to extract the effective 2^+ energy, the (2j+1) weighted average of the $^3/_2{}_1$ and $^5/_2{}_1$ excited states was used. For N=10 and 12, the energy of the 2^+ states were determined to be 1687 keV and 1463 keV respectively, which is lower than their counterparts in carbon and oxygen. However, for ^{21}N, with N=14, the energy of the 2^+ state jumps by 500 keV, suggesting that the N=14 sub-shell closure survives to some extent in Z=7 nuclei [19].

Along the oxygen isotopic chain, the appearance of the sub-shell closure in ^{22}O is explained by neutrons filling the $d_{5/2}$ orbit. The addition of the neutrons in the orbit results in a slow decrease in the effective single-particle energy of the orbit in respect to the $s_{1/2}$ orbit as neutrons in the $d_{5/2}$ orbit become more bound, which results in an increasing shell gap.

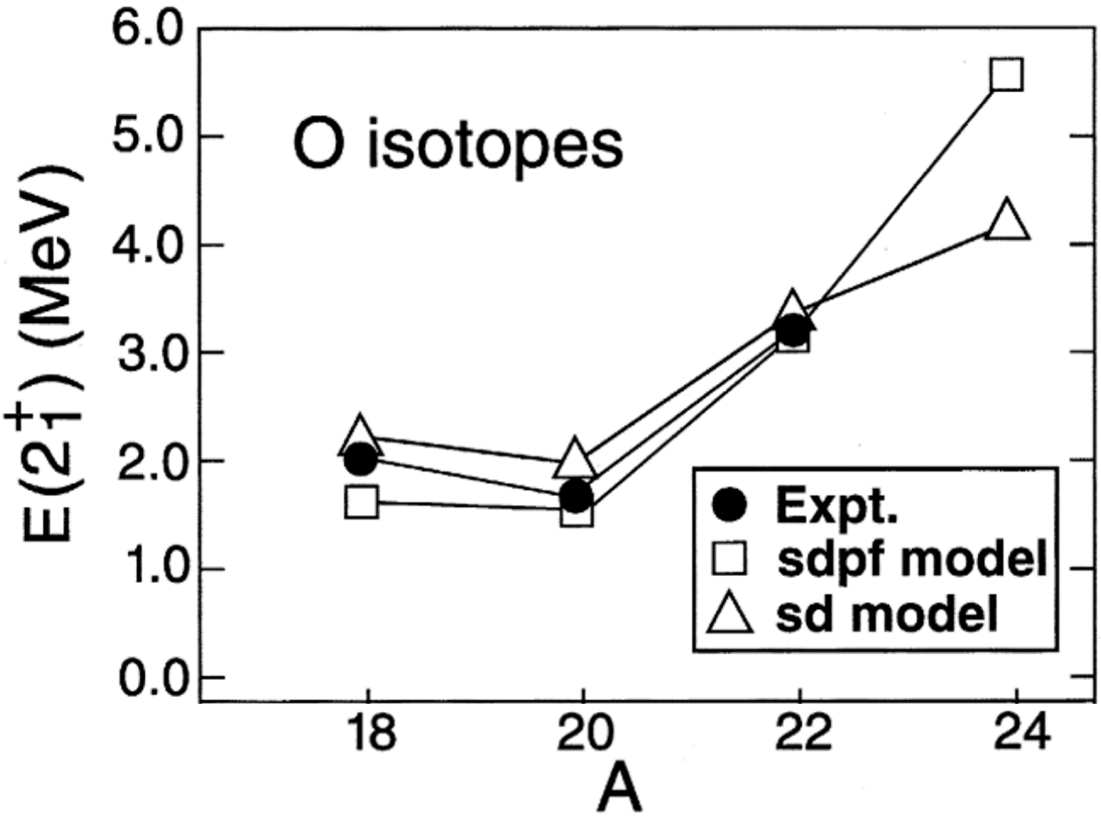

Figure 1.5: The evolution of the 2_1^+ excitation energy in neutron rich oxygen isotopes. As can be seen, there is a large increase in the excitation energy of ^{22}O (Z=8, N=14) compared to ^{18}O and ^{20}O, providing an indication of the N=14 sub-shell closure. This figure was adopted from [16].

This is the result of a large attractive $V^{nn}_{d_{5/2}d_{5/2}}$ matrix element. As a result, a large energy gap, of approximately 4.2 MeV appears in ^{22}O (Z=8, N=14) [18]. The effect of this is seen in the left panel of figure 1.6.

In contrast, in the carbon isotopes, the energy of the first 2^+ states in even-even nuclei is seen to be very similar for ^{16,18,20}C. As seen in the right panel of figure 1.6, the $s_{1/2}$ orbit starts with a lower energy, and as the neutron number increases, the energy remains close to the $d_{5/2}$. The difference between the evolution of the ESPE (Effective Single-Particle Energy)in the oxygen and carbon isotopic chains arises due to the crossing of the neutron $s_{1/2}$ and $d_{5/2}$ orbits in ^{15}C compared to ^{17}O. This is the result of the removal of two protons, which changes the proton-neutron TBME (Two Body maxtrix element), $2\left(V^{pn}_{p_{1/2}d_{5/2}} - V^{pn}_{p_{1/2}s_{1/2}}\right)$ resulting in an attractive first term and repulsive second term. This crossing means that while (as expected) the neutron-neutron matrix element remains attractive, the two orbits remain close, resulting in the two states being filled at the same time (they are degenerate), and therefore there is significant configuration mixing, and the N=14 sub-shell closure does not form. This has been observed experimentally by Wuosmaa et al. by measuring the relative spectroscopic factors for excited states populated using a neutron-transfer reaction ^{15}C(d,p)^{16}C [20]. Theoretical predictions [21, 22, 23] also support the degeneracy of the sd shell in neutron rich carbon. Therefore the two orbits are filled at the same time, they are degenerate, and as a result, the N=14 sub-shell closure does not form. This explains the consistency of the energy of the first 2^+ states in even-even carbon isotopes.

1.3.2 Z=6 sub-shell closure

The prediction of a Z=6 sub-shell closure was noted by Goeppert Mayer, who also noted a shell gap at N=14 [24]. Various measurements have been performed to determine if the sub-shell closure exists, and if it does, its prevalence. The formation of the Z=6 sub-shell closure occurs in neutron rich carbon at $^{14}_{6}C_8$. With eight neutrons, it is expected that neutrons would be in a closed shell, while the 6 protons do not form a classic magic number. Experimental measurements of ^{16}O, which is double magic, show a very high excitation energy for the 2^+ state at 6.9171 MeV [25], which is typical for a doubly magic nucleus. Similarly ^{14}C shows a very high excitation energy of 7.012 MeV [26] which is an indication of the formation of the Z=6 sub-shell closure. Low B(E2) values are also a further indication of a shell closure due to small proton contributions, and this is observed in ^{16,18,20}C, which indicates that the proton contribution to the 2^+ state is small, providing evidence for a sub-shell closure at Z=6 [27]. This has since been re-measured and will be discussed later.

Measurements of the proton radii of carbon, oxygen, beryllium and boron [28, 29, 30, 31, 24] also lend evidence towards Z=6 being a sub-shell closure. The change in proton radii is seen in figure 1.7 [24]. The measured proton radii for $^{12-19}$C shows a flat trend, fluctuating

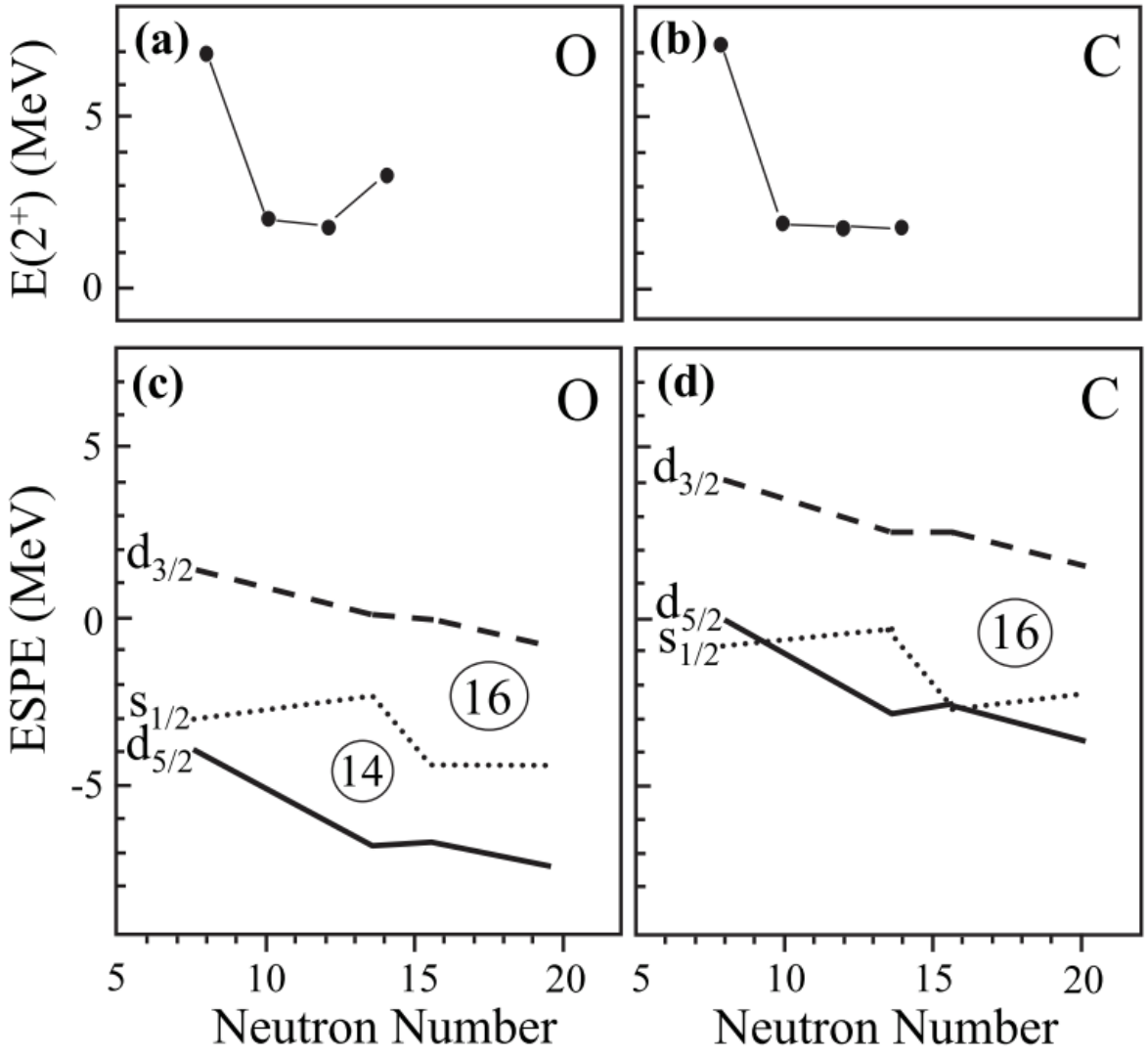

Figure 1.6: The left panel shows the growth of the N=14 energy gap between the $d_{5/2}$ and $s_{1/2}$ orbits in oxygen isotopes. The right panel shows the lack of appearance of the N=14 energy gap in carbon isotopes. This figure was adopted from [18].

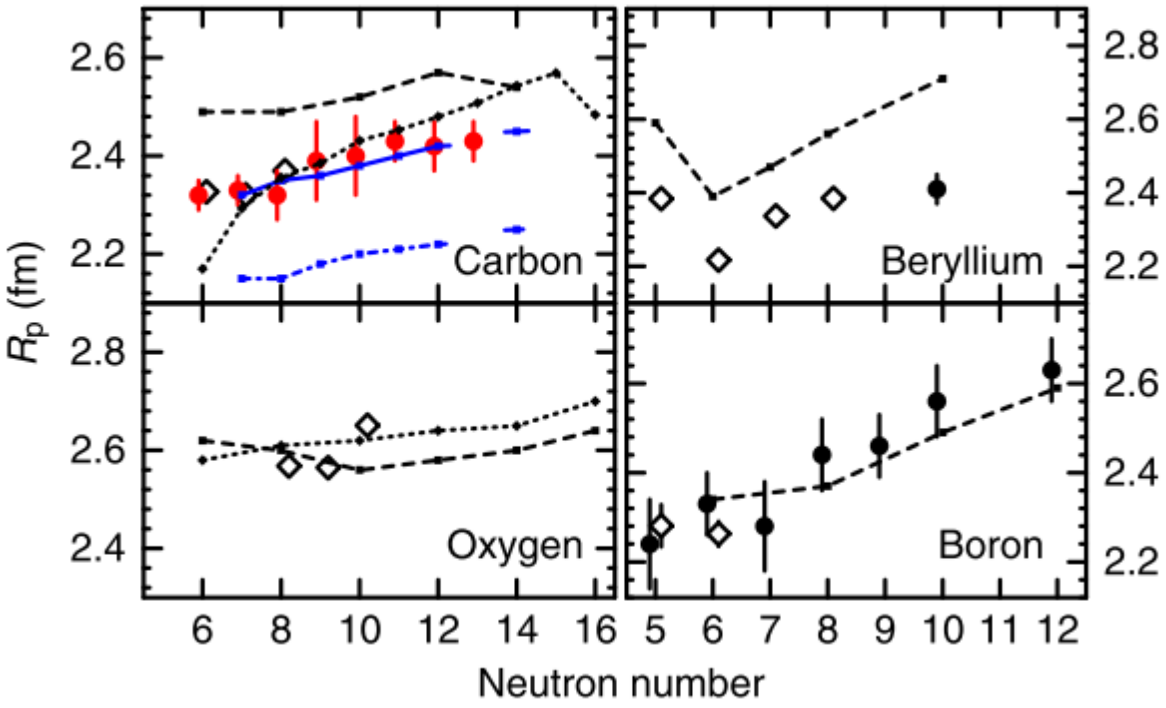

Figure 1.7: The change in proton radii for carbon isotopes is shown in the top left panel. It is seen that the trend is flat, which is similar to the trend seen in oxygen isotopes, shown in the lower left panel. Symbols such as the diamonds, and circles are experimental values, while the dashed lines are values extracted from model calculations. This figure was adopted from [24].

by less than 5%. This trend is similar to the measured and calculated proton radii in oxygen, which is magic, with Z=8. In beryllium and boron, the trend fluctuates much more significantly, by as much as 10%. For beryllium and boron, this is associated with clustering. In carbon, the trend is similar to that observed in oxygen, which is magic. This may occur due to the presence of an inert proton core, $p_{3/2}$, which would indicate a Z=6 sub-shell closure [24].

More recent work calls in to question the prevalence of the Z=6 sub-shell closure as the neutron drip line is approached. The first indication is the re-measurement of the B(E2) values for even-even carbon isotopes. As mentioned previously, a low B(E2) value is an indication of a proton shell closure due to the low probability of proton excitation. The measurement of the B(E2) values in ^{14,16,18}C shows a consistently low value. However the measurement of the B(E2) value for ^{20}C shows a moderate increase, see figure 1.8, which is an indication of a weakening of the sub-shell closure due to a weakening of the $1p_{1/2}$-$1p_{3/2}$ spin orbit splitting [32].

Further evidence that the Z=6 sub-shell closure is diminished as the neutron drip line

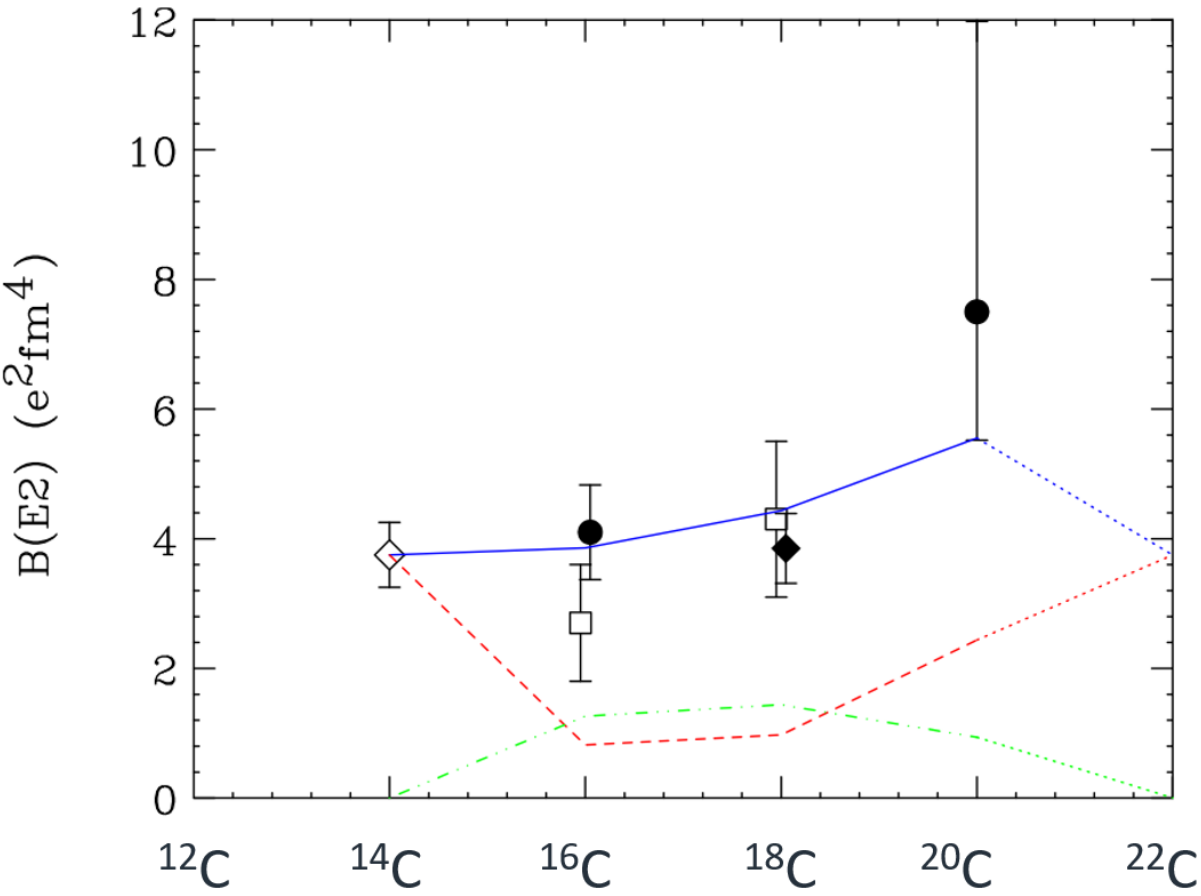

Figure 1.8: The change in B(E2) values for even-even carbon isotopes. It is seen that the B(E2) values in ^{14,16,18}C shows a consistently low value, indicating a sub-shell closure, while the B(E2) value for ^{20}C shows a moderate increase. The green line shows the contribution from the neutrons, the red line shows the contribution of the protons and the blue line shows the sum of the proton and neutron contributions. This figure was adopted from [32].

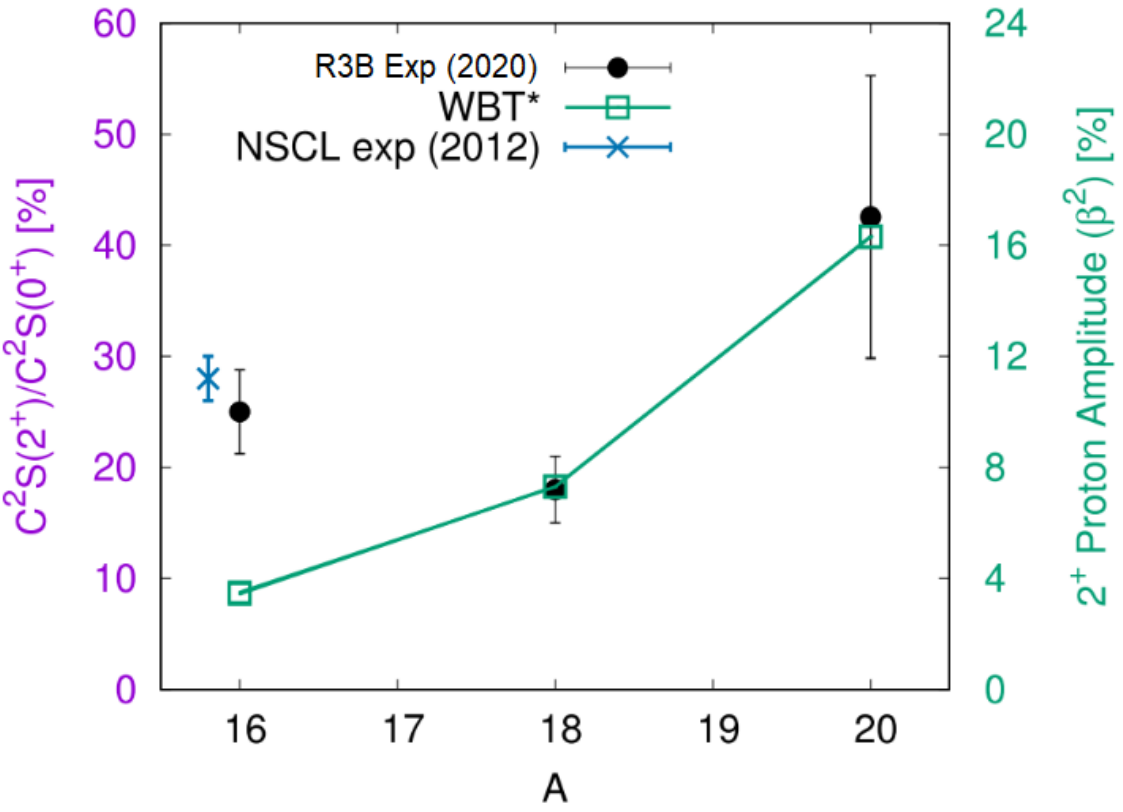

Figure 1.9: The change in proton amplitudes for even-even carbon isotopes. It is seen that that the proton amplitude in ^{16,18}C shows a consistently low value, indicating a sub-shell closure, while the proton amplitude for ^{20}C shows a moderate increase. This figure was adopted from [33].

is approached was found by Ina Syndikus et al. [33]. In this study the proton amplitude, which is a measure of the amount of proton excitation for a given state in a nucleus, and is discussed later in more detail in section 3.5, was measured for even-even carbon isotopes. The proton amplitude of ^{16,18,20}C was determined, with the trend shown in figure 1.9, and for ^{16,18}C the proton amplitude was determined to have relatively low values, indicating only a very small amount of proton excitation. However, in ^{20}C, the proton amplitude, similar to the B(E2) values, shows a moderate increase in its value. This is an indication of an increase in proton excitation, which is further evidence for a weakening of the sub-shell closure as the neutron drip line is approached [33].

1.4 Neutron rich carbon

The carbon isotopic chain represents a good region for testing nuclear theories due to the accessibility of the neutron drip line and the large number of nuclei between ^{12}C and the

neutron drip line. An interesting feature observed in neutron rich carbon isotopes are halo nuclei. This was determined by measuring the interaction cross section of ^{19}C by impinging a beam of ^{19}C onto a carbon target [34]. These measurements find an unexpectedly large interaction cross section, which in combination with Glauber model calculations of the root mean square radii provides evidence for the existence of a one-neutron halo. This is backed up by narrow momentum distributions observed through the knockout of a neutron from ^{19}C [35], indicating a one-neutron halo. In the same experiment [35], the two neutron removal reaction from ^{22}C also shows a narrow momentum distribution, indicating that ^{22}C is a two-neutron halo nucleus. As previously mentioned, there is no evidence for the N=14 sub-shell closure in ^{20}C, despite being observed in oxygen, and in a diminished magnitude in nitrogen. This is discussed in section 1.3.1.

A key question, which this work aims to provide further evidence, is if the Z = 6 sub-shell closure survives all the way to the neutron drip line at ^{20}C, with previous work indicating the potential for a weakening as the neutron drip line is approached.

1.5 Current Information on ^{20}C

1.5.1 Experimental Studies

The ^{20}C nucleus that will be investigated in this PhD project is the second heaviest bound nuclei in the carbon isotopic chain, with ^{21}C (even-odd) being unbound, and ^{22}C being the heaviest bound nucleus. The first observation of ^{20}C was in 1981 at the Lawrence Berkeley Laboratory Bevalac [36]. The ^{20}C along with other reaction products was produced by the fragmentation of a 213 AMeV ^{48}Ca beam on a beryllium target. This resulted in the first clear observation of ^{20}C with approximately 40 counts [36].

Despite the first observation of ^{20}C occurring over 40 years ago, the current experimental knowledge of ^{20}C is limited to the ground state and the first bound excited 2^+ state. Previous work has been performed at R3B to measure the proton amplitude of ^{20}C the decay spectra of the 2^+ state in this experiment is seen in figure 1.10. As discussed in section 1.3.2, this work has very limited statistics for the production of ^{20}C. As a result, the proton amplitudes measured value of $17 \pm 5\%$ is limited by its very large statistical uncertainty. The spectra, showing the decay of the 2^+ state in this experiment is seen in figure 1.10.

The half-life of the the ground state of ^{20}C has been measured experimentally to be $T_{1/2} = 14^{+6}_{-5}\ ms$ [37] by fitting the time distribution of the β delayed neutrons with respect to the implantation signals.. This is important information to know as it means that essentially all ^{20}C produced by a proton knockout reaction in the target will reach the end of the experimental setup without decaying to ^{19}C.

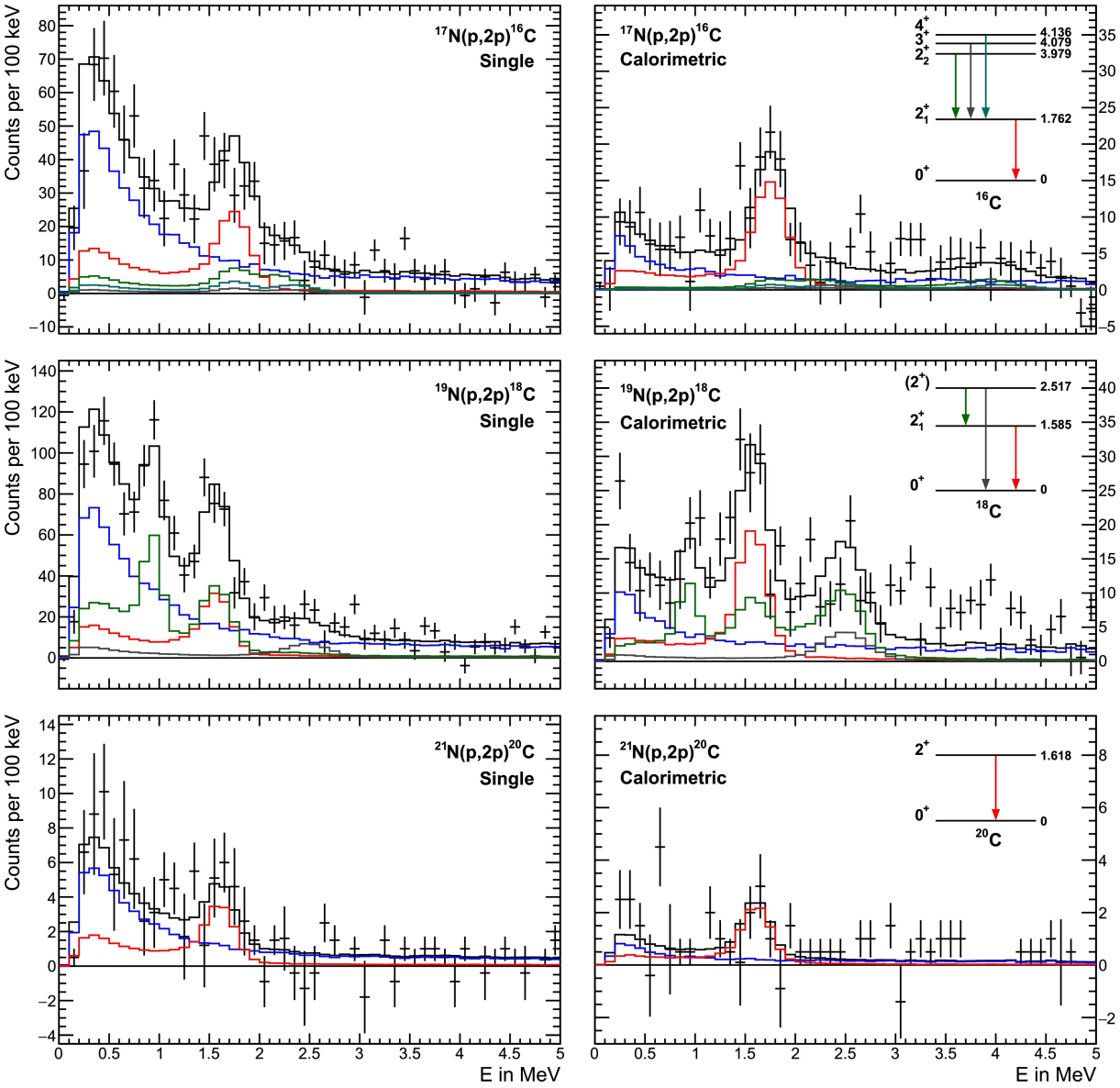

Figure 1.10: The bottom two panels show the decay spectra of the 2^+ state in ^{20}C. As can be seen, this channel has low statistics, which result in the large uncertainty in this measurement.This figure has been adopted from [33].

The transition from the first excited 2^+ state to the ground state has been known since 2003, with the energy of the decay to be approximately 1600 keV. The first measurement determined the transition to have an energy of 1588(20) keV [17]. The more recent study performed at NSCL at MSU, using the two proton knockout reaction ^{9}Be(^{22}O,^{20}C+γ)X has found the transition energy to be 1618(6) keV [38]. The lifetime of the state was measured using the recoil distance method, which was setup to be most sensitive to a half-life of 10-20 ps. This resulted with a half-life being determined to be $T_{1/2}$=9.8±2.8 ps [38].

1.5.2 Theoretical Studies

The investigation of ^{20}C using shell model calculations is of great importance to help understand experimental data in ^{20}C. In 2014, a study [39] using ab initio **C**oupled-**C**luster **E**ffective **I**nteractions (CCEI) for the shell model, shown in figure 1.11, was used to explore the excited states in neutron rich isotopes of carbon and oxygen. This shell model calculation uses nucleon-nucleon and three-nucleon forces from chiral effective-field theory to predict the ground and low lying excited states of $^{17-22}$C and $^{19-24}$O. In the study, they find the first 2^+ state of ^{20}C to be 1.72 MeV with an uncertainty of no more than 10%. This is roughly in agreement with the excitation energy of 1618(6) keV, which lies within the uncertainty, found by Petri et al. in 2011. Furthermore, the model predicts excited states above this that are unbound. The excited states are shown in figure 1.11. The CCEI model predicts that there is a second 2^+ state at approximately 3.8 MeV, as well as a 4^+ state at 3.7 MeV, a 0^+ state at 4 MeV and a 3^+ state at 4.3 MeV.

The CCEI work makes reference to the $p-sd$ Hamiltonian of Warburton and Brown (WBP) model, which is a p-sd shell model calculation using the OXBASH shell model code [40]. The p-sd refers to the protons being in the p shell model space, and the neutrons in the sd shell model space, while the calculation used harmonic oscillator wave functions [41, 42]. This calculation [43] gives rise to a predicted energy of the 2^+ state of just over 2 MeV, significantly higher than the energy determined experimentally, as shown in figure 1.12.

Another model, using the $spsdpf$ interaction based on the psd PWBT interaction (WBT) model is a similar model based on a different hamiltonian [41]. It is useful to compare WBT to WBP in order to evaluate the theoretical error. This model is able to reproduce the energy levels of neutron rich oxygen nuclei [18], however when it is applied to neutron rich carbon nuclei such as ^{20}C, the energy predicted of the first 2^+ state is too high, similar to WBP model predictions,as shown in figure 1.13. Based on the experimental energy levels observed in ^{18}C and ^{20}C, the WBT* model was produced by multiplying the neutron-neutron TBME by 0.75 in order to get a better reproduction of the excited states seen in ^{18}C and ^{20}C [18].

The WBT* interaction represents the current best model for the excitation energy of the experimentally known 2^+ state in ^{20}C. The energy determined using No Core Shell Model

(NCSM) [44] or N^{3}LOW potential shell model calculations [45] predict similar excitation energies to the SBP/WBT model at approximately 2 MeV for the 2^+_1 state in ^{18}C and ^{20}C. Antisymmetrized molecular dynamics (AMD) calculations predict a much higher energy for the 2^+ state in ^{20}C [46, 47], with Thiamova et al. determining an energy of 3.4 MeV [48].

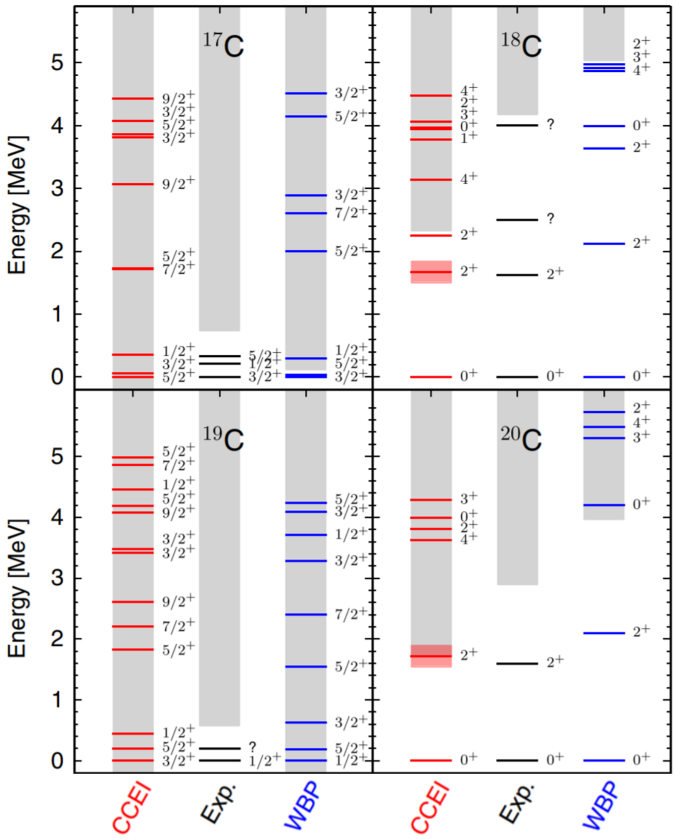

Figure 1.11: Excitation spectra of neutron-rich carbon isotopes. The grey bands represent the region where excited states are above the neutron separation energy. This figure was adopted from [39].

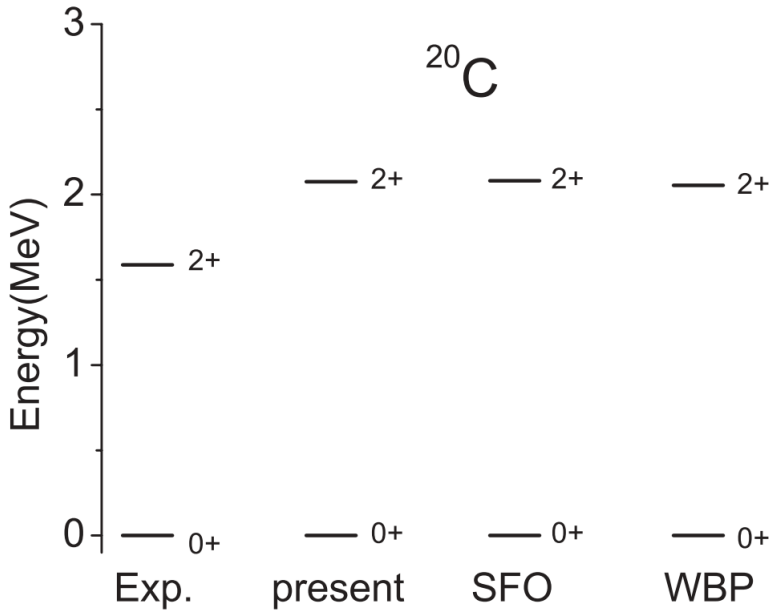

Figure 1.12: The energy of the 2^+ state in ^{20}C as predicted using shell model calculations, with different effective interactions. In the figure, present represents a monopole-based universal interaction, WBP represents interactions in the (0-1)$\hbar\omega$ model space. SFO represents shell model calculations in the (0-1)$\hbar\omega$ and (2-3)$\hbar\omega$ model space. It can be seen that all three models over estimate the energy of the first 2^+ state when compared to experimental values. This figure was adopted from [43].

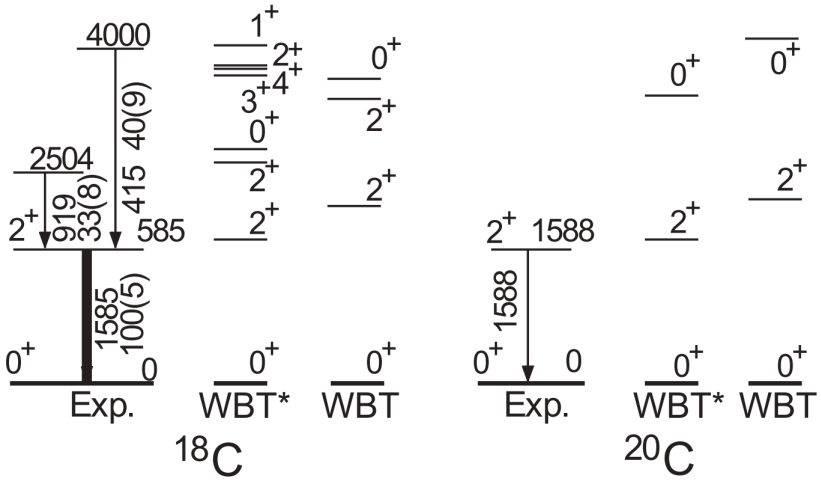

Figure 1.13: The energy of the excited states in ^{18}C and ^{20}C as predicted by the WBT and WBT* calculation. This figure was adopted from [18].

1.6 Thesis Objectives

The work presented in this thesis details the calibration and measurement of the population of the excited 2^+ state in ^{20}C. This was investigated through proton knockout reactions from a ^{21}N beam produced by the **R**adioactive **I**sotope **B**eam **F**actory (RIBF) facility at RIKEN. The decay of the 2^+ state was measured using the gamma ray detector DALI2 in the SAMURAI spectrometer. The exclusive cross section of the state can be determined using a GEANT4 simulation. This in combination with the measurement of the inclusive cross section enables the analysis of the proton amplitude. The re-analysis of the proton amplitude for ^{20}C is of great interest as it clarifies the prevalence of the Z=6 sub-shell closure at the neutron drip line. As mentioned previously, theoretical work for the proton amplitude based on the lifetime of the 2^+ state in ^{20}C predicts a proton amplitude of ≥30% [32]. If the proton amplitude was this high, it would indicate a significant increase in the value in relation to the proton amplitude of ^{16}C and ^{18}C, which in turn implies an increase in the proton excitation, and a decrease in the prevalence of the Z=6 sub-shell closure as the neutron drip line is approached. In later experimental work, Syndikus et al. [33] reported a proton amplitude of (17±5)%. This value is significantly lower than the previously reported theoretical value, however still represents a large increase in the proton amplitude when compared to ^{16}C and ^{18}C. The problem with this measurement is the very large statistical uncertainty in the measured value, as shown in figure 1.10. With this uncertainty, the true value of the proton amplitude could lie anywhere between 12-22%, which would represent a proton amplitude in line with ^{16}C and ^{18}C and therefore no weakening on the Z=6 sub-shell closure, up to a value which would represent a significant weakening of the Z=6 sub-shell closure. As a result, it is important to re-measure the proton amplitude for ^{20}C so that the ambiguity in the previous measurement can be removed.

In this thesis, Chapter 2 describes the different detectors that make up the SAMURAI spectrometer as used in the Day-One campaign. Chapter 3 details the methodology used in the analysis. Chapter 4 describes the calibration of the various detectors, and also describes the GEANT4 simulation used to simulate the response of DALI2. The results for the inclusive cross section, exclusive cross section and proton amplitude are shown in Chapter 5. The discussion of these results and future prospectives are shown Chapter 6. Supplementary figures and additional work is shown in Chapter 7.

Chapter 2

Experiment Setup

The experiment was performed at the RI Beam Factory (RIBF) facility at RIKEN in Tokyo, Japan in May 2012 for the SAMURAI (**S**uperconducting **A**nalyser for **MU**lti-particles from **RA**d**I**oisotope beams) Day-One campaign. A ^{48}Ca primary beam was used to produce a secondary cocktail beam centred on ^{23}O/^{22}N in BigRIPS. In-flight fragmentation results in a secondary cocktail beam that was then transferred to the SAMURAI experimental hall where further reactions with a carbon target with a density of 1.798 ± 0.001 g/cm^3 [49] produce ^{20}C along with other reaction fragments. In this study, ^{21}N in BigRIPS and ^{20}C fragments were tagged for analysis. The experimental devices used for the measurements are explained below.

2.1 The BigRIPS separator

To produce the secondary beam in this experiment, the RI beam factory used cyclotrons to accelerate a ^{48}Ca primary beam to 345 MeV/nucleon. This is impinged on a 20 mm thick beryllium primary target [49], located at F0. The result of this is in-flight fragmentation, resulting in a cocktail beam, which using the BigRIPS separator allows a secondary beam to be selected and transported to various experimental setups, in this case, the SAMURAI spectrometer. Figure 2.1 shows the setup of preceding accelerators, BigRIPS and different experiment setups, such as SAMURAI and ZeroDegree.

The BigRIPS separator has been designed to have large ion-optical acceptances in order to allow for the production of very neutron rich nuclei by using in flight fission of fissile beams. However in the case of the Day-One campaign, the experiment utilises in flight fragmentation.

The BigRIPS separator consists of two stages of magnetic spectrometers, the purification stage and the particle identification state. In figure 2.1, the first stage is located between the target and F2. It is composed of two room temperature dipoles, labeled D1 and D2, and four

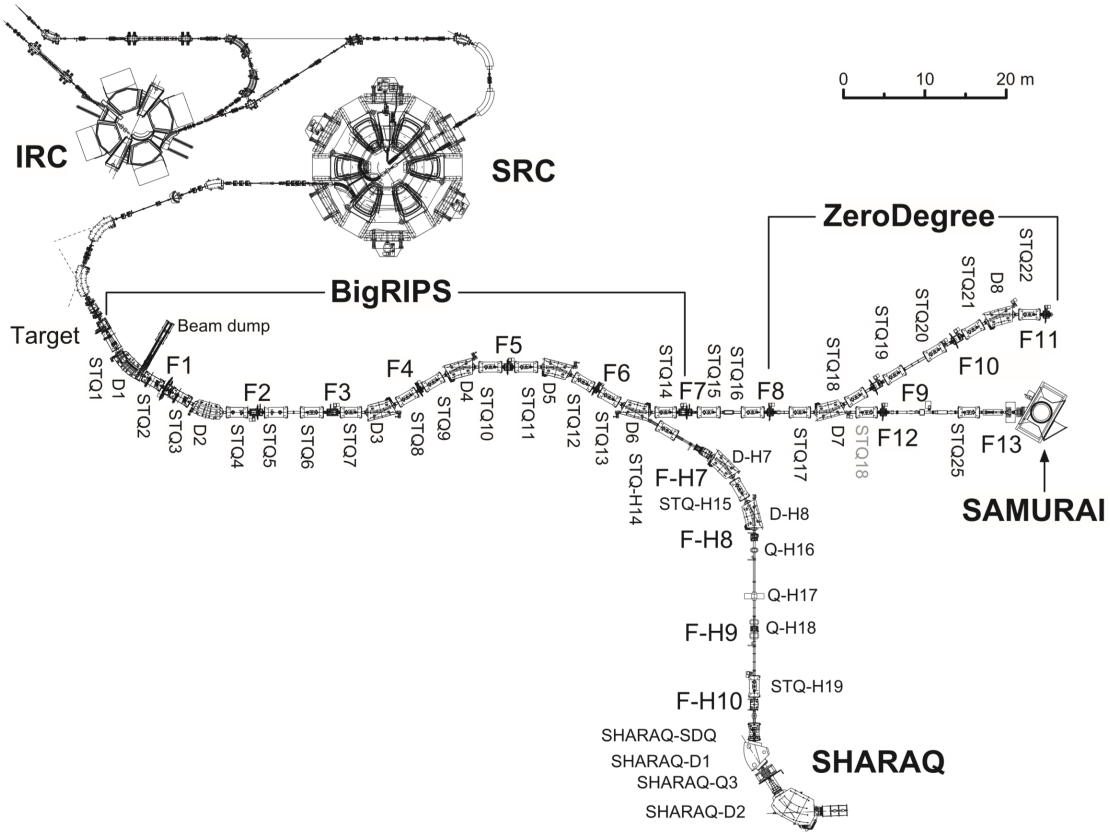

Figure 2.1: A schematic of the BigRIPS separator. This figure was adopted from [50].

STQs (**S**uperconducting **Q**uadrupole **T**riplets). This first stage uses an energy degrader to separate the cocktail beam into the desired secondary beam, however if further beam purification is needed, a second energy degrader is located in the second stage. In between the first and second stage there are two more STQs, that are used to adjust the angular magnification at F3, which reduces the loss of angular acceptance, and increases the momentum resolution.

The second stage of the BigRIPS separator consists of the remaining eight STQs and four dipoles. The second stage is used to further separate the beam using the dipoles and STQs and to identify the beam using the ToF-Bρ-ΔE method. To do this, the Time of Flight (ToF) is recorded using in beam, thin plastic scintillation counters located at the start and end of the second stage at F3 and F7. These detectors are single 3 mm thick plastic scintillators, with photomultiplier tubes on either end. Unlike the SBTs, which are also plastic scintillators used for timing, only a single plastic strip is used, whereas the SBTs are two layers of plastic scintillators. Bρ measurements are performed using position sensitive Parallel Plate Avalanche Counters (PPAC) located at F3 and F5. This is then performed again using the PPAC detectors located at F5 and F7, so that the A/Z value of the fragments can be identified. The ΔE measurements are performed using the **MU**lti-**S**ampling **I**onisation **C**hamber (MUSIC), located at the end of the separator [51].

2.1.1 Beam proportional chamber (BPC)

The **B**eam **P**roportional **C**ounter, shown in figure 2.2 is used to measure the rigidity of the incoming beam by measuring the horizontal (X) position of the beam. It is located with BigRIPS at the F5 focal plane, and is constructed with two anode planes, on which wires are attached with a spacing of 4mm, giving a drift length of 2mm. The BPC has a 100% detection efficiency for Z = 2-8.

2.2 SAMURAI spectrometer

The SAMURAI spectrometer is made up of many different detectors, and designed for kinematically complete measurements. The largest component of the setup is the rotatable 3.08 T magnet, designed to analyse charged particles. The charged particles identification is performed using the ToF-Bρ-ΔE method, and as such has detectors to determine time of flight, magnetic rigidity, and energy loss as well as neutron detectors. A schematic of the experimental setup is shown in figure 2.3.

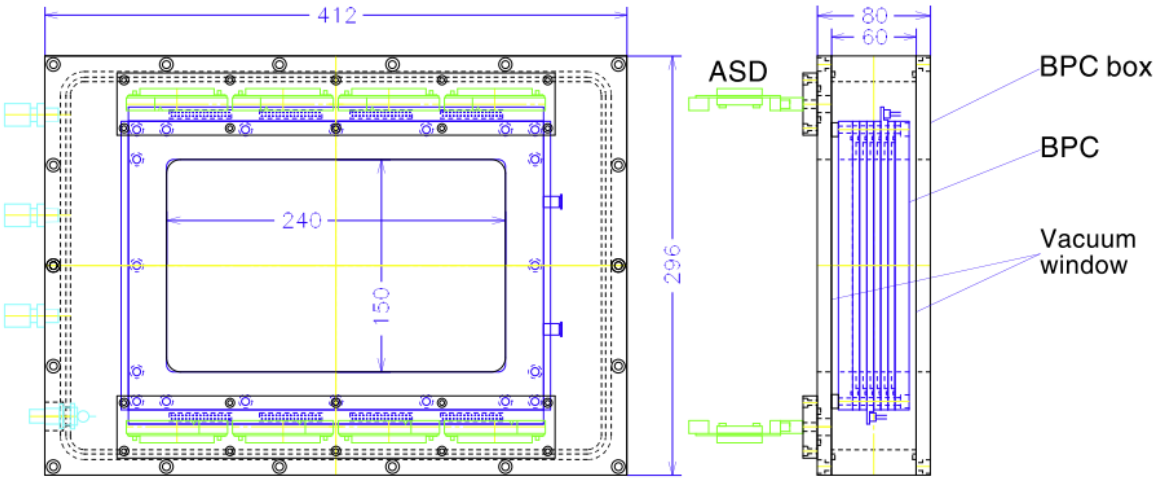

Figure 2.2: A schematic of the beam proportional counter (BPC). This figure was adopted from [52].

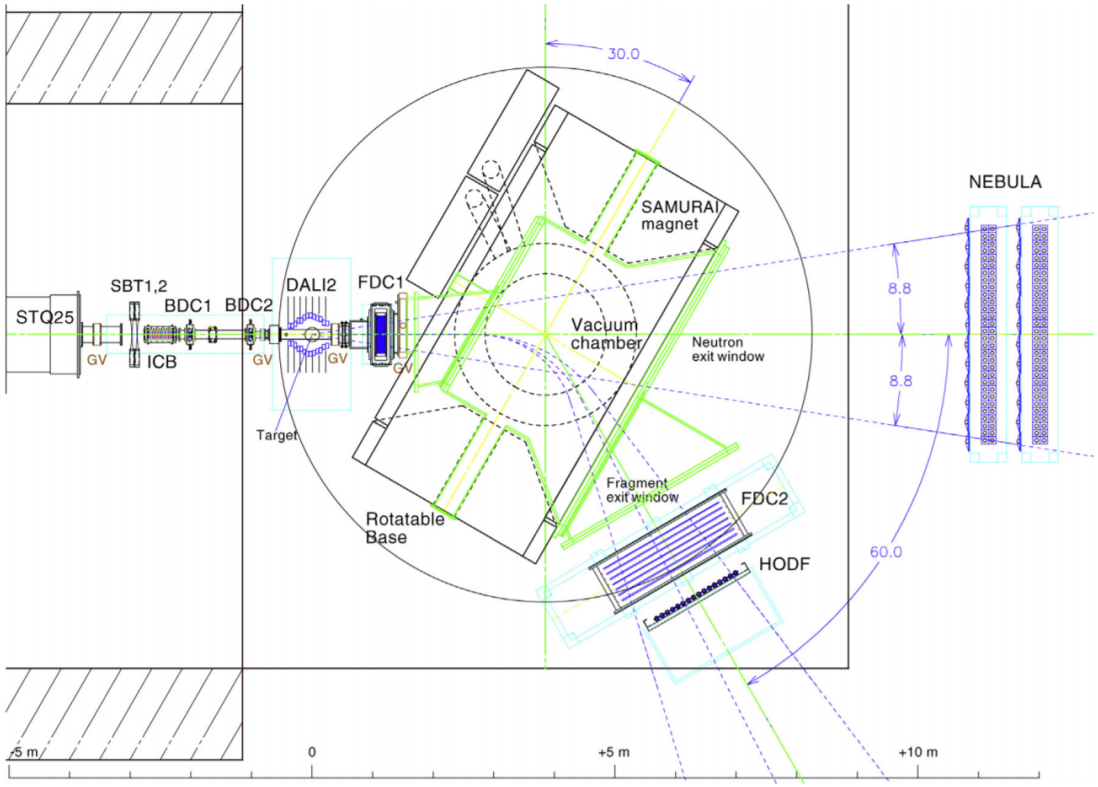

Figure 2.3: A schematic of the SAMURAI spectrometer, adopted from [52]

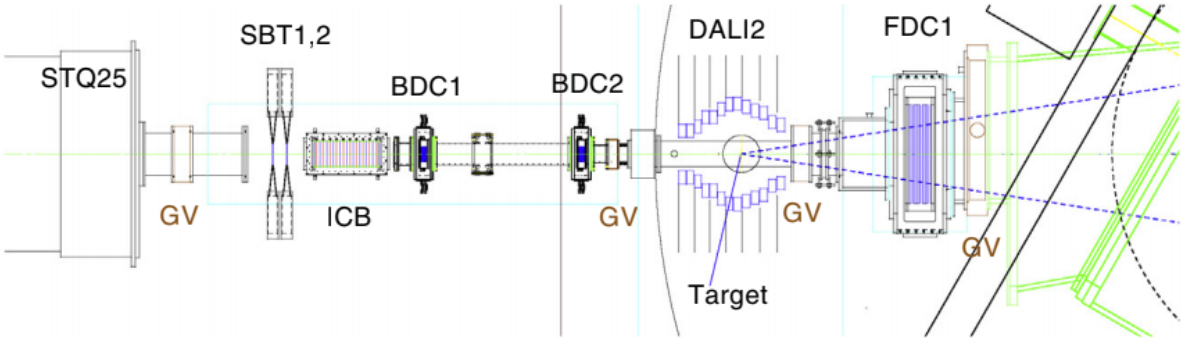

Figure 2.4: A schematic of the upstream detectors located before the SAMURAI magnet. This figure was adopted from [52].

2.2.1 The SAMURAI dipole magnet

Based on previous experiments, the SAMURAI magnet has been designed to have a bending power of 7.05 Tm. This is achieved with a magnetic field strength of 3.08 T [53]. The magnet is also designed to have a large inner vacuum chamber, measuring 80 cm in height. Two windows are installed on the SAMURAI magnet, one for neutrons and one for charged particles. This vacuum chamber allows the analysis of reaction product with less scattering. The magnet is also able to rotate, between -5° and +95°, and during the experiment was positioned at 30° to the beam line in order to accept reaction residues and neutrons at the same time. This design allows the SAMURAI magnet to have a large angular acceptance for particles, with a vertical acceptance of ±5° and a horizontal acceptance of ±10°. The geometry also allows for coincidence measurements of protons and heavy fragments even with A/Z = 3 [53].

2.2.2 Upstream Detectors

The following section describes the detectors located upstream of the SAMURAI magnet and downstream of BigRIPS, as shown in figure 2.4.

SBT1,2

The first detectors in the SAMURAI spectrometer setup are the 0.5 mm thick plastic scintillators SBT1 and SBT2 (they can also be configured to be 1 mm thick). These detectors are used as a beam trigger and for time of flight measurements. These plastic blocks have **P**hoto**M**ultiplier **T**ubes (PMTs) connected at either end to detect the light created in the scintillator block. They are located three meters upstream of the target [52], with a separation of 80 mm. The SBTs are used in conjunction with the detectors located at F3 and F7 in order to identify the incoming beam.

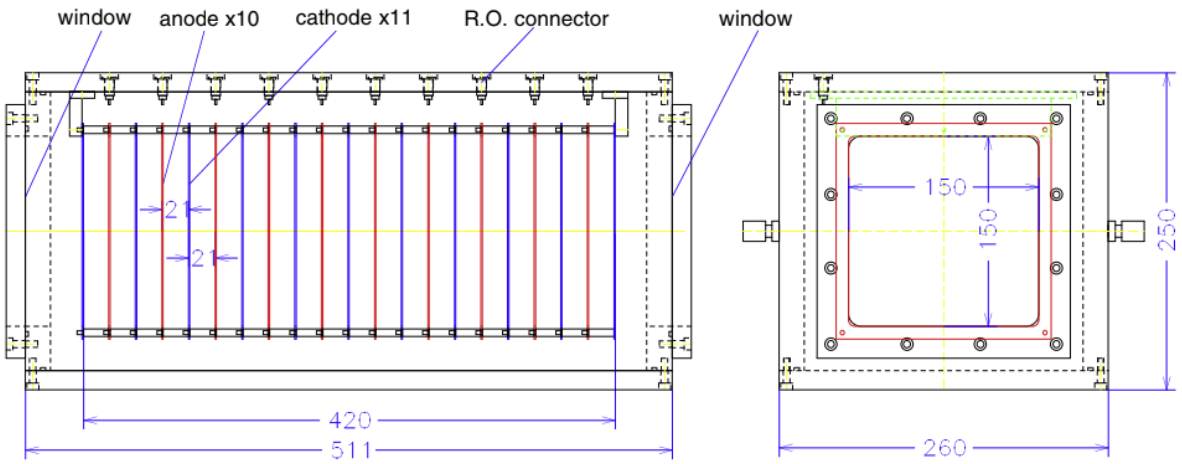

Figure 2.5: A schematic of the ICB, adopted from [52].

ICB

The **I**on **C**hamber for **B**eam (ICB), shown in figure 2.5, is a multi layer ion chamber containing the gas P10, which is a mixture of 10% methane and 90% Argon. Within the gas are ten anodes and eleven cathodes in order to cover the entire width of the detector, which are used to measure the energy loss. From this the charge resolution for Z = 6 is $\sigma_Z = 0.17$, with a pileup rate of 16% at a beam rate of 0.2 MHz. This detector is located between the SBTs and before BDC1, which are located before the target [52], as shown in figure 2.4.

BDC1,2

BDC 1 and 2, shown in figure 2.6, are two identical Walenta type **B**eam **D**rift **C**hambers, that are used to track the trajectory of the secondary beam to determine the beams position on the target. The BDCs contain $i-C_4H_{10}$ at 50-100 Torr. Within this gas, there are eight anode planes containing sixteen wires with a drift length of 2.5 mm [52]. With this, the mean X and Y position can be obtained within the BDCs with a resolution of 100 μm and a detection efficiency of 100%. With this determined and the geometry of the setup known, the position of the beam can be interpolated onto the target.

Target

The carbon target used in the experiment is located within the DALI2 gamma ray detector. This target has a density of 1.798 ± 0.001 g/cm^2 [49]. This was determined, as shown in figure 2.7 by weighing the target, which weighs 129.432 g, and measuring the thickness of the target at eight different points over the target. The thickness was then taken as the average of the eight points measured, with the uncertainty determined from the variation in thickness over

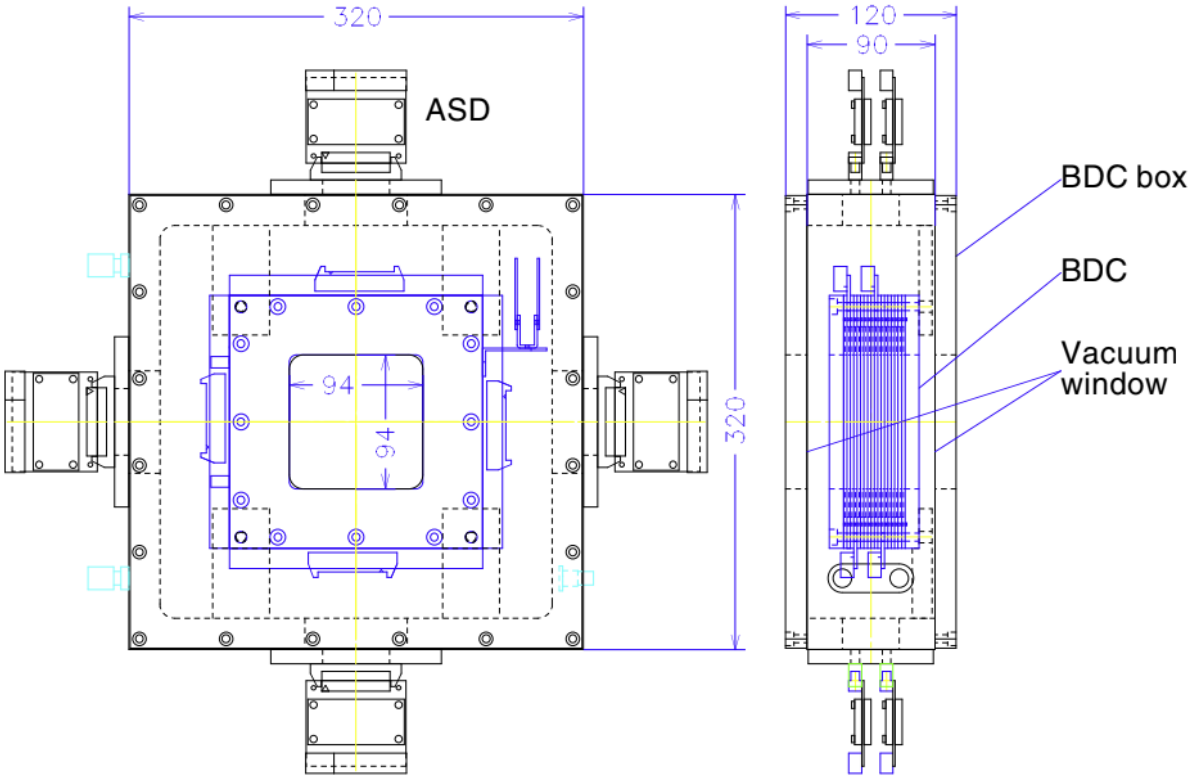

Figure 2.6: A schematic of the two identical BDCs, adopted from [52].

these points [54]. The secondary beam was then impinged on this target to create the reaction products of interest. There is also an empty target setting which is used in this analysis and a lead target which is not used.

2.2.3 Downstream Detectors

FDC1

In the SAMURAI spectrometer there are two different **F**orward **D**rift **C**hambers (FDC), FDC1 and 2. The first FDC, shown in figure 2.8 is located between the target and the SAMURAI magnet and is used to measure the angle that charged particles are emitted at following the secondary beams interaction with the target. This is done by determining the mean X and Y position of the ions within the drift chamber, which is done with a resolution of 110 μm and a detection efficiency of 100% and combining the information with the information determined in BDC1 and BDC2. FDC1 is a Walenta style drift chamber, with a 5 mm drift length. It is filled with i-C_4H_{10} at 50 Torr, within which fourteen sense planes are located, with wires in three different orientations, 0°, +30° and -30°. The FDC1 also has a wide opening to allow fast neutrons to pass through without any interaction.

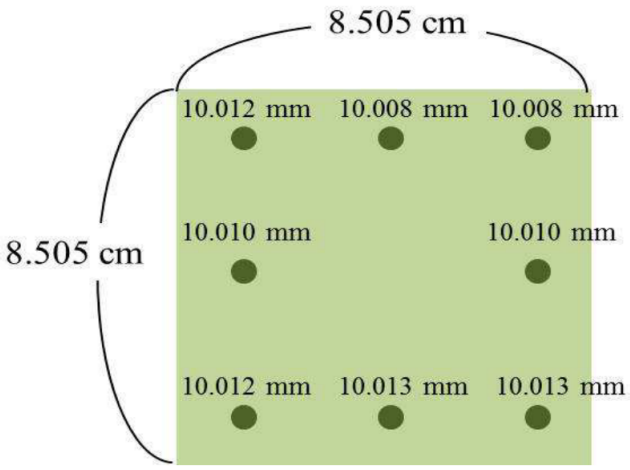

Figure 2.7: A schematic of the target, showing the thickness at different locations used to determine the density and uncertainty of the target, adopted from [54].

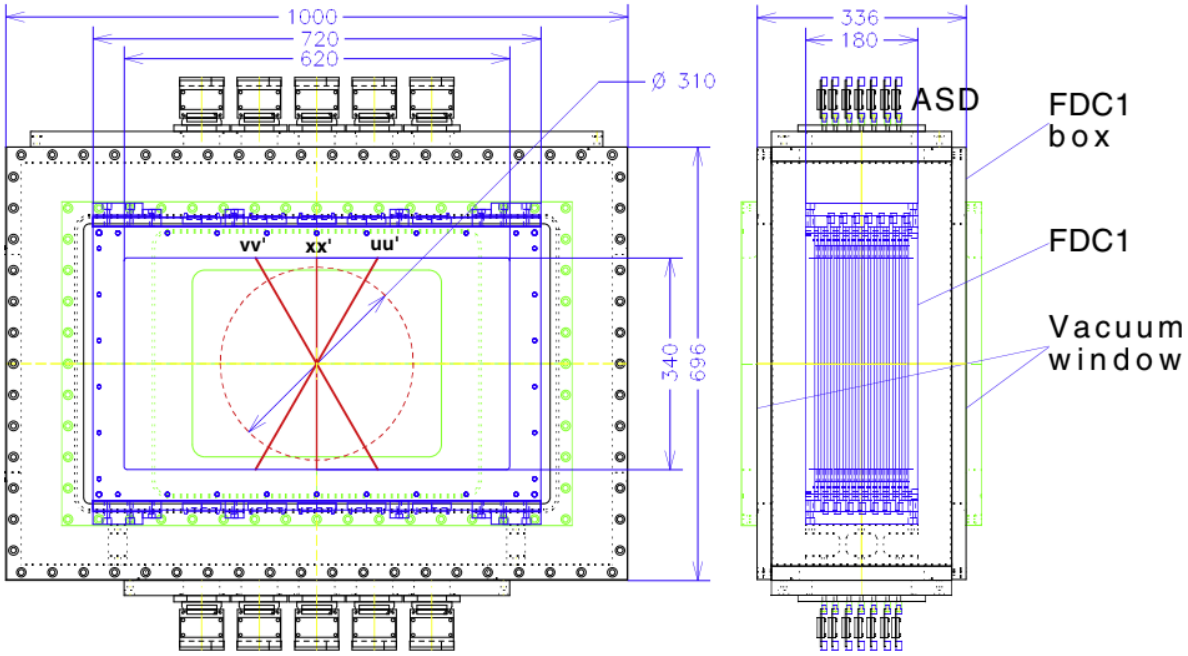

Figure 2.8: A schematic of FDC1, adopted from [55].

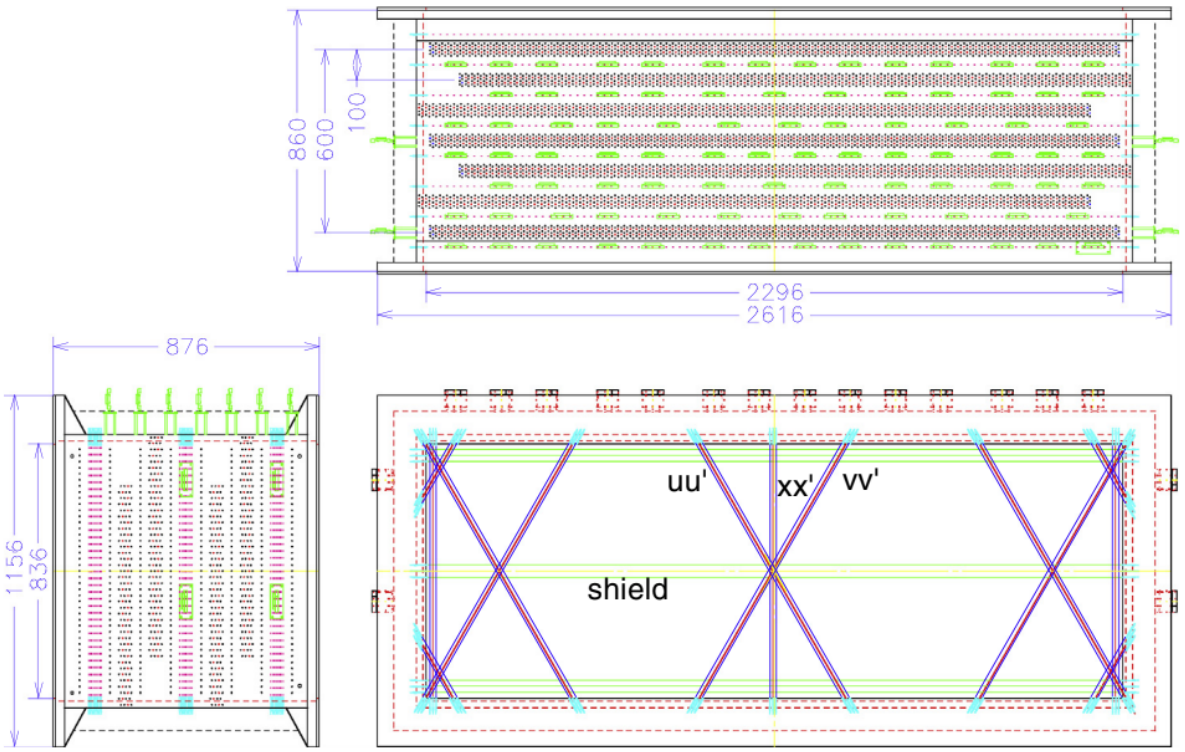

Figure 2.9: A schematic of FDC2, adopted from [55].

FDC2

The second forward drift chamber (FDC2), shown in figure 2.9, is a different design to the first, and is located after the SAMURAI magnet. It has the purpose of measuring the magnetic rigidity of charged particles after they have passed through the SAMURAI magnet by detecting the position and angle of reaction products within the detector. The drift chamber has a maximum drift length of 10 mm and is filled with a gas mixture of $He + 50\%C_2H_6$ or $He + 60\%CH_4$. Within this gas are fourteen sense planes and eight shield planes. These sense planes form a hexagonal structure, with sense wires laid out in the same three orientations as in FDC1 [52]. FDC2 has a resolution of 120 μm and a detection efficiency of 100%.

HODF

The **HOD**oscope for **F**ragments and Protons, shown in figure 2.10, is a large array of plastic scintillators located after the SAMURAI magnet and FDC2. It is designed to act as the final measurement for charged particles, measuring time of flight and energy loss. From this the charged particles can be identified. It is made of sixteen paddles, where each paddle is made of 1.2 m long vertical plastic scintillators, coupled to photomultiplier tubes at both ends via a light guide. With this, the detector has a charge resolution of $\sigma_Z = 0.16$ and a time of flight resolution of $\sigma_T = 140$ ps for ions with a charge up to eight [52].

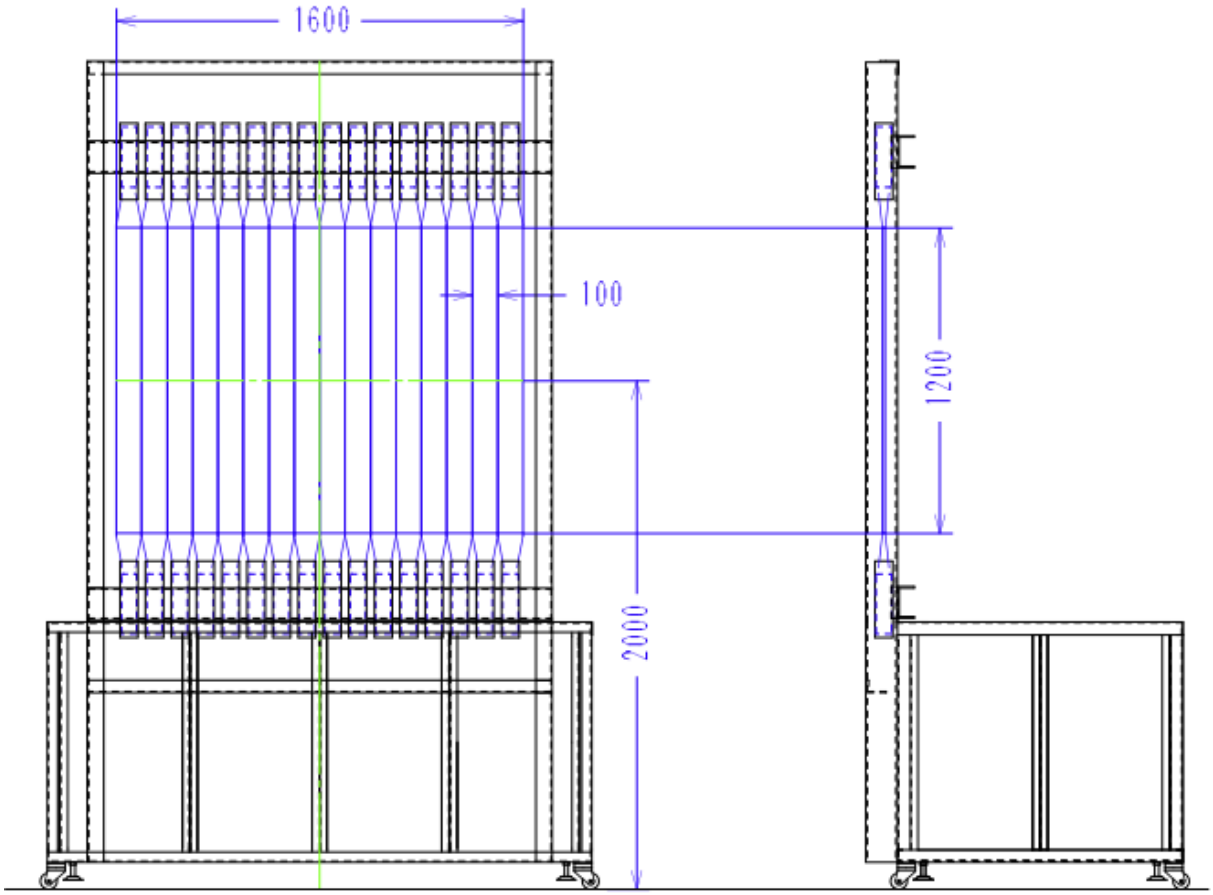

Figure 2.10: A schematic of the HODOSCOPE, adopted from [55].

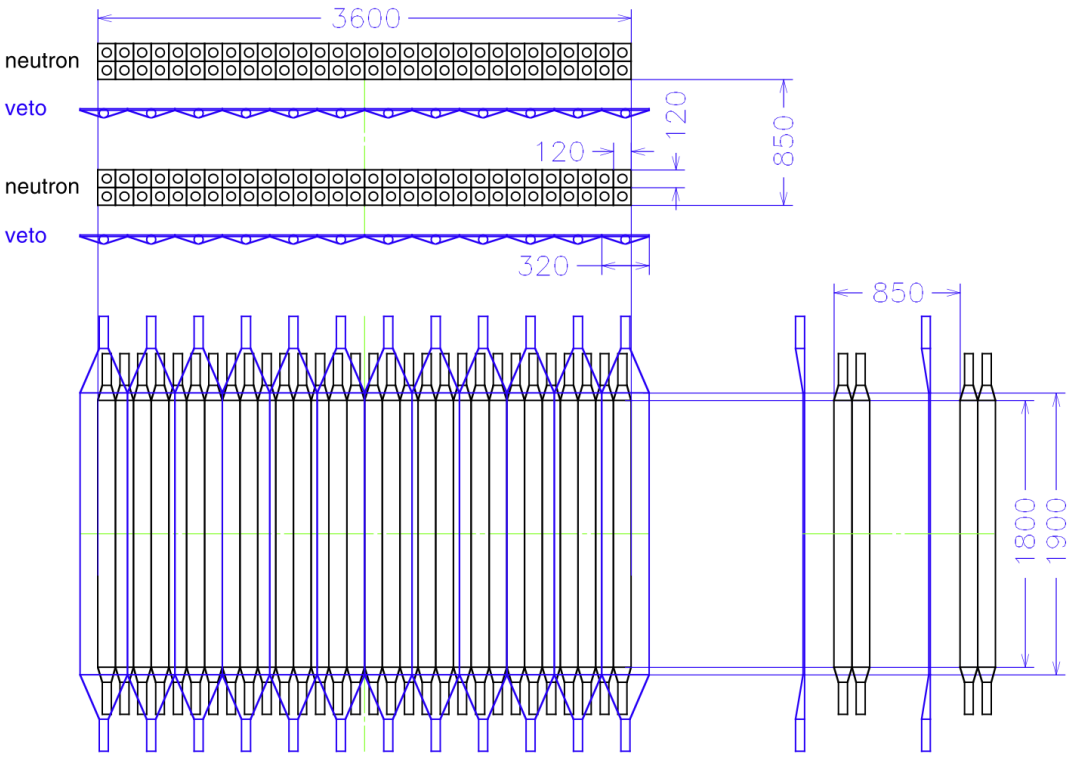

Figure 2.11: A schematic of the NEBULA neutron detector, showing how the different panels are laid out in the detector. On the right, it can be seen that there is a thin veto layer (shown in blue), that is used to detect charge particles, followed by two thick layers of plastic scintillators to detect the neutrons. This figure was adopted from [52].

NEBULA

The **NE**utron detection system for **B**reakup of **U**nstable nuclei with **L**arge **A**cceptance is a large array of plastic scintillators designed to detect neutrons with an energy of between 100 and 300 MeV, by the interaction of neutrons with charged particles in the plastic scintillators, which results in the charged particles being detected. As neutrons are not deflected in the presence of a magnetic field, NEBULA is located at 0° after the SAMURAI magnet. The detector is made out of six layers of plastic scintillators, grouped up into two sets of layers. Each layer is started by a layer of twelve thin (1 cm) plastic scintillators, connected via light guides with photomultiplier tubes at the top and bottom, in order to detect charged particles. This acts as a veto so that charged particles passing through the detector are rejected. Behind this veto are two layers of thicker (12 cm) plastic scintillators, with each layer containing thirty plastic scintillators. With this setup, the NEBULA array has a single neutron efficiency of approximately 40% and a two neutron detection efficiency of 12% according to simulations [52]. The setup is shown in figure 2.11.

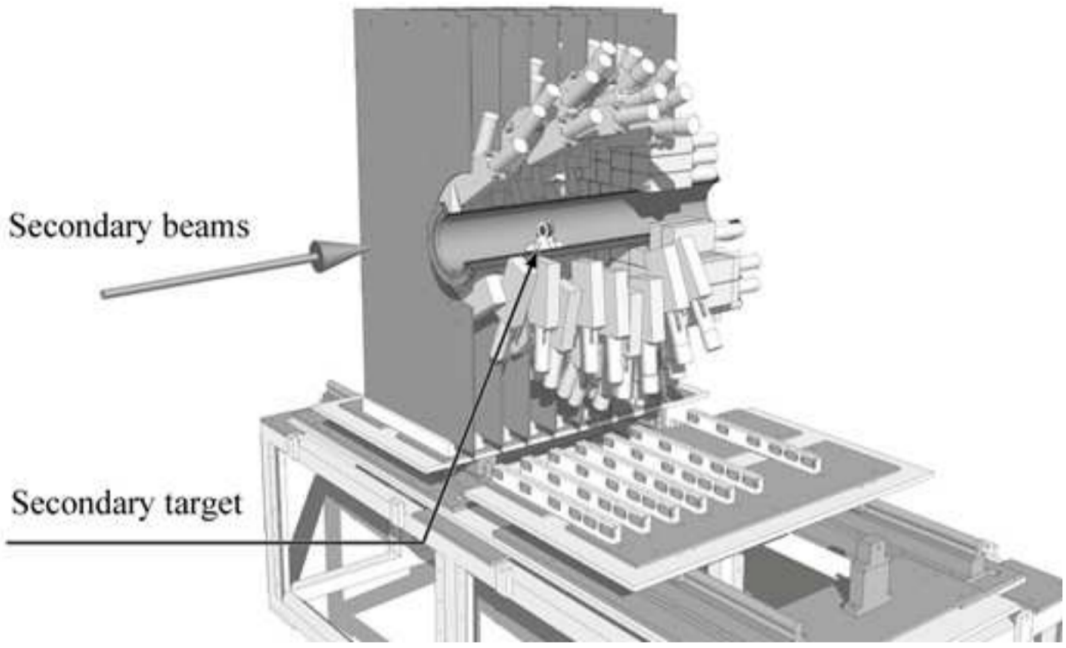

Figure 2.12: A schematic of the DALI2 array, adopted from [55].

2.3 DALI2

The **D**etector **A**rray for **L**ow **I**ntensity radiation **2** (DALI2) in the Day-One campaign is an array configured of 140 NaI (TI) scintillators coupled to photomultiplier tubes. The crystals are made in three different sizes, 45×80×160 mm^3, 40×80×160 mm^3 and 60×60×120 mm^3 and are arranged in thirteen layers. When a γ-ray interacts with the scintillating crystal, pulses of light are produced, which are detected by the PMTs. Using this geometry, DALI2 can cover polar angles of 15° to 160° with an average full width half maximum angular resolution of 6°. This enables the detection of forward emitted gamma rays with velocities of v/c = 0.6c. Once Doppler shift corrections have been made, DALI2 has an energy resolution of 10% and a full energy photopeak efficiency of 20% for 1 MeV gamma rays at $v/c = 0.6c$ [55]. A schematic of DALI2 in its typical, 186 crystal configuration is shown in figure 2.12, this differs from the 140 crystal detector by having additional detectors downstream of the target. The 140 crystal setup simply has ring layers of detectors around the beam pipe.

2.4 Data Acquisition

In order to reconstruct the physics observables of each event, all the signals from the detectors were recorded by the **D**ata **AQ**uisition system (DAQ) with a common trigger signal with shared dead time. The trigger pulses have been determined by a combination of four

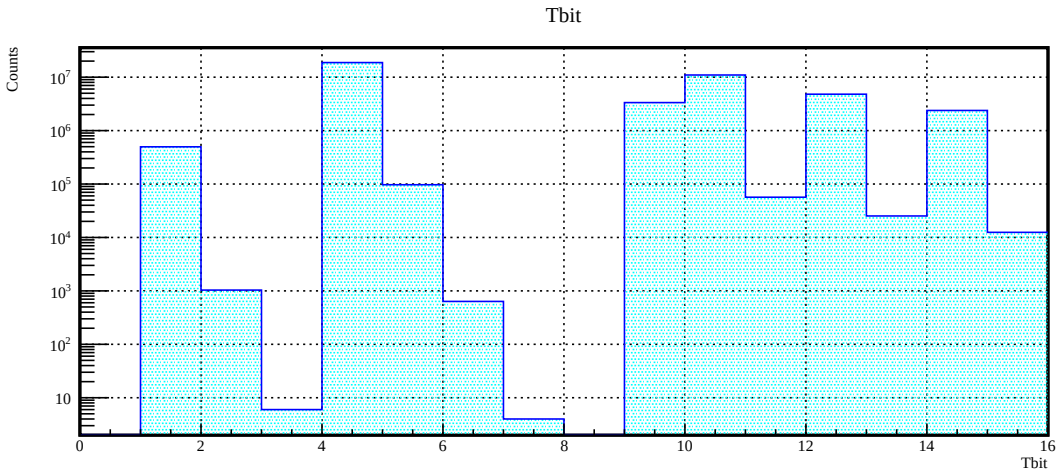

Figure 2.13: An example of the different tbits which correspond to the different triggers and the number of events as a result. See table 2.1 for a summary of what each tbit represents.

different data signals, that are recorded as a trigger bit (tbit) in the data.

The first detector that triggers the DAQ is the **D**own **S**cale **B**eam. This is measured when the beam passes through the two SBTs, located at the start of the SAMURAI spectrometer. Due to the high rate of events, the beam is down scaled by a certain value so that the dead time of the DAQ is minimised. In the case of the first trigger method, the only events that are recorded is the down scale beam, with no coincidence with any other detectors. For the experiment runs that have been analysed, there are two different down scale beam factors. The first factor, for runs 276-283, has a factor of 1/1000, with a beam rate of approximately 1600Hz and a live time of approximately 60%. The other data set, runs 284-310 and 318-325 has a down scale beam factor of 1/200, with a beam rate of approximately 700Hz and a live time of approximately 80%.

A second trigger source is the neutron detector, NEBULA. The different triggers can be combined in different ways to show different reaction channels. For instance, a tbit value of two is the NEBULA trigger. This can be combined with the Down Scale Beam and DALI2 triggers as well as the downstream HODOSCOPE.

The gamma ray detector, DALI2 was used for the third component of the trigger source. Similar to the Down Scale Beam factors, there are two DALI2 downscaling factors. The first factor, for runs 276-283, has a factor of 1/1. The other data set, runs 284-310 and 318-325 has a down scale beam factor of 1/4. For DALI2, a tbit value of four is the DALI2 trigger.

The different tbit values, their assignment and possible combinations are shown in table 2.1. The population of the different combinations of triggers is shown in figure 2.13.

The electronics schemes of the SBTs (figure A.1), HODOSCOPE (figure A.2), DALI2 (figure A.3), NEBULA (figure A.4) and the strobe (figure A.5) are shown in the appendix in section A.1.

Summary of Tbits	
Tbit	**Assignment**
1	Down Scale Beam
2	NEBULA
3	Down Scale Beam + NEBULA
4	DALI2
5	Down Scale Beam + DALI2
6	NEBULA + DALI2
7	Down Scale Beam + NEBULA + DALI2
8	HODOSCOPE
9	Down Scale Beam + HODOSCOPE
10	HODOSCOPE + NEBULA
11	Down Scale Beam + HODOSCOPE + NEBULA
12	HODOSCOPE + DALI2
13	Down Scale Beam + HODOSCOPE + DALI2
14	HODOSCOPE + NEBULA + DALI2
15	Down Scale Beam + HODOSCOPE + NEBULA + DALI2

Table 2.1: Summary of tbits

Chapter 3

Methodology

3.1 Proton Knockout Reactions

The work presented relies on proton knockout reactions, in which a ^{21}N beam is impinged on a target, which in the case of this work, is composed of ^{12}C. When this happens the ^{21}N ion may lose one or more nucleons. In the case of this work, a single proton knockout reaction is selected, which produces ^{20}C. A proton knockout reaction with a carbon target is surface dominated, and therefore the proton removed from the ^{21}N beam is most likely to be from either the $1p_{1/2}$ or $1p_{3/2}$ orbit. With this the ground state or excited 2^+ state can be occupied, as described in more detail in section 3.5.

3.2 Inclusive Cross Section

The investigation of the bound state and proton amplitude in ^{20}C relies primarily on the study of cross sections, both inclusive and exclusive. The use of proton knockout reactions enables the population of both bound and unbound states in ^{20}C. Through this the proton amplitude can be determined. This important value yields information on the structure of ^{20}C, and the prevalence of the Z=6 sub-shell closure as the neutron drip line is approached. In order to determine this, the measurements of the exclusive cross section for the bound 2^+ state and the ground state is necessary, which is discussed below.

3.2.1 Definition of inclusive cross section

In this study, the inclusive cross section is defined as the amount of ^{20}C produced in any bound state from a proton knockout reaction from ^{21}N. This includes the cross sections populating the ground state as well as the known 2^+ state and any other bound states. The inclusive cross section is defined using equation 3.1.

$$\sigma_{inclusive} = \frac{N_{^{20}C}}{n \times N_{^{21}N}} \tag{3.1}$$

Where n is the area density of the target, measured in target nuclei cm^{-2}, given by equation 3.2.

$$n = d.\frac{N_A}{M_{mol}} \tag{3.2}$$

$N_{^{20}C}$ is the amount of outgoing ^{20}C and $N_{^{21}N}$ is the amount of measured incoming ^{21}N using the down scaled beam trigger. In order to convert to millibarns, the value is then multiplied by 1×10^{27}. The area density was determined using the size of the target and its mass. According to the logbook of the experiment, the carbon target has dimensions of 85.050×85.050×10.011 mm^3, with a deviation in the thickness of the target of ± 0.003 mm [56]. The mass of the target is 129.431 g, which results in a density of 1.789±0.005 gcm^{-2}. Converting the density to area density using equation 3.2, the area density is calculated to be (8.970±0.027)× 10^{22} target nuclei cm^{-2}.

The values used in equation 3.1 assume that all detectors are 100% efficient and that transmission of beam to target and fragments from target to the HODOSCOPE is perfect, which is not the case. These values represent the number of ions measured using the down-scale beam, before any correction to account for the efficiency of the transmission of fragments from the target to the HODOSCOPE. It also assumes that there is no interaction of the beam in other materials, either before the target or unreacted ^{21}N in material after the target. Therefore modifications to the equation 3.1 are needed to account for this.

It is then necessary to consider the transmission efficiency from the target to the HODOSCOPE and the loss of reaction products within the target. To account for these effects, the amount of incoming and outgoing ^{21}N was compared for target runs and the empty target runs [57]. This is done using the down scale beam trigger. The transmission is discussed in more detail in section 4.6. Including the transmission factor, the inclusive cross section becomes equation 3.3.

$$\sigma_{inclusive} = \frac{N_{^{20}C}}{n.N_{^{21}N}.T} \tag{3.3}$$

Where T is the transmission factor and n is the area density of the target, shown in equation 3.2.

3.3 Exclusive Cross Section

This is a measurement of the amount of ^{20}C produced in a specific state. In the case of this work, ^{20}C is only known to have a single bound excited state which is the 2^+ state at approximately 1620 keV. Using measurements of the γ-ray transition from the 2^+ state to the ground state observed by DALI2, combined with a response function of DALI2 generated by GEANT4 from calibration data, the amount of population to the 2^+ state can be estimated. The cross section is determined by 3.4.

$$\sigma_{2^+} = \frac{N_{^{20}C^{2+}}}{n.N_{^{21}N}.T} \tag{3.4}$$

Similarly, in order to determine the proton amplitude, discussed later, the exclusive cross section of the ground state needs to be determined. As ^{20}C is only known to have a single bound excited state, and the inclusive cross section is defined as the amount of ^{20}C produced in a bound state, i.e. the ground state or the single excited state, the exclusive cross section of the ground state is given by equation 3.5.

$$\sigma_{g.s.} = \sigma_{inclusive} - \sigma_{2^+} \tag{3.5}$$

The discussion of how the cross section is determined is discussed in section 5.2. The identification of the excited state is determined using DALI2, and the gamma rays produced need to be Doppler corrected due to the relativistic velocities of the beam and fragments.

3.4 Doppler correction

In the experiment, the beam is at very high energies, with a velocity of $0.63c$, corresponding to an energy of 345 MeV/nucleon. As a result, the secondary beam is also at very high energies, so as a result, Doppler corrections of the emitted gamma rays are necessary to determine energies in the rest frame. To convert between the observed energies and energies in the rest-frame, equation 3.6 is used.

$$\frac{E_\gamma}{E_{\gamma 0}} = \frac{\sqrt{1-\beta^2}}{1-\beta\cos\theta_\gamma} \tag{3.6}$$

Where E_γ is the observed gamma energy, $E_{\gamma 0}$ is the gamma energy in the rest frame, $\beta = \frac{v}{c}$ is the velocity of the ion as a percentage of the speed of light, determined using the incoming beams time of flight. θ_γ is the scattering angle of the outgoing particle [58], which is the angle between the target and the geometrical centre of the DALI2 crystal that is hit. The angle is modified in order to take the angle of the outgoing ion relative to the Z axis, and the

gamma ray that it may emit. The Doppler corrected resolution is then evaluated with the error propagation using equation 3.7.

$$\left(\frac{\Delta E_{\gamma 0}}{E_{\gamma 0}}\right)^2 = \left(\frac{\beta \sin\theta_\gamma}{1-\beta\cos\theta_\gamma}\right)^2 \times (\Delta\theta_\gamma)^2 + \left(\frac{\beta-\cos\theta_\gamma}{(1-\beta^2)(1-\beta\cos\theta_\gamma)}\right)^2 \times (\Delta\beta)^2 + \left(\frac{\Delta E_{intr}}{E_\gamma}\right)^2 \quad (3.7)$$

Where ΔE_{intr} is the uncertainty in the emitted γ-rays energy.

3.5 Proton amplitude

In order to develop the framework which will be used in this work, it is important to consider the excited states of other neutron rich nuclei such as carbon and oxygen. The first nuclei that is examined is ^{16}O, which is doubly magic with Z and N=8. The first 2^+ state has an energy of 6.9171 MeV [25], see figure 3.1. This is a very high excitation energy, attributed to the fact that ^{16}O is a doubly magic nuclei. Similarly, when two protons are removed, measurements of the first excited 2^+ state in ^{14}C shows a similar energy at 7.012 MeV. It is expected that ^{14}C would be singularly magic with respect to the neutrons (N=8), however the high excitation energy, indicates that the Z=6 sub-shell closure, discussed previously in section 1.3.2, forms at ^{14}C, making the nucleus doubly magic. The excited state is interpreted as a proton excitation of the ground state by measuring the angular distributions [26]. With the addition of two neutrons to ^{16}O, the first 2^+ state in ^{18}O has a much lower energy at 1.982 MeV. This is interpreted as the excitation of the two additional neutrons outside of the doubly magic ^{16}O core [59].

The excited state in ^{20}C is described by a mixing of pure proton and pure neutron excitations. In figure 3.1 the excitation energy of ^{14,16}C and ^{16,18}O is shown. In the case of ^{16}C, which has two more neutrons, and two fewer protons compared to ^{16}O, the excited 2^+ states can be described by the mixing of the pure proton excitation in ^{14}C and pure neutron excitation in ^{18}O. Experimentally, the first excited 2^+ state is seen at 1.762 MeV [42]. It is expected that there will be an additional 2^+ state at approximately 7 MeV, as seen in ^{14}C, which is well above the neutron separation energy of 4.250 MeV [60]. In the case of ^{20}C, the excited 2^+ states are expected to be similar to the excited 2^+ states in ^{16}C. This is due to the neutrons filling the degenerate *sd* orbit. It is also expected to be dominated by neutron excitation due to the large energy separation between the $1p_{3/2}$ and $1p_{1/2}$ orbit, which is on the order of several MeV [61, 38].

In figure 3.2, the top panel shows the population of different orbits for protons and neutrons in the ground state of ^{21}N. In this experiment, when measuring the proton amplitude, the focus is on the protons, which are seen on the left of each of the panels. The proton

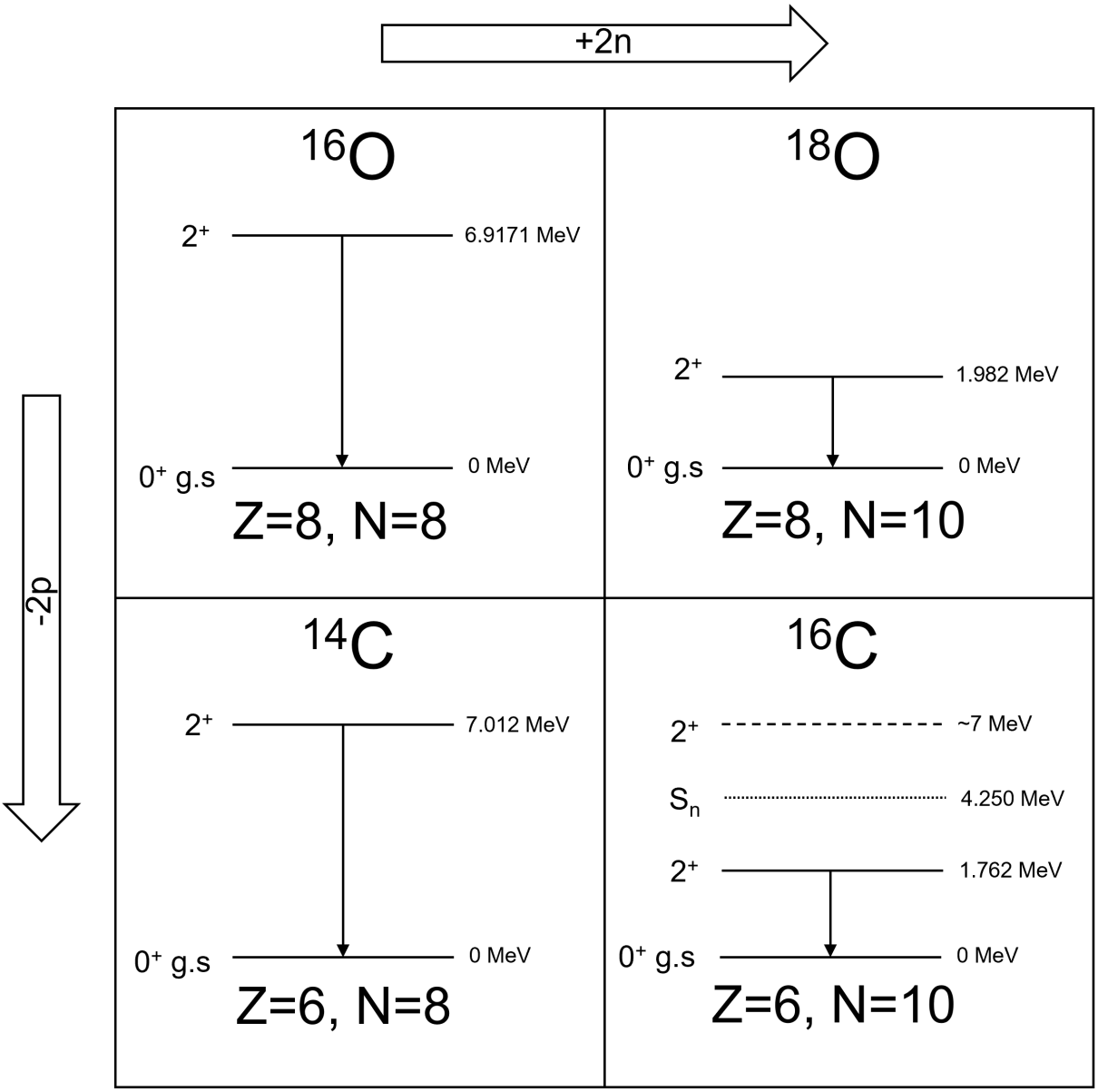

Figure 3.1: The evolution of 2^+ energies with the addition of neutrons and removal of protons. The excited states shown are found in references [25, 26, 59, 60, 42]. ^{16}O which is doubly magic and ^{14}C, which is also doubly magic due to the formation of the Z=6 sub-shell closure exhibit a characteristically high 2^+ energy at approximately 7 MeV, with the excited state attributed to proton excitation. ^{18}O, which is interpreted as a closed ^{16}O core with two valence neutrons exhibits a much lower 2^+ excitation energy, attributed to the excitation of the two valence neutrons. It is expected that the 2^+ states in ^{16}C will be a mixing of pure proton and pure neutron excitation, which gives rise to the two states shown, one measured experimentally at 1.762 MeV by [42], and one above the neutron separation energy. The excited states of ^{20}C is expected to follow the same pattern due to the neutrons filling the degenerate sd shell. The figure is based on figure three produced in reference [62].

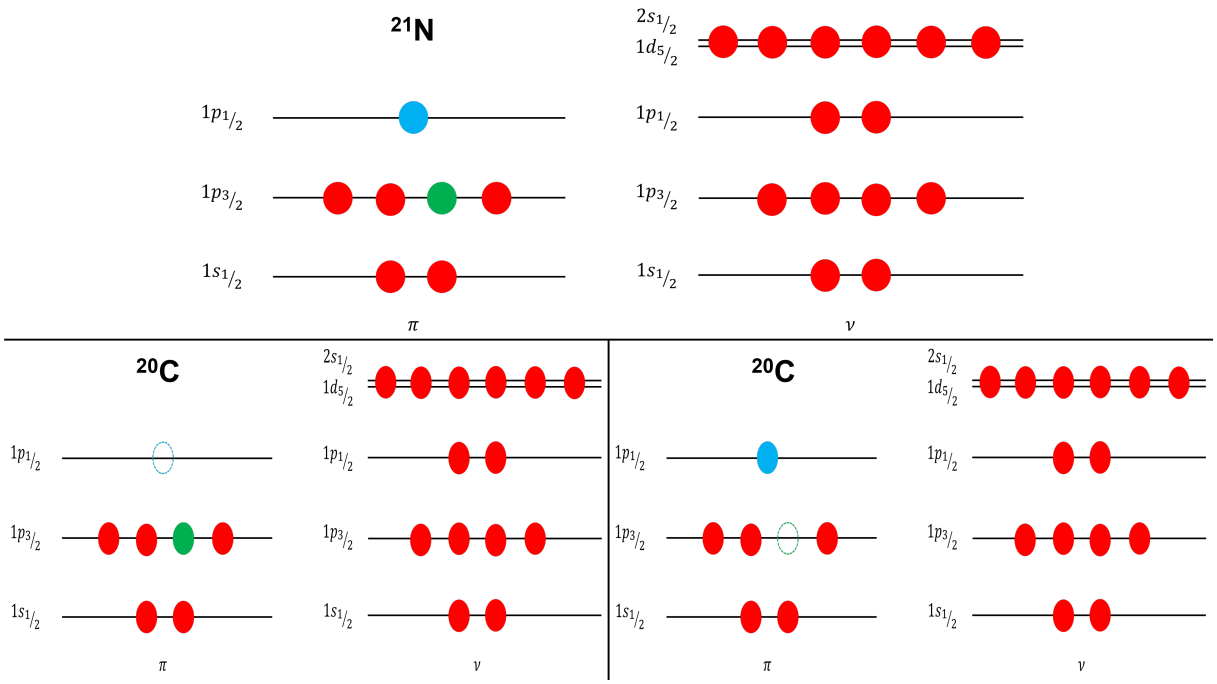

Figure 3.2: In the top panel, the population of levels is shown for the ground state of ^{21}N, with the protons on the left and the neutrons on the right. The bottom two panels show the possible configuration of protons and neutron in ^{20}C following a proton knockout reaction from ^{21}N.

knockout reaction is dominated by the knockout of surface protons [63], and therefore the proton removed is most likely to be from either the $1p_{1/2}$, which is shown in blue, or $1p_{3/2}$ orbit, shown in green. In the case of the $1p_{3/2}$ orbit, any of the four protons could be knocked out, however for ease of viewing, only one is highlighted in figure 3.2. In the case of the removal of a $1p_{3/2}$, as seen in the lower right panel, it is possible that a 2^+ or 1^+ state will be produced. In the lower left panel of figure 3.2, the ground state of ^{20}C is shown following the knockout of the proton from the $1p_{1/2}$ orbit.

As has been mentioned earlier in this section, the excited 2^+ state can be described by a mixing of pure proton and pure neutron excitations. The mixing of two excitations via an interaction V, is described by the matrix equation 3.8 [64, 65].

$$\begin{pmatrix} E_1 & V \\ V & E_2 \end{pmatrix} \cdot \begin{pmatrix} \phi_I \\ \phi_{II} \end{pmatrix} = \begin{pmatrix} E_I \\ E_{II} \end{pmatrix} \cdot \begin{pmatrix} \phi_I \\ \phi_{II} \end{pmatrix} \tag{3.8}$$

When applied to the situation of ^{20}C, in the context of mixing pure proton and pure neutron states, this leads to two excited 2^+ states, shown in equation 3.9 and 3.10.

$$\left|2_1^+\right\rangle = \alpha \left|2^+\right\rangle_\nu + \beta \left|2^+\right\rangle_\pi \tag{3.9}$$

$$\left|2_2^+\right\rangle = -\beta\left|2^+\right\rangle_\nu + \alpha\left|2^+\right\rangle_\pi \tag{3.10}$$

Where α and β are mixing amplitudes which denote the amount of pure proton (proton amplitude) and pure neutron (neutron amplitude) excitation respectively, where $\alpha^2+\beta^2=1$. In this work, the objective is to determine the amount of pure proton excitation, the proton amplitude, in the first 2^+ state of ^{20}C, which can be accessed through the proton knockout reaction from ^{21}N.

Referring to figure 3.2, the ground state of ^{21}N can be described by equation 3.11, where n is the number of neutrons in the degenerate sd orbit for the carbon isotope of interest.

$$\left|{}^1/_2{}^-_{g.s.};{}^{21}N\right\rangle = \left|\nu(sd)^6; J=0\right\rangle \otimes \left|\pi\left(1p_{3/2}\right)^4\left(1p_{1/2}\right)^1; J={}^1/_2\right\rangle \tag{3.11}$$

Referring to the lower left panel of figure 3.2, the removal of the $1p_{1/2}$ proton in ^{21}N results in the population of the ground state of ^{20}C. As discussed earlier, there is evidence for the Z=6 sub-shell closure in neutron rich carbon isotopes, and there is a closed shell for neutrons at N=8, resulting in the neutrons filling the degenerate sd shell. With this in mind, the ground state can be described, as done by Macchiavelli et al. [32] by equation 3.12.

$$\left|0^+;{}^A C\right\rangle = \left|\nu(sd)^n; J=0\right\rangle \otimes \left|\pi(p_{3/2})^4; J=0\right\rangle \tag{3.12}$$

The lower right panel of figure 3.2 shows the removal of a proton from the $1p_{3/2}$ orbit in ^{21}N. This can result in the population of the 2^+ state in ^{20}C, and taking the mixing of pure neutron and pure proton excitation, the 2^+ state can be described by equation 3.13.

$$\begin{aligned}\left|2_1^+;{}^A C\right\rangle = \alpha\left|\nu(sd)^n; J=2\right\rangle \otimes \left|\pi(p_{3/2})^4; J=0\right\rangle \\ +\beta\left|\nu(sd)^n; J=0\right\rangle \otimes \left|\pi(p_{3/2})^3(p_{1/2})^1; J=2\right\rangle\end{aligned} \tag{3.13}$$

The determination of the proton amplitude is accessed through a proton knockout reaction. This is done through the comparison of the spectroscopic factors of the states that are produced. This can be approximated by the comparison of the exclusive cross sections of the excited state and the ground state, as shown in equation 3.14. As illustrated in figure 3.2, protons in two different orbits are assumed to be involved in the reaction. If the proton is knocked out from the $1p_{1/2}$ orbit, shown in the lower left panel in blue, the ground state of ^{20}C is produced. As this reaction only knocks out a single proton, the spectroscopic factor is expected to be one. The knockout of the proton in the $1p_{3/2}$ orbit, shown in the lower right panel in green can populate the 2^+ state of ^{20}C. However the 2^+ state is not the only state that can be populated. Referring to equation 1.5, the 2^+ state has the highest angular momentum that is possible combining the angular momentum of the $1p_{3/2}$ and $1p_{1/2}$ proton. However they can also combine to produce a 1^+ state. The multiplicity of a state, which

describes the number of configurations of nucleons that can produce a given state, is given by 2J+1. Therefore the 2^+ state has a multiplicity of five ((2×2)+1), while the 1^+ state has a multiplicity of three ((2×1)+1). The removal of the proton in the $1p_{3/2}$ orbit can result in the population of a state in eight possible configurations, with the 2^+ state populated five out of eight times. As there are four protons in the $1p_{3/2}$ orbit, the ratio of the spectroscopic factors is proportional to the square of the proton amplitude as shown in equation 3.14 [33].

$$\frac{C^2S(2_1^+)}{C^2S(2_{g.s.}^+)} \approx \frac{\sigma_{2^+}}{\sigma_{g.s.}} \approx \frac{\beta^2 \times 4 \times {}^5/_8}{1} \approx \beta^2 \times {}^5/_2 \tag{3.14}$$

The spectroscopic factors in equation 3.14 are the relationships between the experimentally determined exclusive cross sections, and the cross section from reaction theory [65]. The spectroscopic factor of the 2^+ state and the ground state is given by equation 3.15 and 3.16.

$$C^2S\left(2_1^+\right) = \frac{\sigma_{exp}\left(2_1^+\right)}{\sigma_{theory}\left(1p_{3/2}\right)} \tag{3.15}$$

$$C^2S\left(0_{g.s.}^+\right) = \frac{\sigma_{exp}\left(0_{g.s.}^+\right)}{\sigma_{theory}\left(1p_{1/2}\right)} \tag{3.16}$$

As the protons in the $1p_{3/2}$ and $1p_{1/2}$ orbits are deeply bound, and have the same angular momentum ($l = 1$) [65], the theoretical cross sections are assumed to be approximately equal to one another, and therefore cancel out. As a result the proton amplitude can be extracted from the relation of the exclusive cross section of the 2^+ state and the ground state, as shown in equation 3.17.

$$\beta^2 \approx \frac{\sigma_{2^+}}{\sigma_{g.s.}} \times \frac{2}{5} \tag{3.17}$$

As the proton and neutron components of the 2^+ state are orthogonal, it is expected that there will be another 2^+ state, described by I. Syndikus [65] by equation 3.18.

$$\begin{aligned} \left|2_2^+;{}^A C\right\rangle = &-\beta \left|\nu(sd)^n; J=2\right\rangle \otimes \left|\pi(p_{3/2})^4; J=0\right\rangle \\ &+\alpha \left|\nu(sd)^n; J=0\right\rangle \otimes \left|\pi(p_{3/2})^3(p_{1/2})^1; J=2\right\rangle \end{aligned} \tag{3.18}$$

Chapter 4

Data Analysis

In order to perform the investigation of the bound 2^+ state and the proton amplitude in ^{20}C, the experimental runs dayone0276-0310 and dayone0318-0325 using a carbon target and a ^{21}N beam were analysed. A summary of the experiment runs is listed in table 4.1. These runs used a beam centred on ^{23}O/^{22}N. Within this beam, ^{21}N is present, making up approximately 40% of the incoming beam. The incoming ^{21}N is impinged onto the carbon target, undergoing a proton knockout reaction to produce ^{20}C. The empty target runs dayone0311-0317 were also analysed. Table 4.2 summarises the different runs using the ^{23}O/^{22}N beam on a carbon target that were used to measure the proton amplitude of ^{20}C. The first step that was performed was to identify the incoming beam using the ToF-Bρ-ΔE method. This is described in section 4.1.

In order to perform the calibrations detailed in this section, the data runs shown in table 4.3 are used.

4.1 Incoming beam analysis

4.1.1 Time Calibration of TDC Modules for Plastic Counters

Calculating the time of flight of the incoming beam is necessary for the determination of the A/Z. It is necessary for time information to be determined at two different locations. These are the plastics at F3, and the SBTs at F13. The SBTs are at the entrance point of the beam from BigRIPS into the experiment hall, and are used as a trigger for the experiment.

The first step to calibrating the detectors is to analyse a run which uses a pulser. This is done to convert from the raw TDC to real time. It is necessary to do this for both the left and right detector in F3 and the left and right detectors in both of the SBTs. The run used was dayone0433, which produces pulses that are separated by 10 ns. The first step to determine the parameters was to plot the raw time and then use a peak detection algorithm

Summary of Day-One Campaign runs		
Runs	**Dates**	**Purpose**
0001-0057	03/05/12 - 07/05/12	Detector Calibrations
0058-0090	07/05/12 - 08/05/12	^{22}C beam on carbon target
0091-0094	08/05/12 - 09/05/12	Detector Calibrations
0095-0112	09/05/12 - 09/05/12	^{22}C beam on empty target
0113-0166	09/05/12 - 12/05/12	^{22}C beam on lead target
0167-0176	12/05/12 - 13/05/12	^{22}C beam on carbon target
0177-0178	13/05/12 - 13/05/12	^{20}C beam on carbon target
0179-0180	13/05/12 - 13/05/12	^{20}C beam on lead target
0181-0187	13/05/12 - 13/05/12	^{20}C beam on empty target
0188-0204	13/05/12 - 13/05/12	Detector Calibrations
0205-0206	13/05/12 - 13/05/12	^{24}O beam on empty target
0207-0208	13/05/12 - 13/05/12	^{24}O beam on carbon target
0209-0224	14/05/12 - 14/05/12	Detector Calibrations
0225-0252	14/05/12 - 14/05/12	^{28}Ne/^{27}F beam on carbon target
0253-0258	14/05/12 - 15/05/12	^{28}Ne/^{27}F beam on empty target
0259-0273	15/05/12 - 15/05/12	^{28}Ne/^{27}F beam on carbon target
0274-0275	15/05/12 - 15/05/12	Detector Calibrations
0276-0310	15/05/12 - 16/05/12	^{23}O/^{22}N beam on carbon target
0311-0317	16/05/12 - 16/05/12	^{23}O/^{22}N beam on empty target
0318-0325	16/05/12 - 16/05/12	^{23}O/^{22}N beam on carbon target
0326-0332	16/05/12 - 16/05/12	Detector Calibrations
0333-0349	16/05/12 - 17/05/12	^{20}N/^{19}C beam on carbon target
0350-0352	17/05/12 - 17/05/12	^{20}N/^{19}C beam on empty target
0353-0355	16/05/12 - 17/05/12	^{20}N/^{19}C beam on lead target
0356-0358	25/05/12 - 25/05/12	Detector Calibrations
0359-0388	25/05/12 - 26/05/12	^{27}Ne/^{26}F beam on carbon target
0389-0392	26/05/12 - 26/05/12	^{27}Ne/^{26}F beam on empty target
0393	26/05/12	Detector Calibrations
0394-0404	26/05/12 - 27/05/12	^{19}B beam on carbon target
0405-0409	27/05/12 - 27/05/12	^{19}B beam on empty target
0410-0427	27/05/12 - 28/05/12	^{19}B beam on lead target
0428-0436	28/05/12 - 28/05/12	Detector Calibrations

Table 4.1: Summary of Day-One experiment

Run	Target	Total Time (minutes)	Beam Downscaling	NEBULA Downscaling	DALI2 Downscaling
275	carbon	17	1/1	1/1	1/1
276-283	carbon	232	1/1000	1/1	1/1
284-310	carbon	835	1/200	1/1	1/4
311	empty	18	1/200	1/1	1/4
312-317	empty	260	1/50	1/1	1/2
318	carbon	31	1/200	1/1	1/4
321-325	carbon	163	1/200	1/1	1/4

Table 4.2: Summary of ^{23}O/^{22}N beam downscaling information.

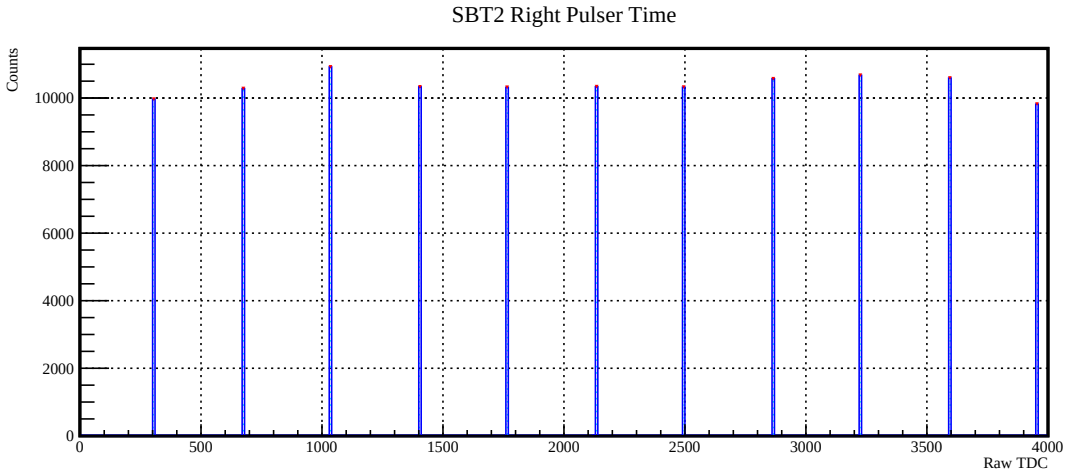

Figure 4.1: An example of the peak detection used to determine the location of the 10 ns pulses, which enables the conversion from the raw time channel to calibrated time.

to determine the location of the peaks. An example for the left detector in SBT1 is shown in figure 4.1.

These peaks are then fitted against the corresponding time to get the conversion factors for converting from the raw time channel to the calibrated time, which is shown in figure 4.2.

4.1.2 SBT Slew Correction

The slew correction is necessary due to the use of leading edge discriminators, which are used to process the analogue signal from the PMT into logic pulses for the TDC modules. The pulse timing has a dependency with the amplitude of the signal, which is dependent on the charge of the ion that interacts in the plastic, where the energy deposited in the plastics is proportional to the square of the atomic number (Z) of the ion and the square root of the velocity. A QDC module is used to measure the charge output. As the beam should be coming in at approximately the same velocity, regardless of the ions charge, the most important effect for the energy deposited in the plastics is the charge. As a result of this

Run	Target	Total Time (minutes)	Downscaling	Purpose
dayone 0433	N/A	4	DSB: 1/1	TCal (pulser) run for Plastics (range: 320 ns, period: 10 ns)
dayone 0435	N/A	12	DSB: 1/1	TCal (pulser) run for HOD/NEBULA (range: 320 ns, period: 10 ns)
dayone 0312 - 0317	Empty	260	DSB: 1/50, NEBULA: 1/1, DALI2: 1/2	Empty runs, used to align BDC2 relative to BDC1 and FDC1
calib 0221 - 0222	N/A	25	DALI2: 1/1	DALI2 ^{60}Co calibration runs
calib 0237 - 0238	N/A	42	DALI2: 1/1	DALI2 ^{88}Y calibration runs
calib 0244	N/A	9	DALI2: 1/1	DALI2 ^{22}Nax2 calibration run
calib 0251	N/A	94	DALI2: 1/1	DALI2 background run
calib 0254	N/A	11	DALI2: 1/10	DALI2 ^{137}Csx2 calibration run
calib 0257	^{22}Na	30	DALI2: 1/10	DALI2 ^{22}Na efficiency run to verify simulation
calib 0262	^{88}Y	70	DALI2: 1/1	DALI2 ^{88}Y efficiency run to verify simulation
NEBULA 0003	N/A	8	NEBULA: 1/1	NEBULA pedestal run
NEBULA 0004 - 0007	N/A	1197	NEBULA: 1/1	NEBULA cosmic ray runs with 3 T SAMURAI field
NEBULA 0015 - 0017	N/A	678	NEBULA: 1/1	NEBULA cosmic ray runs with 3 T SAMURAI field
NEBULA 0022 - 0024	N/A	1606	NEBULA: 1/1	NEBULA cosmic ray runs with 3 T SAMURAI field
NEBULA 0026 - 0028	N/A	547	NEBULA: 1/1	NEBULA cosmic ray runs with 3 T SAMURAI field
NEBULA 0035	N/A	40	NEBULA: 1/1	NEBULA cosmic ray runs with 3 T SAMURAI field
NEBULA 0007 - 0014	N/A	118	NEBULA: 1/1	Am-Be gamma ray runs with 3 T SAMURAI field
NEBULA 0029 - 0034	N/A	182	NEBULA: 1/1	Am-Be gamma ray runs with 3 T SAMURAI field
dayone 0049 - 0054	Al	155	DSB: 1/1000, NEBULA: 1/1, DALI2: 1/1	^{15}C->Al High energy gamma ray + neutron runs with 3 T SAMURAI field

Table 4.3: Summary of calibration runs.

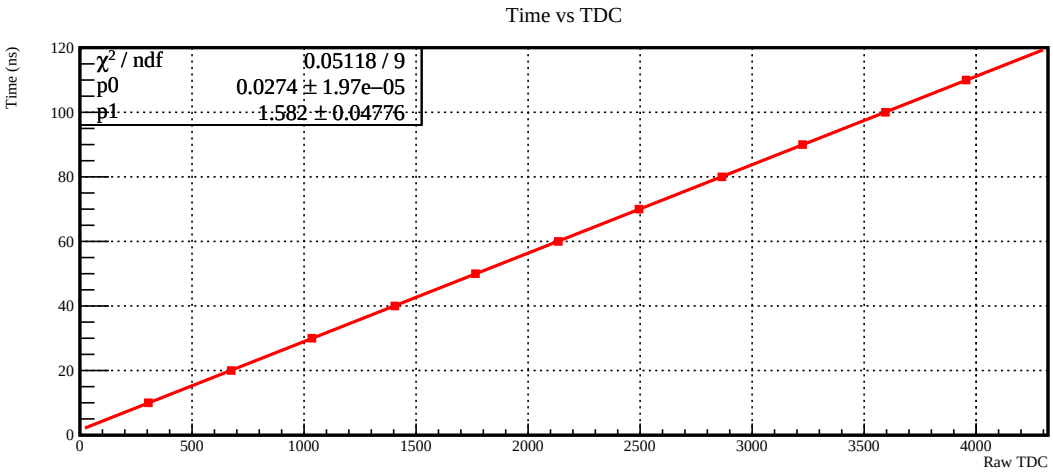

Figure 4.2: The fitted location of the 10 ns pulses against time.

dependency, the ions with a higher charge produce a larger signal, which is detected faster. An example of the effect is shown in figure 4.3.

As can be seen, the relation between the time and raw charge approximates a quadratic function. Therefore it can be corrected using equation 4.1.

$$T_{slew} = T_{cal} - \left(\frac{A}{\sqrt{Q_{raw}}} + B \right) \tag{4.1}$$

Where T_{cal} is the difference in calibrated time between SBT1 and SBT2 shown in equation 4.2.

$$T_{cal} = \left(\frac{TL_2 + TR_2}{2} \right) - \left(\frac{TL_1 + TR_1}{2} \right) \tag{4.2}$$

A and B are fit parameters determined from figure 4.4, and Q_{raw} is the averaged raw charge collected in either SBT1 or SBT2, shown in equation 4.3.

$$Q_{Raw} = \sqrt{QL_{raw}.QR_{raw}} \tag{4.3}$$

By applying equation 4.1 to the calibrated time, the slew effect can be corrected, as seen in figure 4.5.

4.1.3 SBT Beam Position Dependency

The incoming beam is distributed in space and angle, and as a result the position of the beam within the SBTs has an effect on both the timings (resulting in worse timing resolution) for incoming and outgoing fragment A/Z. When looking at the raw time within the SBTs, the left detector shows a single peak, while the right detector shows a broad distribution.

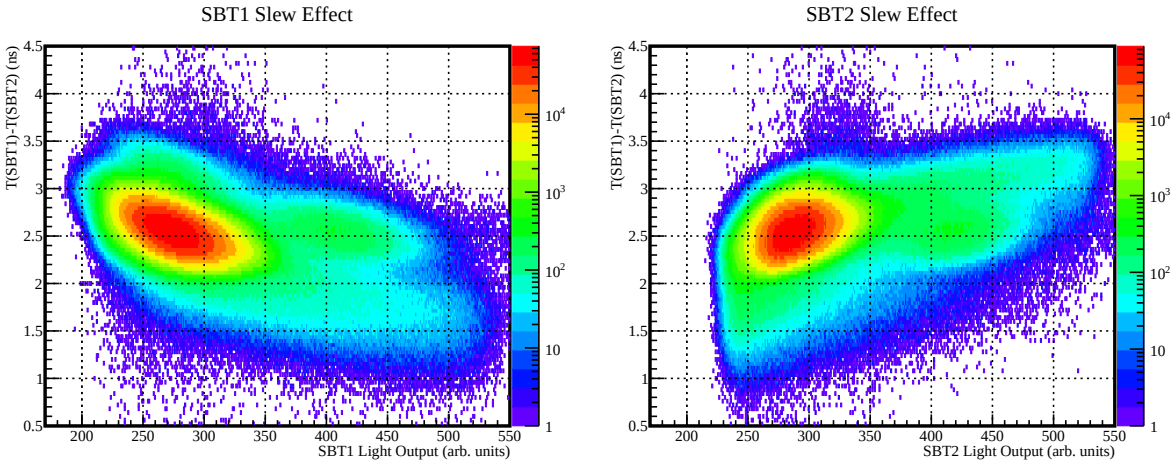

Figure 4.3: The difference in time between SBT1 and SBT2, plotted against the raw charge in SBT1 in the left panel and the raw charge in SBT2 in the right panel. The slew effect is shown as for a smaller charge, the time difference is larger, therefore the smaller charge is detected slower.

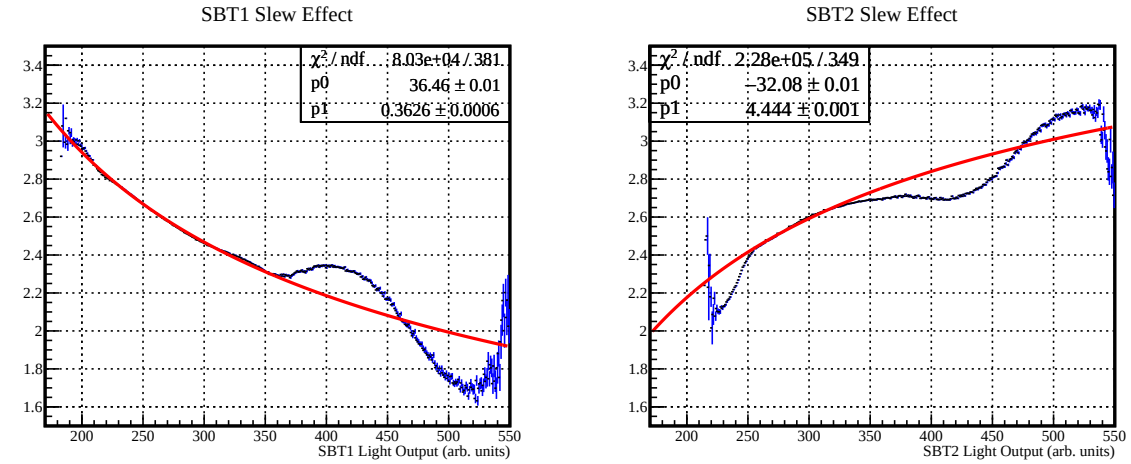

Figure 4.4: The fitting of the difference in time between SBT1 and SBT2, plotted against the raw charge in SBT1 in the left panel and the raw charge in SBT2 in the right panel, shown in figure 4.3. The increase in the time difference, shown in the left panel at an SBT1 light output between 360-450, is likely the result of events piling up.

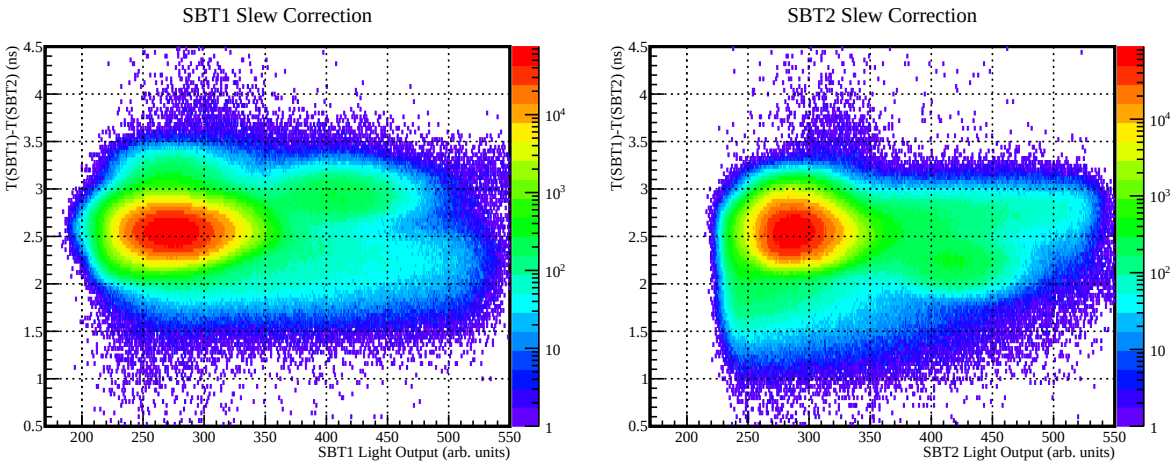

Figure 4.5: The difference in the slew corrected time between SBT1 and SBT2, plotted against the average raw charge in SBT1 in the left panel and the raw charge in SBT2 in the right panel. As can be seen compared to the previous figure, the slew effect has been significantly reduced.

The single peak in the left detector is because, in the case of the SBTs, the left detector is used to determine the timing of the trigger. In order to correct for this, the position of the beam within the SBTs needs to be accounted for. Figure 4.6 is an example of the position dependency of the beam within the plastics.

This position dependency is then fitted with a 4^{th} order polynomial shown in equation 4.4.

$$T_{position\ correction} = T_{slew} - \left((A \times dT^4) + (B \times dT^3) + (C \times dT^2) + (D \times dT) + E\right)$$
$$where: \tag{4.4}$$
$$dT = T_R - T_L$$

Where A, B, C, D and E are the fitting parameters, which is shown in figure 4.7.

The fit in figure 4.7 was chosen by comparing the full width half max (FWHM) of the time after correcting with different order fittings of the data shown in figure 4.7. In order to test which fitting of the data was the best, the data was fitted in three different ways, first the entire incoming beam was fitted with the various orders of polynomial fits; secondly only incoming ^{21}N was fitted with the various orders of polynomial fits; and finally, incoming ^{21}N with a cut on the target position was fitted. To determine the best fitting, the FWHM of the time difference between the SBTs was compared. The result of the different fittings is shown in table 4.4, and the effect of the fitting using the fourth order polynomial is shown in figure 4.8.

The different time measurements were compared to determine the improvement in the resolution. This was done by plotting the original time, slew time and position corrected

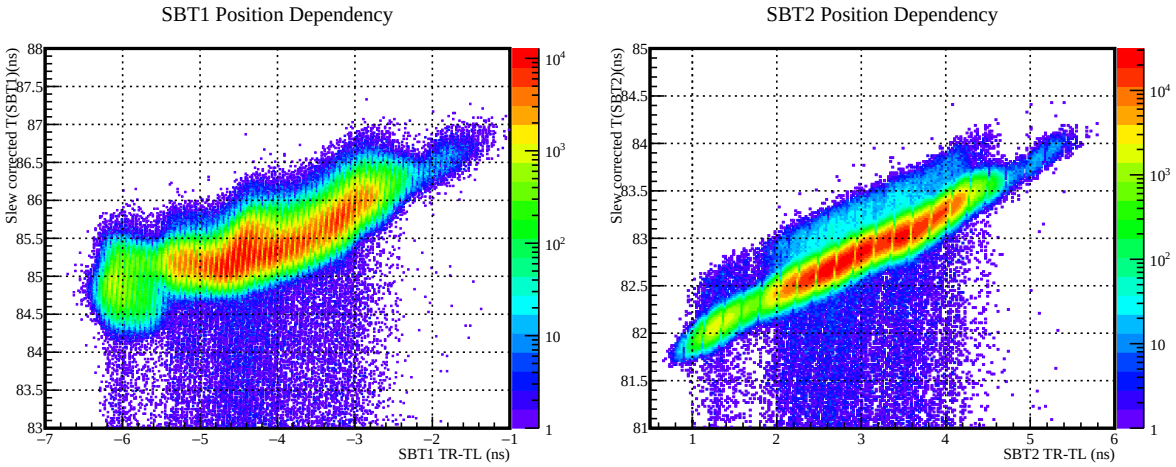

Figure 4.6: The slew corrected time in the SBTs, plotted against the difference in time between the right and left detector.

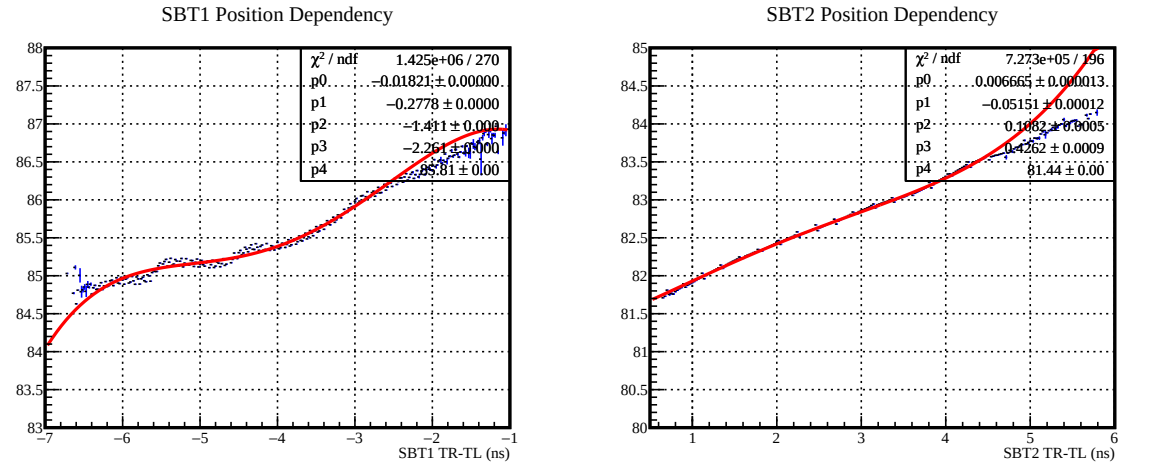

Figure 4.7: A 4^{th} order polynomial fitting of the slew corrected time in the SBTs, plotted against the difference in time between the right and left detector.

Comparison of SBT Position Time Corrections			
Correction	**TDiff (All incoming beam) FWHM (ns)**	**TDiff (^{21}N) FWHM (ns)**	**TDiff (^{21}N and TC) FWHM (ns)**
Original Time	0.441	0.441	0.441
Slew Time	0.301	0.301	0.301
Pol 1	0.329	0.343	0.343
Pol 2	0.273	0.28	0.294
Pol 3	0.28	0.28	0.287
Pol 4	0.28	0.266	0.287
Pol 5	0.336	0.266	0.287

Table 4.4: Comparison of SBT Position Time Corrections.

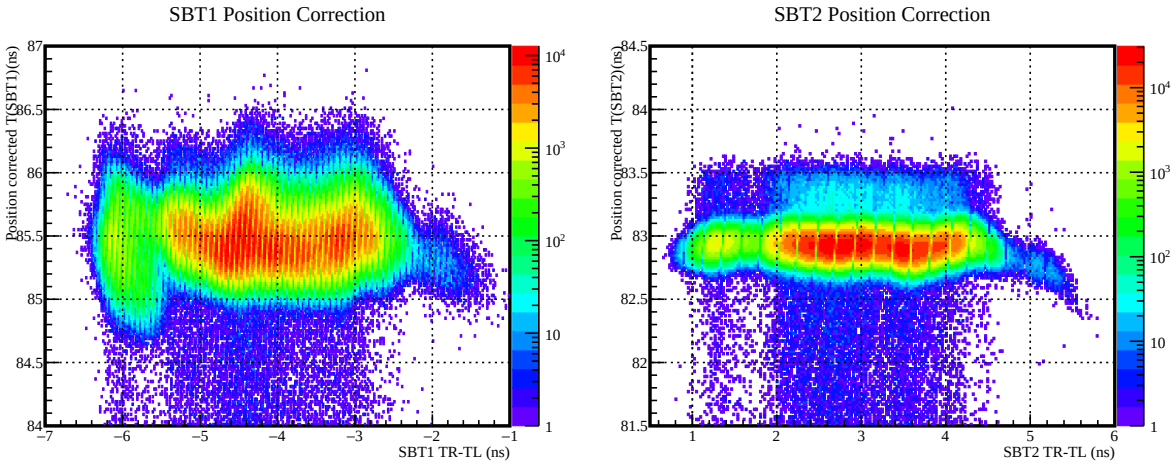

Figure 4.8: The position corrected time in the SBTs, plotted against the difference in time between the right and left detector.

time, and calculating the FWHM of the peaks, for both SBT1 and 2. An example is shown in figure 4.9.

A comparison of the FWHM is shown in table 4.5. For SBT1, the slew correction only shows a modest improvement in resolution. This is because SBT1 acts as the trigger, so has a narrower peak. SBT2 shows a decrease in resolution, this is due to the unusual signal from the original SBT2 time. The position correction shows a significant improvement in the time resolution, roughly halving the FWHM for both SBT1 and SBT2.

4.1.4 SBT Time Offset

The final step in calibrating the time of flight for the incoming beam was determining the offset that is required to properly reconstruct the A/Z of the incoming beam. By selecting on the correlated charge at F3 and the SBTs, it is possible to restrict the incoming beam to just nitrogen. The beam composition has been determined in previous work, with ^{21}N and

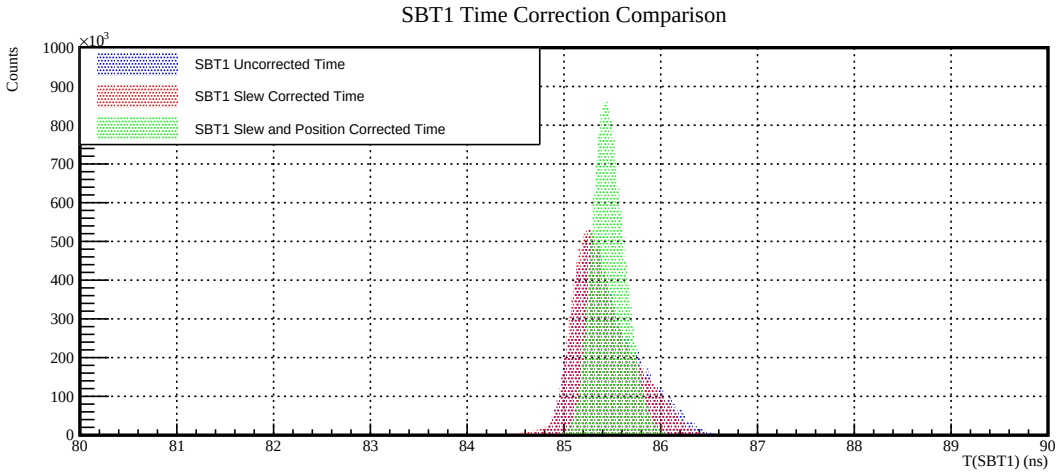

Figure 4.9: A comparison of the time (blue), slew corrected time (red) and position corrected time (green). As can be seen, the position corrected time shows a significantly sharper peak compared to the original time and the slew corrected time.

Comparison of SBT Time Corrections		
Correction	**SBT1 FWHM (ns)**	**SBT2 FWHM (ns)**
Original Time	0.75	0.225
Slew Corrected Time	0.705	0.465
Position Corrected Time	0.345	0.15

Table 4.5: The improvement in the FWHM of the time in the two SBTs, with the different corrections applied.

^{22}N representing most of the beam (99%) when selecting on incoming nitrogen. Therefore, as the two largest peaks in A/Z are known, the timing can be adjusted so that the different isotopes have the correct A/Z.

4.1.5 Bρ using beam proportional chamber (BPC)

The magnetic rigidity of the incoming beam is determined from the position of hits within the BPC, located at F5 within BigRIPS. The magnetic rigidity of the incoming ions is determined using equation 4.5 [66].

$$B\rho = B\rho_{BPC}\left(1+\frac{x}{d}\right) \tag{4.5}$$

Where $B\rho_{BPC}$ is the rigidity of the central trajectory determined at the previous dipole in BigRIPS, x is the X position of the beam within the detector, and d is the momentum dispersion, 33 mm / % [54].

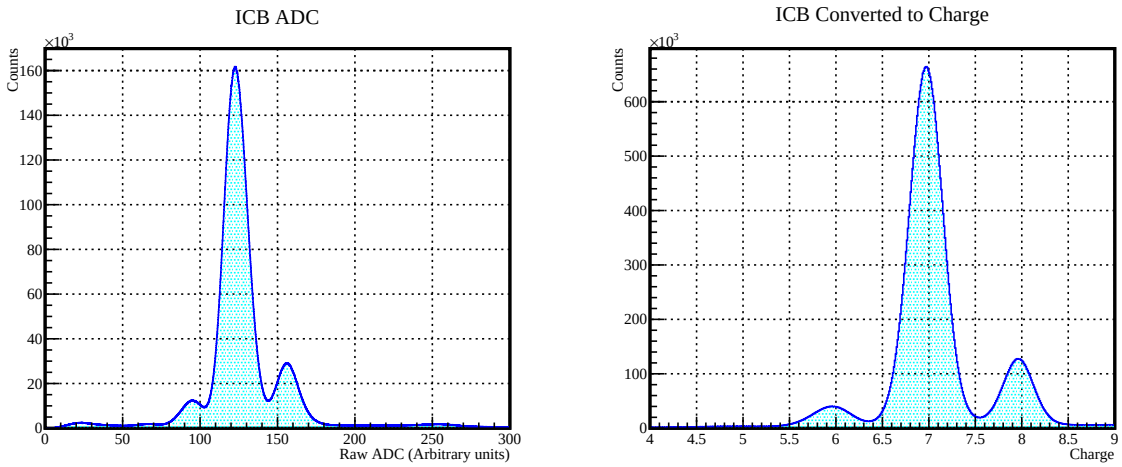

Figure 4.10: The left panel shows the raw ADC deposition in the ICB used to determine incoming Z value. The three peaks represent the three main elements in the beam, carbon, nitrogen and oxygen, with lower charge elements depositing less energy. The right panel shows the result of the calibration, resulting in the conversion from ADC to incoming beam charge.

4.1.6 ΔE using ion chamber for beam (ICB)

One of the key steps in identifying the incoming beam is to determine its charge. The ICB is filled with P10 gas in which energy from the beam is deposited. Knowing the energy deposited in the ICB by the beam, and the relation between the charge of the ion and the energy deposited, it is possible to convert the deposited energy into the charge of the ion using equation 4.6.

$$Z = (A \times Q^2) + (B \times Q) + C \tag{4.6}$$

Where Q is the energy deposited in the detector, and A, B, C are the conversion factors.

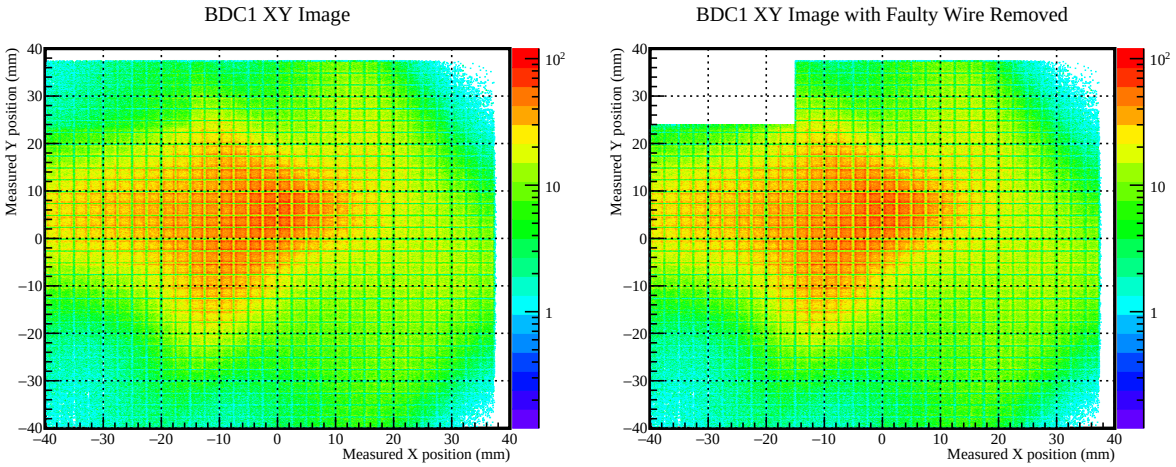

Figure 4.11: The left panel shows the XY beam image in BDC1, which shows the faulty region as a sudden decrease in counts in the upper left corner. The right panel shows the XY beam image in BDC1 with the faulty region removed.

4.2 Beam Drift Chambers

The use of the two drift chambers, BDC1 and BDC2, allows for the reconstruction of the beams path from the entrance of the SAMURAI experiment hall onto the target. The key benefit of this analysis is to predict the position of the beam on the target. This enables the use of a cut, which ensures that the beam is only interacting with the target, and not the target holder. It is also used later for improvements in the reconstructed angle of the gamma ray in DALI2.

4.2.1 BDC1 Faulty Wire Removal

In BDC1, there is an issue with the beam image, with a region showing an unusual pattern. This is the result of an incorrect wrong connection of a wire in BDC1. The faulty region of BDC1 is seen for $X < -15$ mm and $Y > 24$ mm in figure 4.11. As a result, the ions that are in this region do not have their position and angle reconstructed correctly, so when performing the target cut, it may include bad ions that are not truly at the location reported. Furthermore, if these ions were to be included, it is possible that the reconstructed fragment A/Z would be wrongly determined. Therefore it is necessary to remove this faulty region. Due to the location of the faulty region being in a corner of the detector, away from the most intense part of the beam, its removal only reduces the statistics by approximately 2%.

4.2.2 Alignment of Drift Chambers

The trajectory of the incoming ions onto the target is important as it allows for the removal of ions that interact with the target holder, and an improvement in the resolution of DALI2, by improving the angle reconstruction of the gamma ray. In order to perform this analysis, it is important that the drift chambers are correctly aligned with one another. As a result, it is chosen that the position of BDC1 and FDC1 is fixed, and the alignment of the detectors is done by adjusting the position of the ions in BDC2. To perform this calibration, it is necessary to use the empty target runs, as the use of a target may result in a change in trajectory as a result of interactions with the target. In order to determine the adjustment needed to align the drift chambers, the X and Y position of the ion in BDC2 is interpolated by taking the position of the ion in BDC1 and FDC1, and assuming a straight line trajectory between the two positions.

$$\theta_x = arctan\left(\frac{X_{FDC1} - X_{BDC1}}{Z_{FDC1} - Z_{BDC1}}\right) \tag{4.7}$$

$$X_{BDC2} = X_{BDC1} + (Z_{BDC2} - Z_{BDC1})\left(\frac{X_{FDC1} - X_{BDC1}}{Z_{FDC1} - Z_{BDC1}}\right) \tag{4.8}$$

$$\theta_y = arctan\left(\frac{Y_{FDC1} - Y_{BDC1}}{Z_{FDC1} - Z_{BDC1}}\right) \tag{4.9}$$

$$Y_{BDC2} = Y_{BDC1} + (Z_{BDC2} - Z_{BDC1})\left(\frac{Y_{FDC1} - Y_{BDC1}}{Z_{FDC1} - Z_{BDC1}}\right) \tag{4.10}$$

Where $X/Y_{BDC1/FDC1}$ are the X or Y position measured within BDC1 or FDC1. Z_{BDC1} is the Z position of BDC1, located 2077.12 mm before the target; Z_{BDC2} is the Z position of BDC2, located 1077.81 mm before the target; and Z_{FDC1} is the Z position of FDC1, located 983.38 mm after the target. A schematic of the alignment technique is shown in figure 4.12.

In order to determine the offset of BDC2 that is required to align the drift chambers, the measured X/Y position is compared to the interpolated X/Y position. The difference between the two values is the alignment offset. This analysis is shown in figure 4.13 and figure 4.14. The X position of BDC2 was determined to be offset by +0.4762 mm, while the Y position was determined to be offset by -0.475 mm.

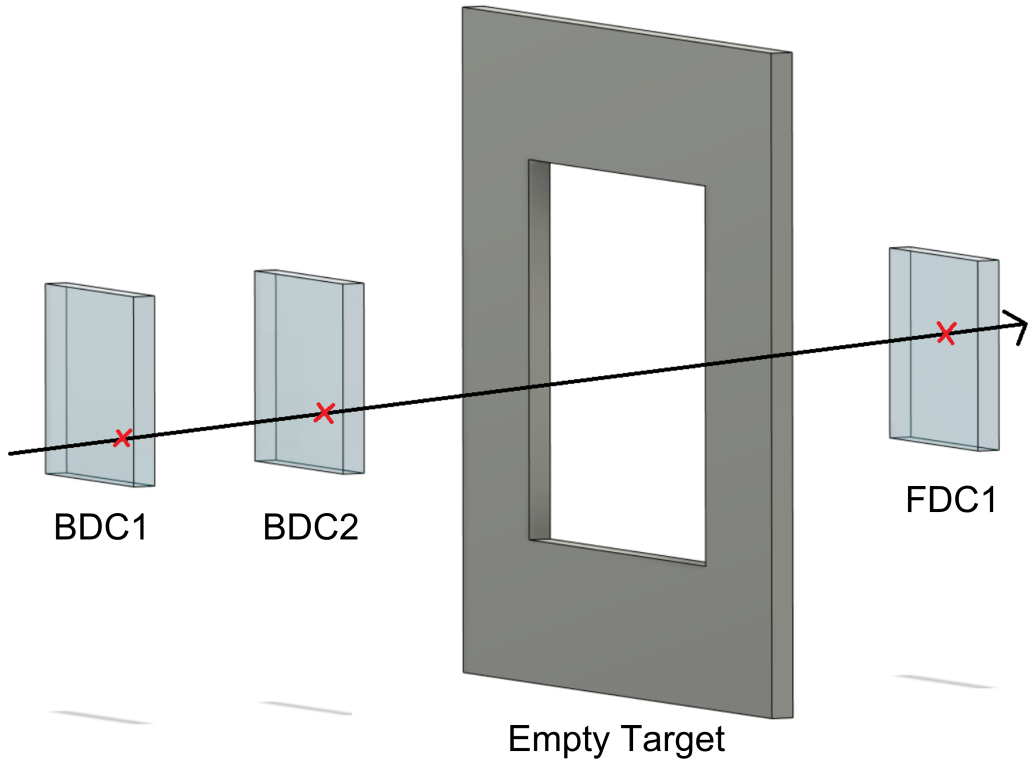

Figure 4.12: The method used to align the drift chambers. The three drift chambers are seen, with BDC2 shown in two positions. The blue line and crosses represent the path of an ion and the hit location in the drift chambers. The red cross represents the measured position in BDC2, with the difference in the red and blue cross in BDC2 being the alignment correction.

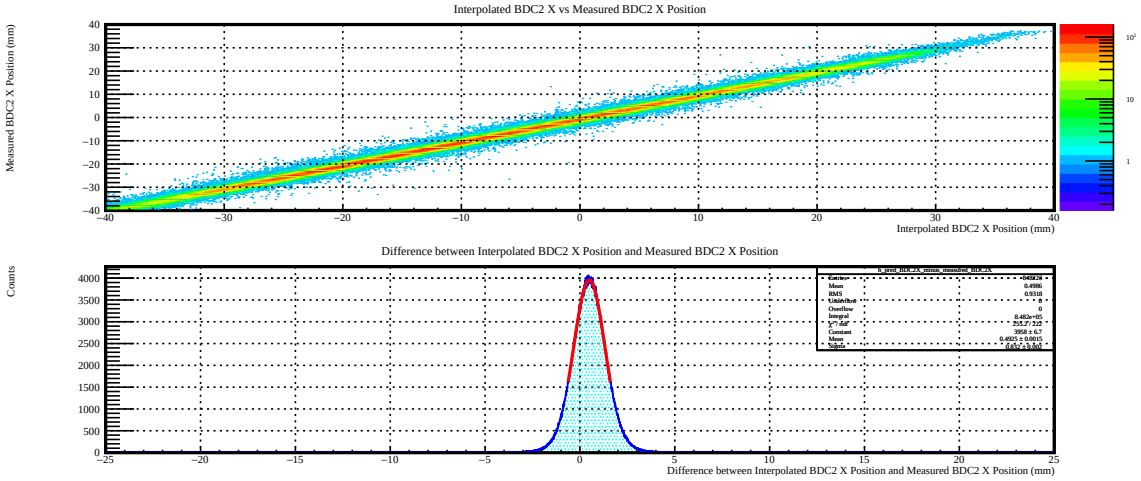

Figure 4.13: The top panel shows the X alignment technique, taking the interpolated X position, and plotting it against the measured X position. The bottom panel shows the difference between the interpolated X position and the measured X position, with a gaussian fitting in order to determine the offset necessary to align the drift chambers.

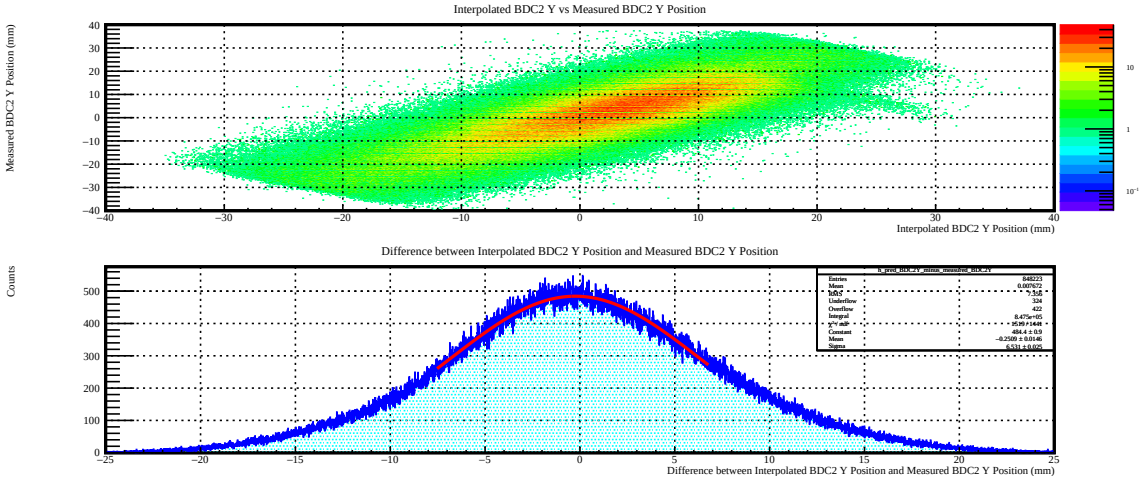

Figure 4.14: The top panel shows the Y alignment technique, taking the interpolated Y position, and plotting it against the measured Y position. The bottom panel shows the difference between the interpolated Y position and the measured Y position, with a gaussian fitting in order to determine the offset necessary to align the drift chambers. The distribution of the Y position is different to the X position due to the Y position in FDC1 being determined using the u,v wires, which result in worse reconstruction when compared to using dedicated Y wires.

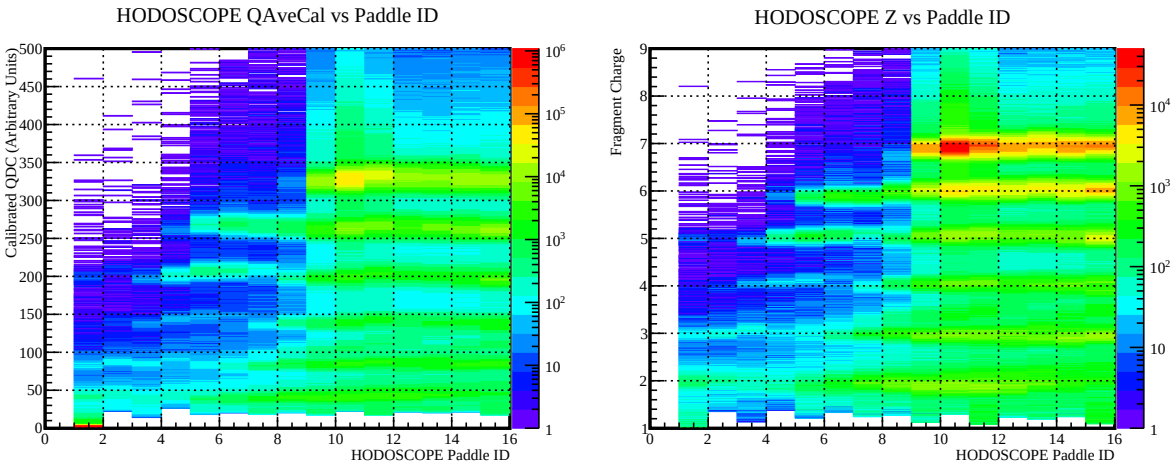

Figure 4.15: The left panel shows the HODOSCOPE paddle ID vs the calibrated deposited energy. As the incoming beam is known, gating on incoming nitrogen means that the maximum charge is known to be Z=7, with this the right panel shows the HODOSCOPE paddle ID vs the charge of the ion determined by converting from QAveCal to charge.

4.3 Fragment Particle Identification

4.3.1 Fragment Z

The calibration of the charge in the HODOSCOPE is similar to the process used in the calibration of the ICB. Knowing the beam composition from the incoming beam analysis, the raw charge is plotted for each paddle gated on incoming ^{21}N. As the maximum charge in the HODOSCOPE is known, each paddle can be converted from raw charge to calibrated charge.

The use of two PMTs, similar to the SBTs, allows for the removal of uncorrelated events which improves the charge and time resolution of the HODOSCOPE. The code takes the raw charge, and finds the average using the square root of the product of the charges. The pedestal is then found, representing a charge of 0, and then the Q_{Cal} is found so that the deposited energy in each paddle is the same. Once the calibrated deposited energy has been determined, there can still be small fluctuations. Therefore, for each paddle, the charge of the ion is determined using equation 4.11, where Q is the calibrated deposited energy, and A and B are two parameters. Following the calibration of the raw charge to atomic number, further improvements can be made such as removing the slew dependency of the HODOSCOPE.

$$Z_{HOD} = A \times Q_{cal}^{B} \tag{4.11}$$

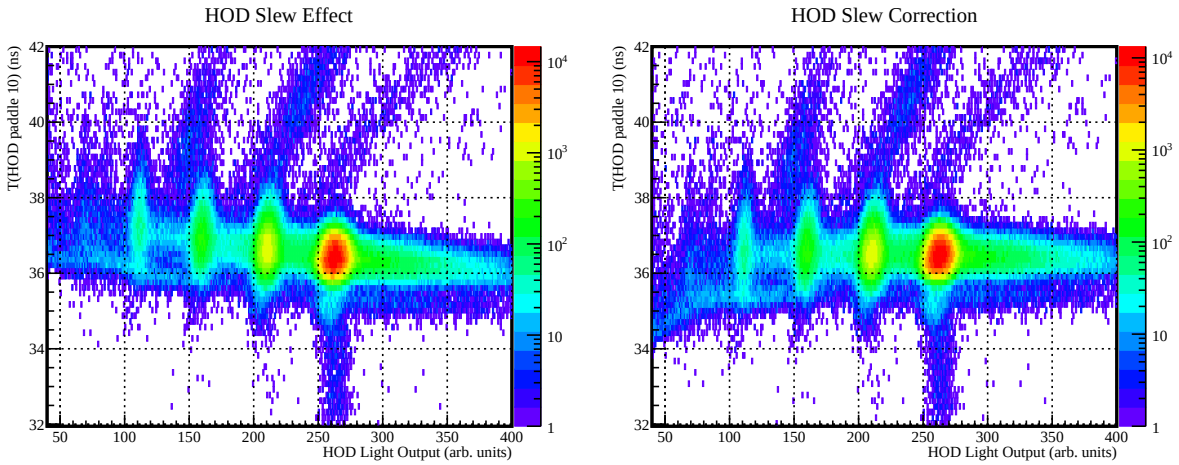

Figure 4.16: The left panel shows an example of the slew effect in paddle 10, the different peaks represent the different elements, with the peak with a light output at approximately 260 being nitrogen. The ions with a higher charge have a lower time compared to the lower charge ions (e.g. Z=4 at a light output of approximately 110). The right panel shows the correction of the slew effect, with different charges arriving at the same time.

4.3.2 HODOSCOPE Slew correction

The HODOSCOPE is constructed in a similar way to the SBTs. It consists of plastic paddles (although thicker) coupled to a PMT at either end. As a result, there will be a slew effect that needs to be corrected. The method is similar to the SBT slew correction, and uses the following equation 4.12.

$$T_{slew(U/D)} = T_{cal(U/D)} - \left(\frac{A}{\sqrt{Q_{raw(U/D)}}} + B \right) \tag{4.12}$$

Where $T_{cal(U/D)}$ is the difference in calibrated time between a paddle in the HODOSCOPE and the average slew and position corrected time in the SBTs for either the top or down detector, A and B are fit parameters determined by fitting the dependency shown in the left panel of figure 4.16, and $Q_{raw(L/R)}$ is the raw charge collected in the detector in question. The slew effect and the effect of the correction is seen in figure 4.16.

4.3.3 Fragment A/Z

The method of analysing the fragment A/Z is similar to the incoming beam A/Z identification, however it now has to deal with the added complexity of the fragments passing through the SAMURAI magnet. Unlike the ICB, careful analysis is required for paddles 1-8. This is because the beam has passed through the SAMURAI magnet which leads to separation of the different isotopes. As a result, isotopes of elements with fewer neutrons, e.g. ^{16}C, have their path deflected more than heavier isotopes, so will go to one side of the HODOSCOPE.

Similarly, heavier isotopes with more neutrons, e.g. ^{20}C, are deflected less. In order to aid the experiment, the amount that the fragment beam is bent is chosen around a central value. In the case of this data, an A/Z of three is focused approximately on the center of the HODOSCOPE. As a result, the magnetic rigidity of the beam needs to be determined using the reconstructed tracks. These reconstructed tracks are determined using the position and angle of the unreacted beam and fragments in FDC1, immediately before the SAMURAI magnet, and FDC2, immediately after the SAMURAI magnet. The magnetic rigidity is then calculated using the transfer matrix method, determined using a central Bρ of 7.3 Tm.

The ray transfer matrix analysis method is a way of determining the magnetic rigidity of an ion using the position and angle information before the SAMURAI magnet, at FDC1, and after the SAMURAI magnet, at FDC2. The method was developed in order to describe the position of a ray after passing through an interface, most commonly light passing through a lens, however it can similarly be applied for ion optics, where an ion passes through a magnetic field [67]. With the position and angle of the ion known both before and after the SAMURAI magnet, it is possible to determine the ray transfer matrix method. The position after passing through the SAMURAI magnet can be described using equation 4.13.

$$\begin{bmatrix} X_2 \\ \theta_2 \end{bmatrix} = \begin{bmatrix} A & B \\ C & D \end{bmatrix} \cdot \begin{bmatrix} X_1 \\ \theta_1 \end{bmatrix} \tag{4.13}$$

The approximation relies on the paraxial approximation, otherwise known as the small angle approximation, where $sin(\theta) = \theta$. With this, the first step in determining the magnetic rigidity can be performed using equation 4.14.

$$\begin{bmatrix} rvec_{10} \\ rvec_{20} \end{bmatrix} = \begin{bmatrix} Mat2_{10} & Mat2_{11} \\ Mat2_{20} & Mat2_{21} \end{bmatrix}^{-1} \cdot \left(\begin{bmatrix} X_2 \\ \theta_2 \end{bmatrix} - \left(X_1 \cdot \begin{bmatrix} Mat1_{10} & Mat1_{11} \\ Mat1_{20} & Mat1_{21} \end{bmatrix} \right) \right) \tag{4.14}$$

From this, the value of delta (δ), which represents x/d (position of beam in detector, divided by momentum dispersion) shown in equation 4.5 can be extracted using equation 4.15.

$$\delta = rvec_{10} \tag{4.15}$$

The magnetic rigidity of the fragment can then be determined in a similar way to the method for the incoming magnetic rigidity, see equation 4.16.

$$B\rho_{fragment} = B\rho_{centre} \left(1 + \left(\frac{\delta}{100} \right) \right) \tag{4.16}$$

Ray tracing is then used in order to trace the path taken from the target to the HO-

DOSCOPE. In order to trace the ion from the target to the HODOSCOPE, the RK4 Runge-Kutta method is used. The Runge-Kutta method is used to approximate the $n^{th}+1$ position. This is done between the hit location at FDC1 and FDC2 over 100 steps between the two positions. The generic formulation for the RK4 Runge-Kutta method solves a problem where the initial values is given by equation 4.17.

$$\begin{aligned} \frac{dy}{dt} &= f(t,y) \\ y(t_0) &= y_0 \end{aligned} \tag{4.17}$$

The Runge-Kutta method approximates the $n^{th}+1$ position using equation 4.18 [68].

$$\begin{aligned} y_{n+1} &= y_n + \frac{1}{6}h\left(k_1 + 2k_2 + 2k_3 + k_4\right), \\ t_{n+1} &= t_n + h \\ &where: \\ k_1 &= f(t_n, y_n), \\ k_2 &= f\left(t_n + \frac{h}{2}, y_n + h\frac{k_1}{2}\right), \\ k_3 &= f\left(t_n + \frac{h}{2}, y_n + h\frac{k_2}{2}\right), \\ k_4 &= f(t_n + h, y_n + hk_3) \end{aligned} \tag{4.18}$$

Using equation 4.18, and iterating over 100 steps, the approximate location of the ion is determined. Using these 100 predicted locations, the path length between FDC1 and FDC2 can be found. The total distance is then calculated by taking the distance between the target and FDC1, the distance using the 100 iterations of the Runge-Kutta method, and the distance between FDC2 and the HODOSCOPE. This path length, along with the time of flight is used to determine the velocity of the fragments. To calculate the time of flight of the fragments, the time of the incoming beam at the SBTs (F13) and the time of the fragment in the HODOSCOPE needs to be known. The time of flight is calculated using the slew and position corrected time from the SBTs and the slew corrected time in the HODOSCOPE. Knowing this information, the fragment A/Z can be reconstructed using the following equation 4.19.

$$\frac{A}{Z} = \frac{B\rho \times c}{m_n \times \beta \times \gamma} \tag{4.19}$$

In equation 4.19, A/Z is the mass divided by the charge; $B\rho$ is the magnetic rigidity of the fragment; c is the speed of light; m_n is the mass of a nucleon; β is the velocity of the fragment and γ is the Lorentz factor.

The result of this can be combined with the fragment Z in order to produce the reaction

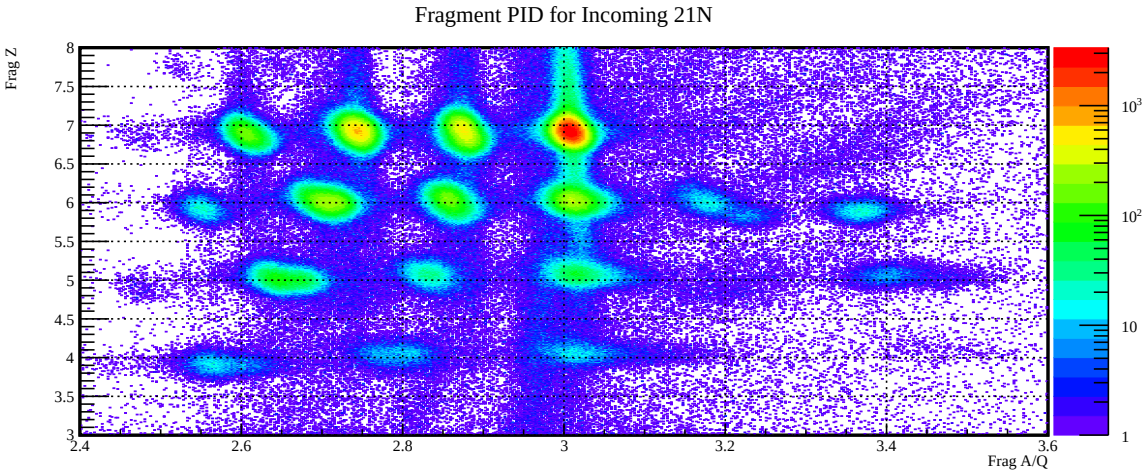

Figure 4.17: The fragment particle identification, for data set two, gated on incoming ^{21}N, and removing other known problems such as the faulty BDC1 wire.

fragment particle identification plot. This is shown in figure 4.17. The resolution of the fragment Z and A/Z was determined for this method using the fragment particle identification gated on incoming ^{21}N. The A/Z resolution was determined by selecting on outgoing carbon fragments (as this work looks at ^{20}C), and fitting each peak with a gaussian. The resolution was then determined by taking the full width half maximum values for each isotope along the carbon isotopic chain, and weighting it according to the number of counts in the peak. For the A/Z, the weighted FWHM was determined to be 0.0432. This was repeated to determine the resolution for the charge, but in this case, isotopes with an A/Z=3 were gated on. The weighted FWHM for the charge resolution was determined to be 0.230.

4.3.4 HODOSCOPE Position Reconstruction using M=2 Events

Considering the higher multiplicity in the HODOSCOPE has multiple benefits. By looking at higher multiplicity events, it is possible to determine the exact position of the HODOSCOPE in relation to FDC2. It is also possible to increase the statistics by reconstructing events that are in adjacent paddles.

In order to determine the position of the HODOSCOPE in relation to FDC2, it is necessary to use the projected position of the beam onto the HODOSCOPE from FDC2. The paddles of the HODOSCOPE are 10 cm wide, therefore due to this large width, most ions that interact with the HODOSCOPE have a multiplicity of one. This is because they impact with a relatively small angle onto the paddles, and therefore only interact with a single paddle. However towards the edge of the paddles, it is possible that an ion will enter the edge of one paddle and exit through the edge of an adjacent paddle. It is therefore possible to determine the exact location of the HODOSCOPE paddles by plotting the projected position gating on

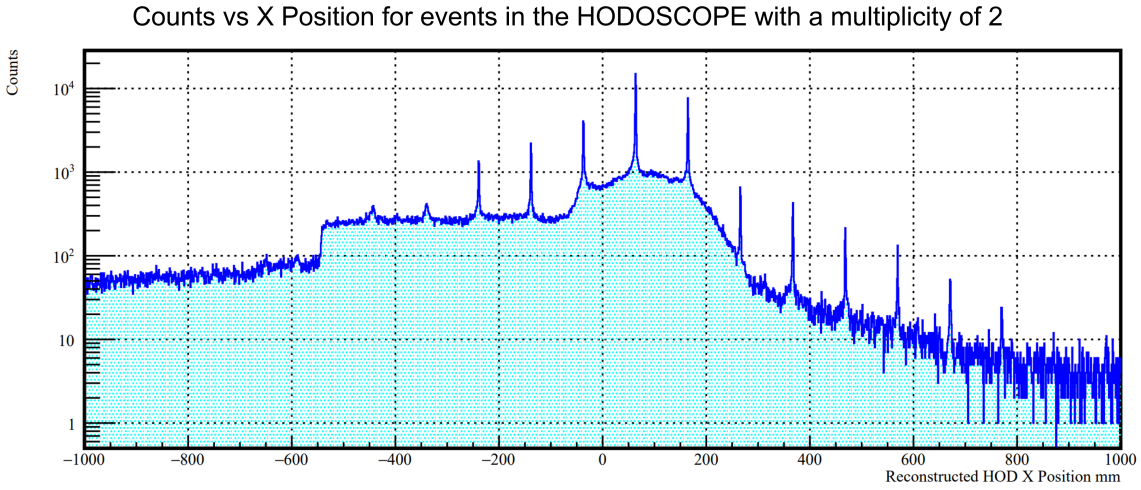

Figure 4.18: Figure of the projected X position in the HODOSCOPE gated on M=2 events, the sharp peaks show the location where adjacent paddles meet.

events with a multiplicity greater than or equal to two. When this is done, it should be seen that there will be an increase in events at the edge of the paddles.

In figure 4.18, several different features can be seen that provide information on the position of the HODOSCOPE. At approximately -550 mm, there is a sharp increase in the number of counts. This marks the edge of the HODOSCOPE, representing paddle sixteen, on the lighter A/Z region. It is then possible to see thirteen sharp peaks, which represent the edge of the paddles. As the reconstructed position gets higher, which represents ions with a higher A/Z, the statistics get lower, and as a result it is not possible to see the edge of the HODOSCOPE or the last couple of paddles. However, using the edge of the HODOSCOPE and the thirteen peaks, it is possible to determine the position of the HODOSCOPE and its paddles in relation to FDC2. The offset is found to be -264.41 mm. This value is important later for calculating the transmission of the beam from the target to the HODOSCOPE.

4.3.5 Reconstruction of M=2 Events

It is possible to increase the statistics by reconstructing the events that interact with two paddles. It is first necessary to determine the amount of statistics for different multiplicities. This was done by running one million events, and plotting the number of HODOSCOPE entries for each incoming event.

As can be seen in figure 4.19, the majority of events have a multiplicity of either zero or one. The HODOSCOPE events with a multiplicity of zero represent incoming ions where no signal is seen in the HODOSCOPE. As a result, an event is assigned to paddle one, with an energy signal equivalent to the pedestal and no time information. This constitutes approx-

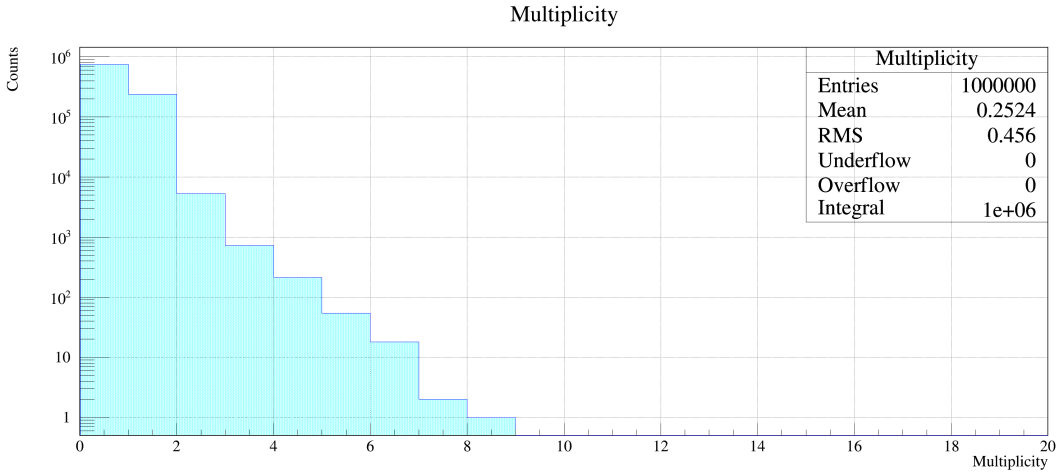

Figure 4.19: HODOSCOPE Multiplicity for one million events.

imately 75% of the incoming events. Most of the remaining events have a single hit in the HODOSCOPE, with a small amount with a multiplicity greater than one. Events with a multiplicity greater than one represent 2.63% of the number of events with a multiplicity of one.

HODOSCOPE Multiplicity									
Multiplicity	**0**	**1**	**2**	**3**	**4**	**5**	**6**	**7**	**8**
Counts	755,200	238,500	5263	726	214	54	18	2	1
Percentage of M=1 (%)	-	100	2.21	0.3	0.09	0.02	0.01	0.00	0.00
Percentage of M=1 for M>1: 2.63%									

Table 4.6: The multiplicity of events in the HODOSCOPE.

When reconstructing the events that interact with two paddles, it is necessary to sort through all the events with a multiplicity of greater than or equal to two, and then sort through all the events and check if the events have signals for both energy and time in both the up and down detectors (a good hit). If the HODOSCOPE event has a good hit, it is then checked to find any events with an id ± 1 from the good hit. Previously, the energy deposited in the HODOSCOPE (QAveCal) was calibrated so that the charge deposited in each paddle is the same. This means that it is possible to convert from the energy deposited into charge using two conversion parameters. In order to reconstruct the charge of an ion which interacts with two adjacent paddles, the energy deposited in both paddles can be added together and then converted into charge. Adding together the paddles, it is possible to produce a particle identification plot. In order to determine the Bρ, the positions used are the locations in the FDCs and the paddle with the highest energy deposition. The time in the HODOSCOPE is calculated by taking the average of the times in the two adjacent paddles. Using this infor-

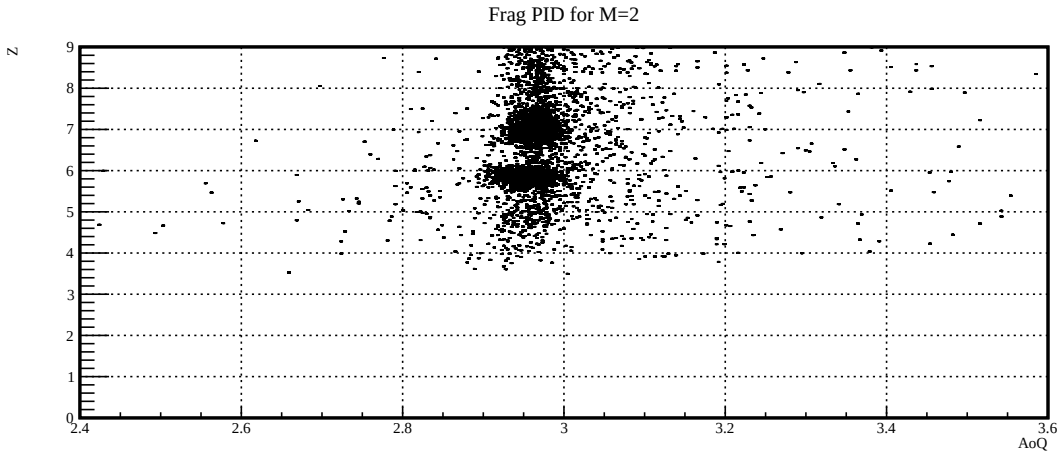

Figure 4.20: Fragment particle identification for M=2 Entries in the HODOSCOPE.

mation the particle identification is then produced in the normal way.

As can be seen in figure 4.20, the most common reconstruction is for an A/Z of approximately three, and for Z = 7 and 6, representing ^{21}N and ^{18}C. However, as the reconstruction is very poor in A/Z and the statistics are very low in comparison to the reconstructed particle identification with a HODOSCOPE multiplicity of one, representing less than 1% of the M=1 particle identification statistics, the extra events were treated as a systematic uncertainty.

4.4 DALI2 γ-ray Analysis

4.4.1 Calibration

In order to calibrate the DALI2 detector, a series of different calibration sources were used. The sources used were: ^{22}Na, ^{60}Co, ^{88}Y and ^{137}Cs, which were placed at the target position within DALI2. These sources were chosen as they provide a wide range of gamma rays, from 511 keV to 1836 keV. In order to calibrate DALI2, the raw ADC for each calibration source is plotted for each detector. Using this, an exponential background and a gaussian fit are applied. The peak of the ADC is then plotted against the reference energy for the source. Using the different sources, the values used to convert between ADC and energy are determined by starting with some test parameters, determining the residual between the energy (using the test parameters) and the reference energy, squaring the residuals and then taking the sum of the squares. The conversion parameters are then determined by varying the two test parameters until the sum of the square of the residuals is minimised. This needs to be done for each of the 140 detectors as each photomultiplier tube attached to each crystal has slightly different properties with regards to its charge collection. This can be due to the different size of the crystals used (three different sizes), how well the PMTs are coupled to the crystal and

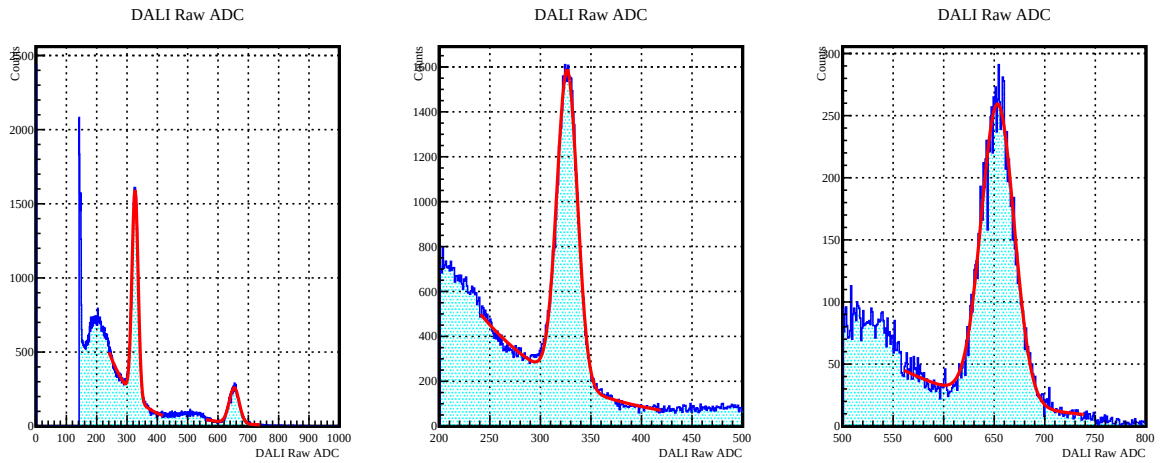

Figure 4.21: An example of the fitting method used to calibrate the individual detectors in DALI2, using a ^{22}Na source. The result of which is shown for both peaks in the left panel, while the middle and right panel shows the fitting zoomed in on each of the two peaks.

variation in the quality of the crystal and components within the PMT. An example of the fitting is seen in figure 4.21. The result of the calibration for a ^{22}Na source is seen in figure 4.22.

4.4.2 Doppler correction

Whilst the calibration shown in figure 4.22 is appropriate for gamma rays coming from a stationary source, under experimental conditions the incoming beam has a velocity of approximately $\beta = 0.6$. Because of this, it is necessary to perform a Doppler correction of the gamma rays [58]. In order to perform the Doppler correction, it is necessary to know the angle of the gamma ray. This is determined from the detector ID, where the geometry of DALI2 is known. The Doppler correction is given by equation 4.20.

$$E_\gamma = E_{lab} \times \left(\frac{1 - \beta \times cos(\theta)}{\sqrt{1-\beta^2}} \right) \tag{4.20}$$

Where E_γ is the Doppler corrected energy, E_{lab} is the energy in the lab reference frame, β is the velocity of the incoming particle, and θ is the angle of the gamma ray. There will be uncertainty introduced to the measurement from the angle of the gamma ray. This is because there is uncertainty from the location of the source of the gamma ray within the target, and the location of the gamma rays interaction within the crystal.

In the original reconstruction of the θ, it is assumed that the gamma ray is emitted from the centre of the target at location (0,0,0). The reconstructed angle is then determined using the X,Y,Z information for the detector. This is done in spherical co-ordinates, with θ being determined using equation 4.21.

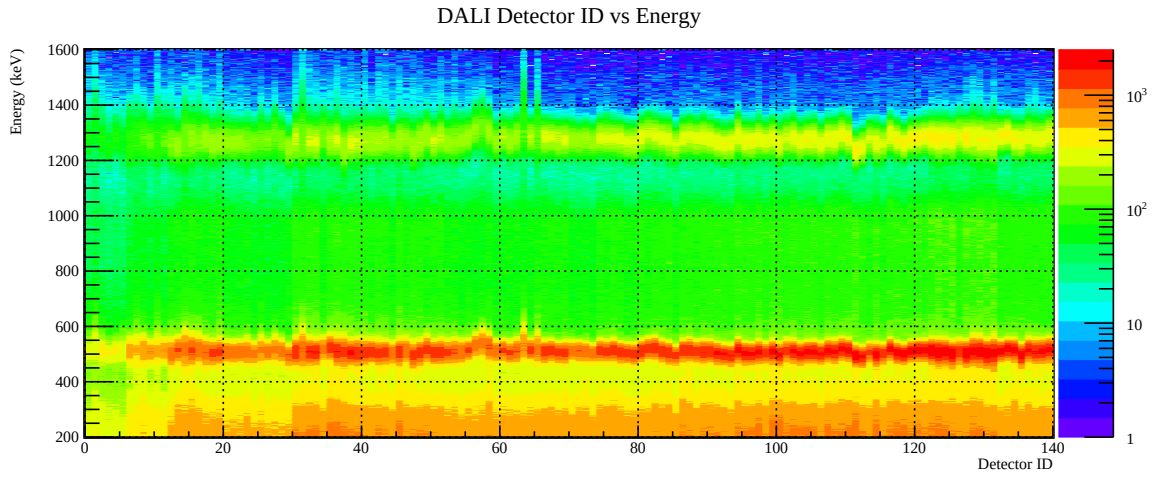

Figure 4.22: An example of DALI2 detector ID vs calibrated energy using a ^{22}Na source, showing the alignment of the different detectors.

$$\theta = \frac{Z_{Detector}}{\sqrt{X^2_{Detector} + Y^2_{Detector} + Z^2_{Detector}}} \tag{4.21}$$

In order to improve the resolution of the reconstructed Doppler corrected energy, it is possible to take into account the position of the incoming ion onto the target. In principle, it is better to use the fragment position leaving the target because the interaction with the target may change the fragments angle. However, there is only one tracking detector after the target, and before SAMURAI, FDC1. FDC1, whilst being thicker than the BDCs, is still not particularly thick, so the reconstructed angle has a larger uncertainty than the incoming angle. The tracking of the incoming ions onto the target is done using the two BDCs. Whilst the BDCs are thinner than FDC1, and therefore the angle reconstruction in an individual detector is expected to be worse than FDC1, the angle can be determined using the difference in position of the ion within the two BDCs. The position of the ion is given using equations 4.22 and 4.23.

$$X_{tgt} = \frac{BDC2_X - BDC1_X}{dist_{BDCs} \times dist_{BDC1-target}} + BDC1_X \tag{4.22}$$

$$Y_{tgt} = \frac{BDC2_Y - BDC1_Y}{dist_{BDCs} \times dist_{BDC1-target}} + BDC1_Y \tag{4.23}$$

In equations 4.22 and 4.23, $dist_{BDCs}$ is the distance between BDC1 and BDC2, which is 999.32 mm and $dist_{BDC1-target}$ is the distance between BDC1 and the target, which is 2077.12 mm.

It is not possible to know the exact Z location where the ^{20}C decays. This is because on average, ^{20}C is produced in the centre of the target, however it can be produced at any

point within the target. As the half-life of the excited state is 6.8 ps, and the fragments have a velocity of approximately $0.62c$, the ^{20}C will travel approximately 1.25 mm per half-life. Therefore, if ^{20}C is produced in the centre of the target, it is expected that approximately 93% will decay within the remaining 5 mm of target. Therefore the Z position is assumed to be at 0, the centre of the target. As a result, in order to determine the theta, the position of the incoming ion on the target is used, $\left(Target_X, Target_Y, 0\right)$.

A further improvement to the angle is to use the angle of the outgoing fragment. Ordinarily, it was assumed that the outgoing fragment follows parallel with the Z axis, however as the BDCs have been aligned with FDC1, the outgoing angle can be determined by taking the difference between the target position and the FDC1 position. The new theta is determined using equation 4.24.

$$\theta_{New} = cos^{-1}\left(\frac{A \cdot B}{|A| \times |B|}\right)$$
$$= cos^{-1}\left(\frac{\left(\left(X_{det} - X_{tgt}\right) \times X_{FDC1}\right) + \left(\left(Y_{det} - Y_{tgt}\right) \times Y_{FDC1}\right) + \left(Z_{det} \times Z_{FDC1}\right)}{\sqrt{\left(X_{det} - X_{tgt}\right)^2 + \left(Y_{det} - Y_{tgt}\right)^2 + \left(Z_{det}\right)^2} \times \sqrt{\left(X_{FDC1}\right)^2 + \left(Y_{FDC1}\right)^2 + \left(Z_{FDC1}\right)^2}}\right) \tag{4.24}$$

Where A represents the distance between the detector position and the target position, determined using the BDCs, and B represents the distance between the target position and the FDC1 position.

The difference between the original method, and the new method is shown in figure 4.23.

4.4.3 DALI2 Simulation

The efficiency of DALI2 is not 100%, therefore when calculating the cross section of the bound 2^+ state in ^{20}C (and unbound states if there is a γ-ray in association with the fragment and neutron), the efficiency of the DALI2 setup must be taken into account. The efficiency of DALI2 also varies with the energy of the gamma ray. In order to determine the efficiency of the DALI2 setup, a GEANT4 code was used to simulate the response of DALI2. This is then compared to calibration files for ^{22}Na and ^{88}Y sources. The code used to simulate DALI2 was produced by Pieter Doornenbal [69].

The EventGenerator Stage

The GEANT4 simulation is comprised of three stages. The first stage is the EventGenerator. In the EventGenerator, the number of decays for a source or the number of decays for a set quantity of incoming ions in a beam is simulated. Then the level scheme for the decay is used to determine the population of each state and the number of decays from each state.

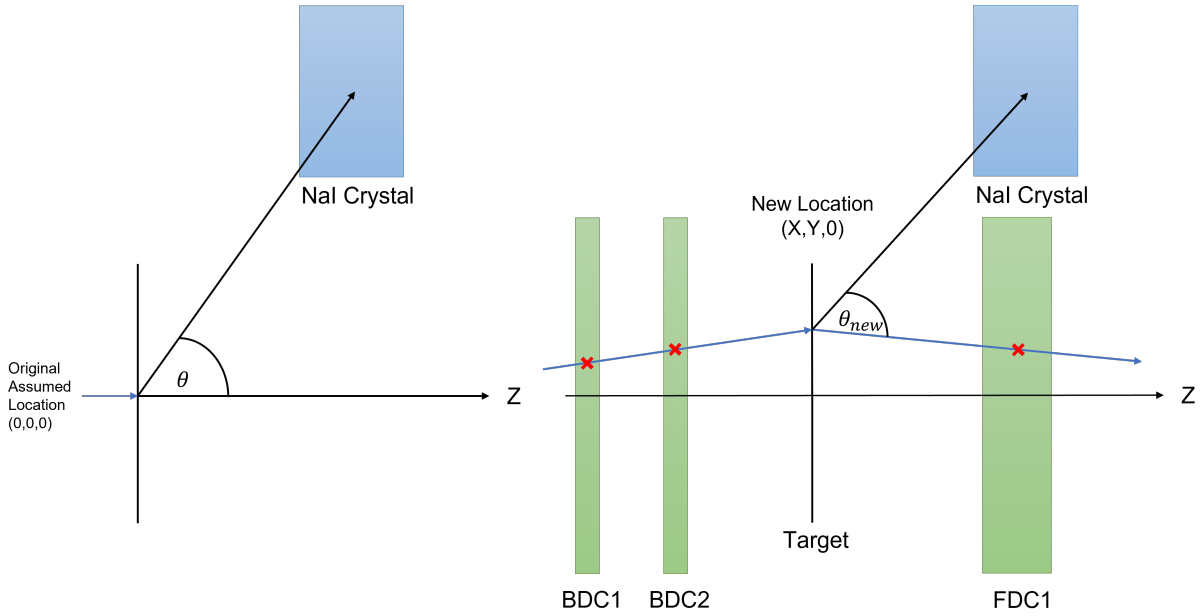

Figure 4.23: The left panel shows the original theta reconstruction, with the angle being determined between the centre of the target and the detector position. The right panel shows the new theta, with the angle being determined using equation 4.24.

In order to simulate the sources to calculate the efficiency, it was necessary to measure the intensity of the source at the time of the experiment, and the live time of the run. In order to determine the activity of the source at the time of the measurement, it was necessary to know the initial activity of the source, the half-life of the source and the date the measurement was taken. The activity of the source and the reference date for the measurement of the source activity was found on the SUNFLOWER collaboration website at [70]. The level scheme for the different sources was taken from the NNDC database [71]. Using that information, the number of half lives that have passed was calculated. Then the activity of the source at the time of the measurement was found using equation 4.25.

$$A_m = A_i \left(0.5^{No_{H.L}}\right) \tag{4.25}$$

Where A_m is the activity at the time of the measurement in becquerels (Bq), A_i is the initial activity of the source in becquerels, and $No_{H.L}$ is the number of half lives. Following this, the length of the run needs to be determined, by taking the length of the run in seconds and then multiplying that by the live time. The live time is calculated using the ratio of the gated and ungated trigger. At this point it is also necessary to account for any downscaling. With this information, and taking the level scheme from the NNDC database [71], the number of decays for each transition can be calculated. These theoretical numbers of decays for each transition will then be used to verify that the simulation is working correctly.

The EventBuilder Stage

The second stage of the GEANT4 simulation is the EventBuilder. This stage takes the root file from the EventGenerator stage, and simulates the response of DALI2. In order to simulate the efficiency of DALI2, the DALI2 setup in its Day-One campaign configuration needs to be recreated within GEANT4. This is 140 NaI(Tl) crystals surrounding the beam pipe structure. Within the beam pipe is the source and the target holder. The beam pipe is surrounded by 1 mm of lead shielding [54] in order to reduce x-rays that are produced. In order to simulate the response of DALI2, the resolution of DALI2 must be determined. This is done by measuring the energy of the peak, and the full width half maximum (FWHM) of the peak. In order to do this, the energy calibration sources ^{88}Y, ^{137}Cs and ^{22}Na were used so that the resolution of a wide range of energies can be determined. In the case of the 511 keV peak in ^{22}Na, the energy and resolution were not included in the resolution calculation. This is because the two 511 keV gamma rays are not necessarily produced in the target position. This means that that the resolution may be different for different detectors, therefore it was excluded from the resolution calculations. Following this, for each detector, the energy vs FWHM was plotted. This was then fitted with the form in equation 4.26. This method has been discussed previously in section 4.4.1.

$$Y = A \times \left(x^{B}\right) \tag{4.26}$$

The free A and B parameters determined by the fitting were then used in the simulation to produce a more realistic response. In order to better recreate the DALI2 response, it was also necessary to consider background radiation. This was done by simulating 10 million decays of ^{40}K, which is responsible for the 1460 keV gamma ray, ^{208}Tl, which is responsible for the 2614 keV gamma ray and ^{214}Bi, responsible for the 1764 keV gamma ray.

The Reconstructor Stage

The final stage is the Reconstructor. This stage takes the output file from the EventBuilder, and performs the analysis of the simulated data. This includes the energy range that is analysed, the Doppler correction of the gamma rays (which is not necessary for calibration source data) and addback. It also allows an energy threshold, which can be used to define a cut off to better match the response of DALI2. This stage of the simulation takes the previous stages, and turns the response into a format that is easily readable, and similar to the output from the data analysis so that the data can be compared to simulation.

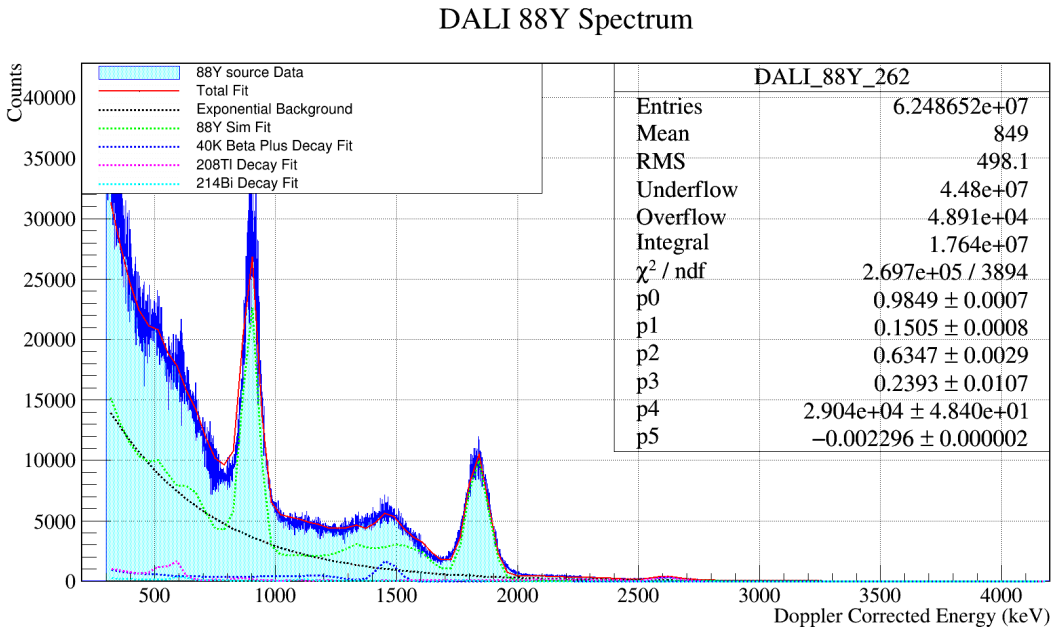

Figure 4.24: The fitting of ^{88}Y source, placed at the target position within DALI2 using a GEANT4 simulated response.

4.4.4 DALI2 Simulation verification

The simulation of DALI2 was verified by comparing the analysis in the Reconstructor stage to the real data analysis from the efficiency calibration run. This was done for ^{88}Y, using run calib0262, and ^{22}Na, using run calib0257. In both cases a minimum energy threshold was set at 300 keV for both the real data and simulation. This was applied due to a reduction in the number of counts at energies below this level. The efficiency data was fitted using the simulation of the run with a scaling factor. The fit used also includes the three background gamma sources, ^{40}K, ^{208}Tl and ^{214}Bi, and an exponential background. In order to validate the simulation with the real data, the scaling factor for the simulated source should be one. This would represent every physical decay is reproduced by the GEANT4 simulation, and that the simulation is correctly taking into account the efficiency and resolution of DALI2. An example of the fitting for the energy of ^{88}Y is seen in figure 4.24.

As can be seen in figure 4.24, the p0 value, which represents the scaling factor of the ^{88}Y GEANT4 simulation is 0.9849 ± 0.0007. This is approximately one, and within the uncertainty of the source activity. Therefore the simulation can be verified in the case of energy. The other scaling parameters (p1-p5), represent the scaling of the background sources (p1-p3) and the fit parameters from the exponential background (p4,p5).

The difference between the fitting parameter and the theoretical value of 1, is treated as a systematic uncertainty when determining the exclusive cross section of the 2^+ state in ^{20}C.

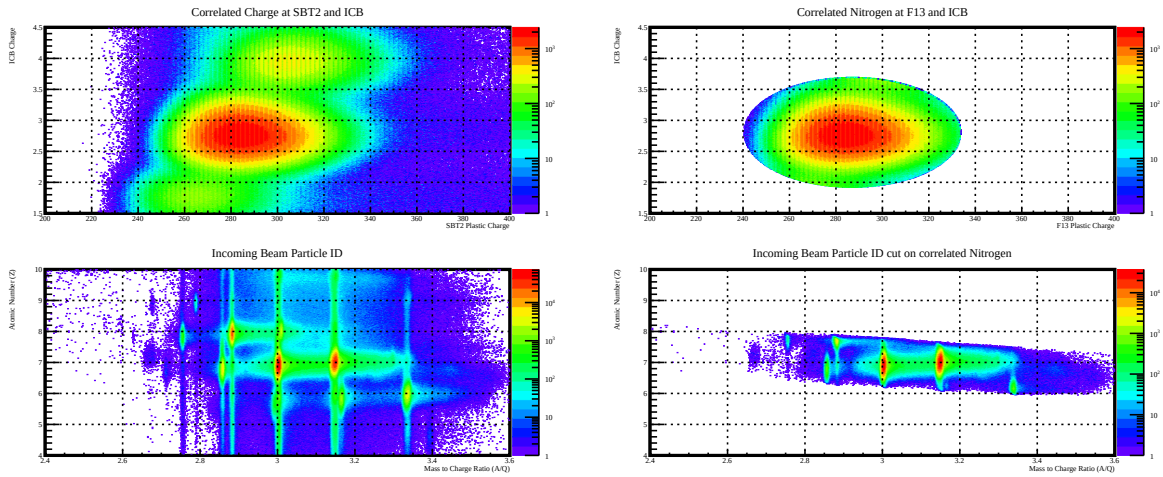

Figure 4.25: A figure with the top row showing the correlated charge, and its cut, and the bottom row showing the incoming beam particle identification, and the effect the correlated nitrogen cut has on the incoming beam particle identification.

4.5 Analysis Cuts

In order to clean up the incoming and outgoing particle identification plots, used to determine the inclusive and exclusive cross sections, various cuts are used which are described in the following sections.

4.5.1 Correlated nitrogen

A cut that is used to determine the amount of incoming ^{21}N is to check that the charge in the plastics at SBT2 (F13) and the ICB is correlated. This is done by applying a 2D gaussian fit, and then taking a three sigma width. This has the aim of ensuring the incoming beam is nitrogen. The cut can be seen in figure 4.25.

The top left panel in figure 4.25 shows the correlated charge in SBT2 and the ICB, the three correlated regions represent the energy deposited from carbon, nitrogen and oxygen, with the lowest correlated charge region representing carbon, and the central region representing nitrogen, on top of this is the fitting of the correlated charge. The top right panel shows the three sigma 2D gaussian cut on the correlated charge. The bottom left panel shows the incoming beam particle identification with no cuts, while the bottom right panel shows the incoming beam particle identification, cut on correlated nitrogen.

The use of the cut results in the inclusion of small amounts of oxygen/carbon which have deposited less/more energy within the detectors. In the case of carbon, this can be seen at A/Z = 3.34 and Z = 6.3 which is incoming ^{20}C, while in the case of oxygen, it can be seen at A/Z = 2.87 and Z = 7.8, which is ^{23}O.

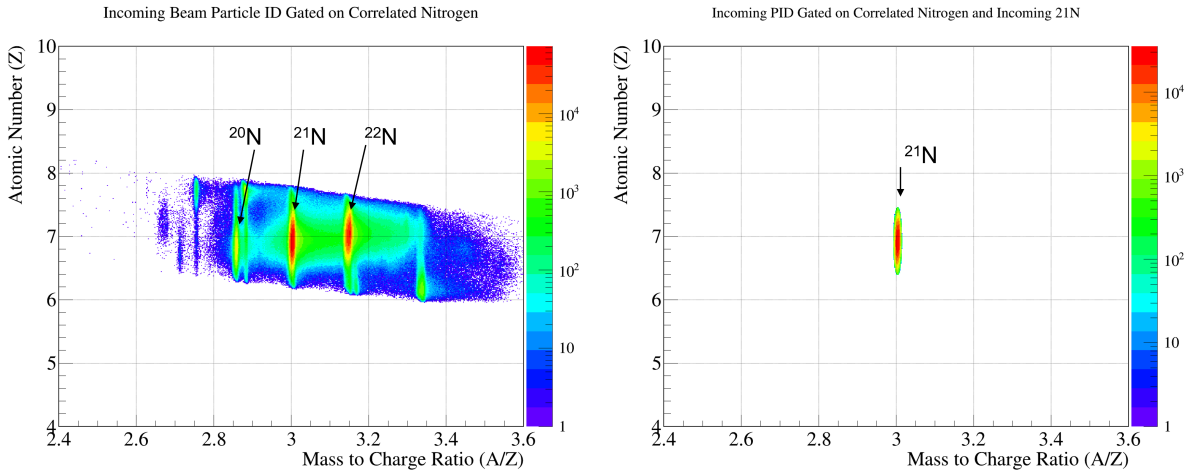

Figure 4.26: A comparison of the incoming particle identification gated on correlated nitrogen and the incoming particle identification gated on ^{21}N.

4.5.2 Incoming Particle Identification ^{21}N cut

For the purpose of this investigation it is necessary to gate on ^{21}N from the incoming particle identification. The first step of gating on incoming ^{21}N is to gate on correlated nitrogen. This is shown in the left panel of figure 4.26, which shows there is a significant background of counts (shown in green) between the peaks of the different nitrogen ions. On the lower A/Z region, there is little overlap of the background between ^{20}N and ^{21}N. Similarly, there is little overlap of the background between Z=6, Z=7 and Z=8. On the other hand, there is a large overlap of the background between ^{21}N and ^{22}N.

As a result, to determine the number of incoming ^{21}N, the incoming particle identification was plotted for correlated nitrogen. This was then fitted using a 2D gaussian. This was first done with the all incoming data (no trigger cuts) in order to determine the centre and sigma of the 2D gaussian. The three sigma range is then determined about the centre of the fit. Following this, the incoming downscaled beam is then plotted using the same cut, and the amount of ^{21}N is determined by the number of entries in the histogram. As the three sigma range accounts for 99.7% of the theoretical full quantity of ^{21}N, the missing 0.3% of statistics are treated as a systematic uncertainty.

4.5.3 Analysis of separate incoming ^{21}N loci

When performing the analysis, it was determined early on that there were two loci for the incoming ^{21}N. This can be seen in figure 4.27, with one centre being located at approximately X = 0 mm with a smaller secondary peak at approximately X = -25 mm.

It is much clearer to see the two structures by plotting the correlation for the X position in BDC1 and BDC2. This is seen in the left panel of figure 4.28, where it is clear that two different

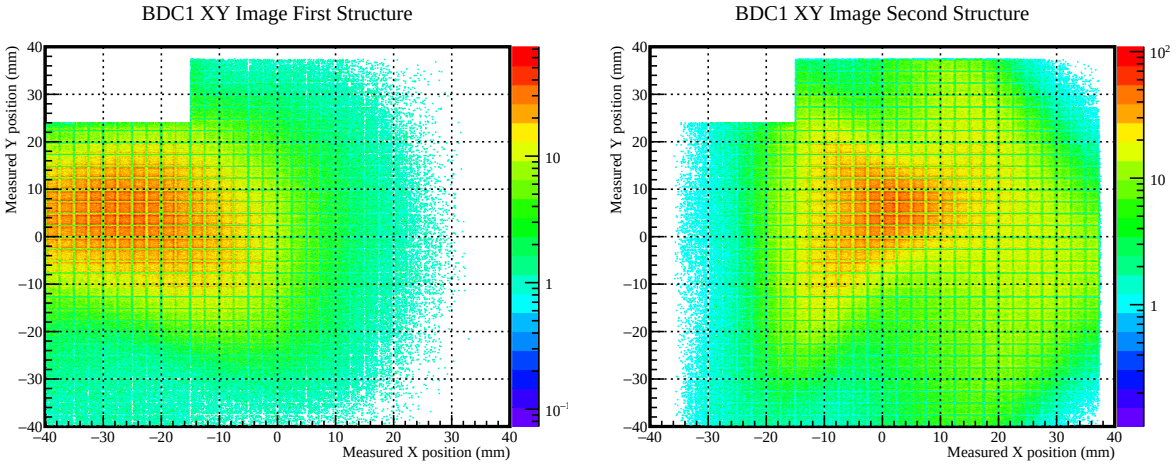

Figure 4.27: A comparison of the XY beam image for incoming ^{21}N within BDC1. It can be cleanly seen that there are two different structures, that are centred at different positions in the X axis. Note the missing region is the cut applied to remove the faulty region of BDC1.

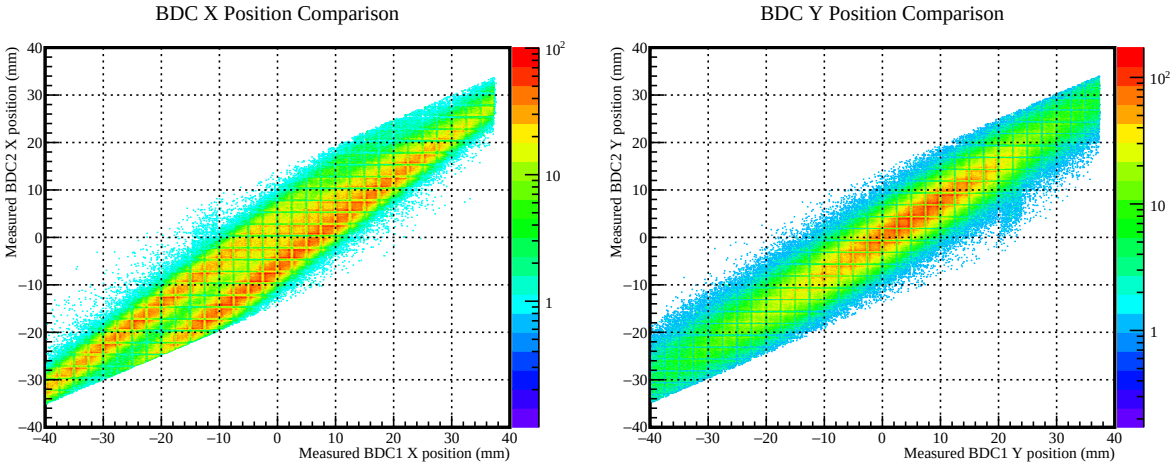

Figure 4.28: The left panel shows a comparison of the X position in BDC1 and BDC2 for incoming ^{21}N. It can be clearly seen that there are two significant peaks. The right panel shows a comparison of the Y position in BDC1 and BDC2, there is only one structure visible.

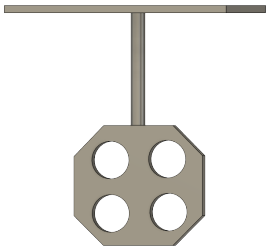

Figure 4.29: A drawing of the target holder used in the Day-One campaign which held the empty, carbon and lead targets.

structures are present. As the incoming ^{21}N has two components, it is necessary to analyse the transmission of them separately, as the position and angle of the structures may result in better or worse transmission due to interaction with different materials. Furthermore, the velocity of the beam differs when comparing the two structures, therefore they should be treated differently as this can change the cross section. The right panel of figure 4.28 shows the correlation of the Y position in BDC1 and BDC2. This does not show any clear double structure, and this is backed up by figure 4.27, which shows the Y position is centred around Y = 5 mm for both structures.

The two structures were found to be stable through the experiment, not changing in the position. Therefore a cut was applied for each structure and the date was analysed, with the cross section determined using the weighted average of the individual cross sections.

4.5.4 Target cut

The beam image recorded at BDC1 and BDC2 was projected to predict how the beam impinges on the target. The target holder is suspended from the flange, and contains four holes which hold the different targets used in the experiment. The targets used in the experiment have a radius of 40 mm. The transmission, which is discussed later in section 4.6, shows that the transmission starts to decrease at target radii greater than 30 mm, therefore a target cut with a radius of 30 mm was chosen.

4.5.5 Fragment Particle Identification ^{20}C cut

In order to determine the amount of reacted ^{20}C, the same method used to determine the amount of incoming ^{21}N was used. This was done gating on correlated nitrogen, incoming ^{21}N, removing the faulty region in BDC1, applying the target cut, and gating on a structure.

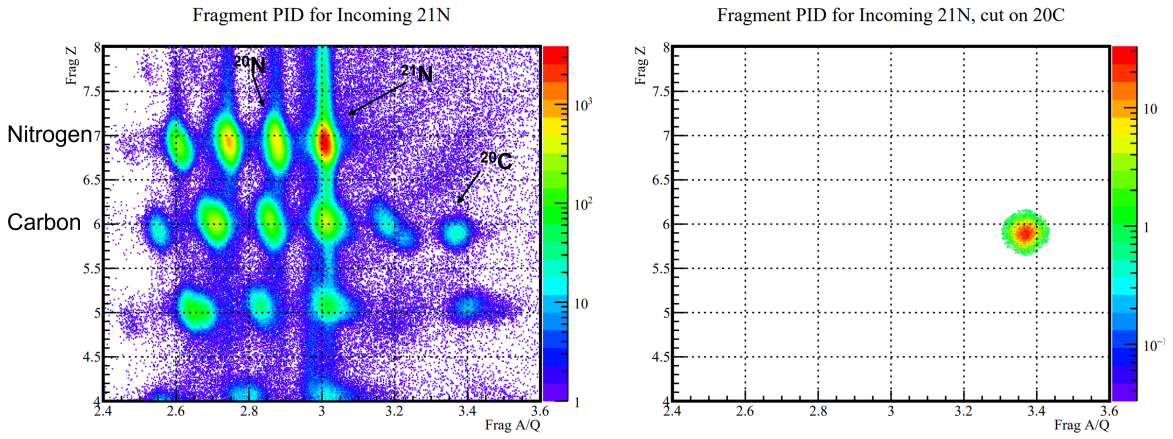

Figure 4.30: A comparison of the fragment particle identification and the three sigma gaussian cut on outgoing ^{20}C.

The fitting was performed without any gating on the downscaled beam, in order to determine the centre and sigma of the 2D gaussian cut. Then the cut was applied to the downscaled data, and the amount of ^{20}C was determined by the number of entries within the cut. This is shown in figure 4.30.

4.6 Transmission summary

The transmission of the beam was analysed, looking at both the radius and the angle of the beam on the target. This information is useful for determining the best limits which optimise the amount of incoming beam and reaction products. It is also necessary to know this information when determining the cross sections in order to determine the true amount of ^{20}C produced at the target position.

4.6.1 Position Transmission

The transmission analysis was performed by determining the amount of incoming ^{21}N, and then comparing it to the unreacted ^{21}N and other reaction products. This is because it is important to understand the fraction of ^{20}C that is lost between the target where it is produced, and the HODOSCOPE. The transmission was investigated by varying the radius of the target cut between 5 mm and 100 mm in 5 mm increments, with the objective of maximising the counts and transmission. An "onion plot" is shown in figure 4.31. Each point in the onion plot represents the percentage of the incoming ^{21}N that makes it to the HODOSCOPE as either unreacted ^{21}N or a reaction product between the point shown and the previous point.

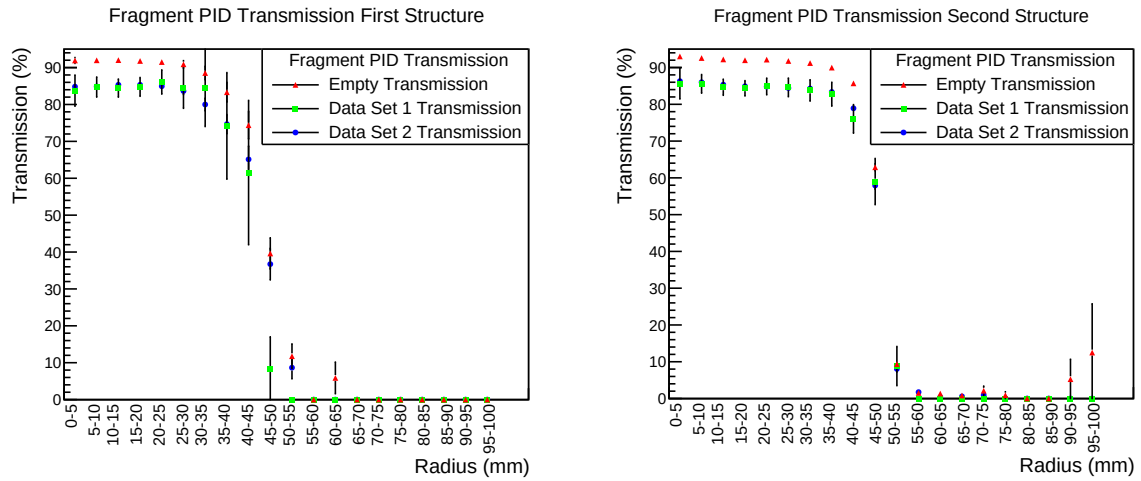

Figure 4.31: An onion plot showing the transmission of the unreacted beam and reaction products with varying target radius cuts.

This has been investigated for the empty target data, and the two target data sets, as well as the two structures of incoming ^{21}N.

The transmission of fragments is very similar for data set one and two, but shows a significant difference when compared to the empty target data, with much lower transmission. There is also a difference between all data sets when comparing the two incoming structures of ^{21}N. It is seen that the first structure, which is the smaller of the two, resulting in higher statistical uncertainty, has the transmission drop off at a smaller target cut radius. This is because the first structure is significantly offset from the centre of the target in comparison to the second structure. In all cases, the transmission remains steady up until 30 mm, therefore this was chosen as the target cut. At high radius, the transmission is very close to zero because at high radii, there are very few incoming counts, and most of these counts would be blocked by the target holder. In this region, there are statistical fluctuations, where a single count being recorded at the HODOSCOPE for the slice can result in an increasing transmission percentage, which can be seen in the 95-100 mm slice in the right panel of figure 4.31 for the empty transmission.

The transmission for each data set and the both structures of incoming ^{21}N was used to determine the most appropriate target cut, which maximises the size of the cut, whilst ensuring that the beam does not impinge the target holder, and transmission remains high.

In order to determine the transmission of ^{20}C, using the 30 mm target cut determined using the onion plot method, the amount of incoming ^{21}N was compared to the unreacted ^{21}N at the HODOSCOPE for both data sets and both structures. This was done as ^{21}N is well centred within the HODOSCOPE, and the analysis of ^{20}C shows that it is also well contained within the HODOSCOPE, and is not found in the paddles at the edge of the HODOSCOPE. The transmission and the uncertainty in the different measurements of incoming and out-

going ^{21}N follows equation 4.27.

$$(T \pm \delta T) = \frac{N_{^{21}N_{out}}}{N_{^{21}N_{in}}} \pm \left(\left(\frac{N_{^{21}N_{out}}}{N_{^{21}N_{in}}} \right) \times \sqrt{\left(\frac{\delta N_{^{21}N_{out}}}{N_{^{21}N_{out}}} \right)^2 + \left(\frac{\delta N_{^{21}N_{in}}}{N_{^{21}N_{in}}} \right)^2} \right) \tag{4.27}$$

As ^{20}C is formed in the middle of the target on average, the transmission of ^{20}C is given by the average of the empty target and target transmission values, as seen in equation 4.28.

$$(T \pm \delta T) = \frac{T_{empty} + T_{target}}{2} \pm \sqrt{\left(\frac{\delta T_{empty}}{2} \right)^2 + \left(\frac{\delta T_{target}}{2} \right)^2} \tag{4.28}$$

The transmission of the different data sets and both different structures is shown in table 4.7.

Data Set	Transmission	Statistical Uncertainty	Systematic Uncertainty
Data Set 1, Structure 1	80.7%	0.6%	0.5%
Data Set 1, Structure 2	81.2%	0.5%	0.5%
Data Set 2, Structure 1	81.0%	0.2%	0.5%
Data Set 2, Structure 2	81.6%	0.1%	0.5%
Narrow Momentum, Structure 1	78.0%	0.2%	0.5%
Narrow Momentum, Structure 2	73.9%	0.1%	0.5%

Table 4.7: The transmission of the different data sets and its uncertainty.

4.6.2 Angle Transmission

The transmission of the beam for varying angles was also investigated in the same way. In this case the angle was varied between 0 and 0.1 radians in increments of 0.01 radians. The result is shown in the onion plot in figure 4.32. In this case the target cut was fixed to 30 mm. The two target data sets were analysed, as well as the empty target data. It is seen that the introduction of the target introduces a large effect in the transmission. For the empty target data, there is only a small decrease in the transmission at larger angles, while both target data sets show a steady decrease in the transmission at larger angles. Figure 4.32 does not show a sudden cut off in the transmission due to materials such as the SAMURAI magnet unlike the target radius transmission.

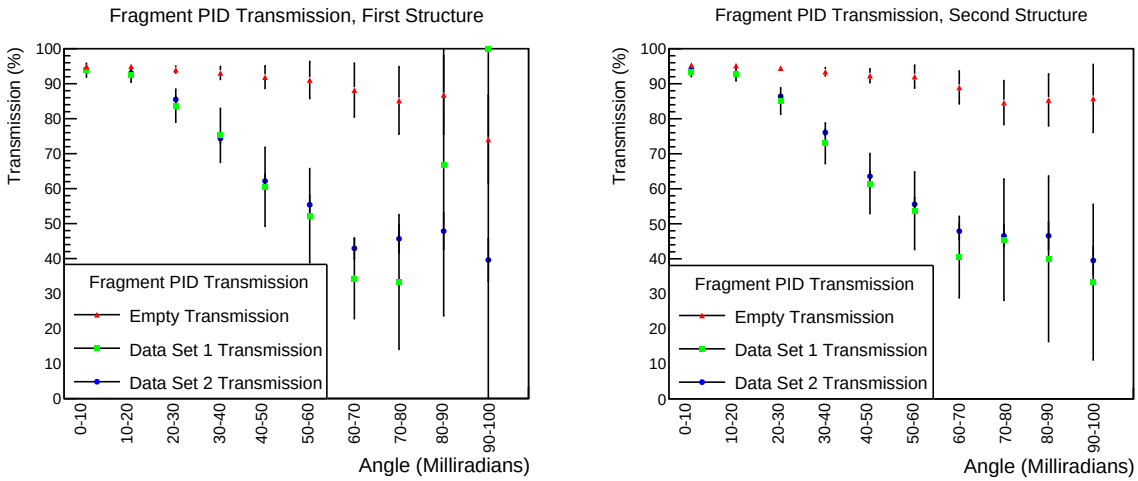

Figure 4.32: An onion plot showing the transmission of the unreacted beam and reaction products with varying FDC2 beam angle cuts.

Chapter 5

Results

5.1 Inclusive Cross Section

5.1.1 Inclusive Cross section calculation

When determining the inclusive cross section, there were three different data sets that were analysed. These include data set one, which contains runs dayone0276-0283, and data set two, which contains runs dayone0284-0310, dayone0318 and dayone0321-0325. The final data set that is included is the narrow momentum run, dayone0275. Data set one and two have different down scale beam factors, and different live times, which as a result makes it necessary to analyse them separately. Furthermore, as discussed previously, there are two different structures for the incoming ^{21}N which have slightly different transmissions as well as slightly different energies. The narrow momentum run does not contain any downscaling, as a result it is not suitable to be used in the exclusive cross section, but can be used as a source of additional statistics for the inclusive cross section. As there are two structures, each are analysed separately. The different data sets are then combined by taking a weighted average.

The first quantity that needs to be considered is the measurement of the incoming and outgoing ions, and their uncertainty. The statistical and systematic uncertainty in a measurement is given by equation 5.1.

$$N_{ion} \pm \delta N_{ion\ stat} \pm \delta N_{ion\ sys} = N_{ion} \pm \sqrt{N_{ion}} \pm \left(N_{ion} \times \left(1 - \left(0.997^2\right)\right)\right) \tag{5.1}$$

Where N_{ion} is the quantity of the incoming ion or fragment of interest, $\delta N_{ion\ stat}$ is the statistical uncertainty in the measurement of the incoming ion or fragment of interest and $\delta N_{ion\ sys}$ is the systematic uncertainty in the measurement of the incoming ion or fragment of interest, introduced by the 2D gaussian cut over a three sigma range. This is repeated for each measurement of the incoming/outgoing ^{21}N and the outgoing ^{20}C.

As a result the cross section is given by equation 5.2.

$$\sigma \pm \delta\sigma = \frac{N_{20_C} \pm \delta N_{20_C}}{(N_{21_N} \pm \delta N_{21_N}) \times (n \pm \delta n) \times (T \pm \delta T)} \tag{5.2}$$

Where n is the target nuclei per cm^2 of the target, and T is the transmission efficiency, determined in table 4.7. The area density is calculated to be (8.970±0.027)$\times 10^{22}$ target nuclei cm^{-2}. To combine the different values and their uncertainties, the inclusive cross section is given by equation 5.3.

$$\sigma_{inclusive} \pm \delta\sigma_{inclusive} = \frac{N_{20_C} \pm \delta N_{20_C}}{(N_{21_N} \times n \times T) \pm \left((N_{21_N} \times n \times T) \times \sqrt{\left(\frac{\delta N_{21_N}}{N_{21_N}}\right)^2 + \left(\frac{\delta n}{n}\right)^2 + \left(\frac{\delta T}{T}\right)^2} \right)} \tag{5.3}$$

The values for the cross section and its uncertainties given in equation 5.3 need to be multiplied by 1×10^{27} in order to convert to millibarns. These calculations are done for each data set as they cannot be compared like for like. To produce the final value, the weighted average of all the data sets is given by equation 5.4.

$$\sigma_{mean} \pm \delta\sigma_{mean} = \frac{\sum \frac{\sigma_i}{\delta\sigma_i^2}}{\sum \frac{1}{\delta\sigma_i^2}} \pm \frac{1}{\sum \sqrt{\frac{1}{\delta\sigma_i^2}}} \tag{5.4}$$

By analysing the different structures for each data set, the inclusive cross section is determined to be $\mathbf{5.73 \pm 0.29_{stat} \pm 0.05_{sys}}$ **mb**. The inclusive cross section of each data set and structure is shown in table 5.1.

In the case of the inclusive cross sections calculated for structure one and two in data set one, the statistical uncertainty of the measurement is rather high. This is because the downscaling used for the beam is much higher, resulting in fewer counts being recorded by the DAQ. This is reflected in the statistical uncertainty for these two values which is much larger. This data set is used because there is no downscaling for DALI2, resulting in higher statistics for the exclusive cross section, discussed next in section 5.2. When taking the final inclusive cross section into account, the large statistical uncertainty in the data set one values means that when the weighted average is taken, these values contribute very little to the final result.

Data Set	Incoming ^{21}N	Outgoing ^{20}C	Inclusive Cross Section (mb)	Statistical Uncertainty (mb)	Systematic Uncertainty (mb)
Data Set 1, Structure 1	10083	5	6.85	3.07	0.07
Data Set 1, Structure 2	16190	9	7.63	2.54	0.08
Data Set 2, Structure 1	329659	133	5.56	0.48	0.06
Data Set 2, Structure 2	591624	250	5.77	0.37	0.06
Narrow Momentum, Structure 1	64056	27	6.02	1.16	0.07
Narrow Momentum, Structure 2	180378	68	5.69	0.69	0.06
Weighted average	-	-	**5.73**	**0.29**	**0.05**

Table 5.1: The inclusive cross section for each data set used to calculate the final inclusive cross section.

5.2 Exclusive 2^+ Cross Section

The determination of the 2^+ cross section in ^{20}C is done using the verified GEANT4 simulation, discussed in section 4.4.3. The first step in determining the exclusive 2^+ cross section was to use analysed data, and split it into the four different data sets with their different downscaling and different structures. The narrow momentum run is not used in this case as there is no downscaling on the beam, therefore it is inappropriate to include this data. Next a GEANT4 simulation was run.

For the EventGenerator stage of the simulation, the characteristics of the beam were introduced. Taking the analysed data, the incoming energy of the ^{21}N beam was determined. This was done using the time of flight of the beam. The energy of two structures in both data sets as well as the position of the beam on the target is shown in table 5.2.

Data Set	^{21}N Beam Energy (MeV/U)	FWHM (MeV/U)	^{21}N Beam Position X (mm)	FWHM X (mm)	^{21}N Beam Position Y (mm)	FWHM Y (mm)
Data Set 1, Structure 1	261.8	8.3	-5.1	11.7	0.1	8.9
Data Set 1, Structure 2	267.6	16.9	-7.2	12.6	1.9	10.7
Data Set 2, Structure 1	261.9	8.3	-5.3	11.7	0.2	8.9
Data Set 2, Structure 2	268.0	17.2	-7.0	12.6	1.9	10.8

Table 5.2: The beam energy and FWHM for incoming ^{21}N for each data set used in the simulation of DALI2.

The beam position and angle on the target was determined using information from the BDCs. The mass change was entered to simulate the proton knockout reaction. In total, 10 million incoming ^{21}N ions were simulated. The energy loss of the beam within the target is also accounted for in the simulation. In order to improve the fitting of the gamma ray in each data set, the centre of the peak was determined by fitting the gamma ray using a gaussian fit with two exponentials. An example is shown in figure 5.1.

In the fitting box, p0-p3 are the fitting parameters for the two exponentials used to replicate the background. The parameters p4-p6 are the fitting parameters of the gaussian fit, where the p5 parameter is the centre of the gaussian fit, and it is this energy that is used to simulate the response of a gamma ray with this mean energy. The central energy for each data set is shown in table 5.3.

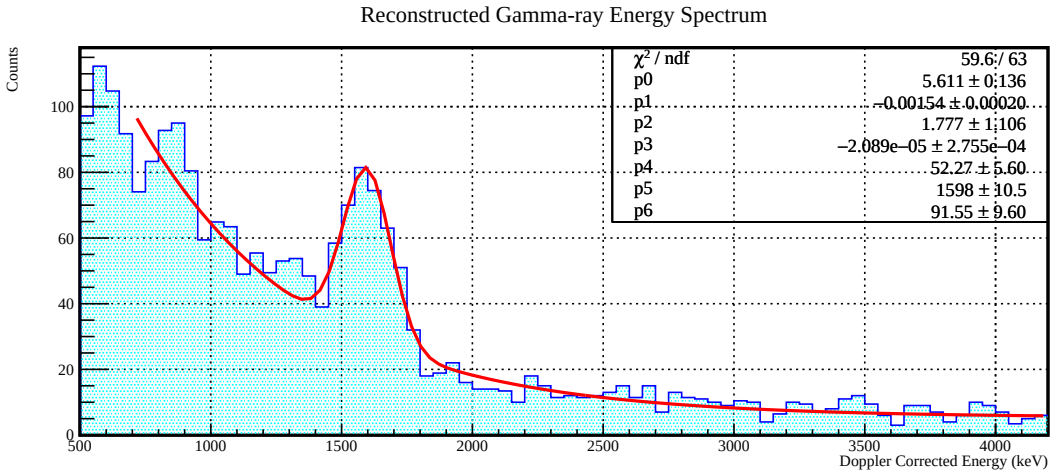

Figure 5.1: The DALI2 spectrum for ^{20}C, fitted with a convoluted fit comprising of a gaussian plus two exponentials. This is used to determine the central energy of the peak.

Data Set	^{20}C 2^+ Energy (keV)	Energy Uncertainty (keV)
Data Set 1, Structure 1	1585	7
Data Set 1, Structure 2	1625	9
Data Set 2, Structure 1	1613	6
Data Set 2, Structure 2	1598	11

Table 5.3: The central energy of the 2^+ state in ^{20}C determined for each data set used in the simulation of DALI2.

As shown in figure 5.2, there are no other known gamma rays in ^{20}C, therefore the simulation only needs to include this one transition [71].

After this, the simulation does not match real values such as decay probabilities, and level population probabilities as they are unknown. In order to determine the exclusive 2^+ cross section, it is assumed in the simulation that the probability of the proton knockout reaction resulting in the excited 2^+ state of ^{20}C is 100%. It is also assumed that the probability of decay from the 2^+ state to the ground state is 100%. It is not necessary to simulate background sources in the case of the beam data. This is because the gamma rays are selected on the incoming ^{21}N beam and outgoing ^{20}C reaction products, which is a very restrictive cut. Furthermore, in the case of the calibration data analysed previously, DALI2 was self triggering which means that any gamma ray, including background sources will trigger the DAQ. In the case of the beam data, DALI2 is not self triggered and looks for gamma rays in coincidence with incoming ions. As the background sources are also stationary, the Doppler correction of any events that could be present (although extremely unlikely) will smear out any peaks, therefore the background can be approximated using two exponential functions, one for the

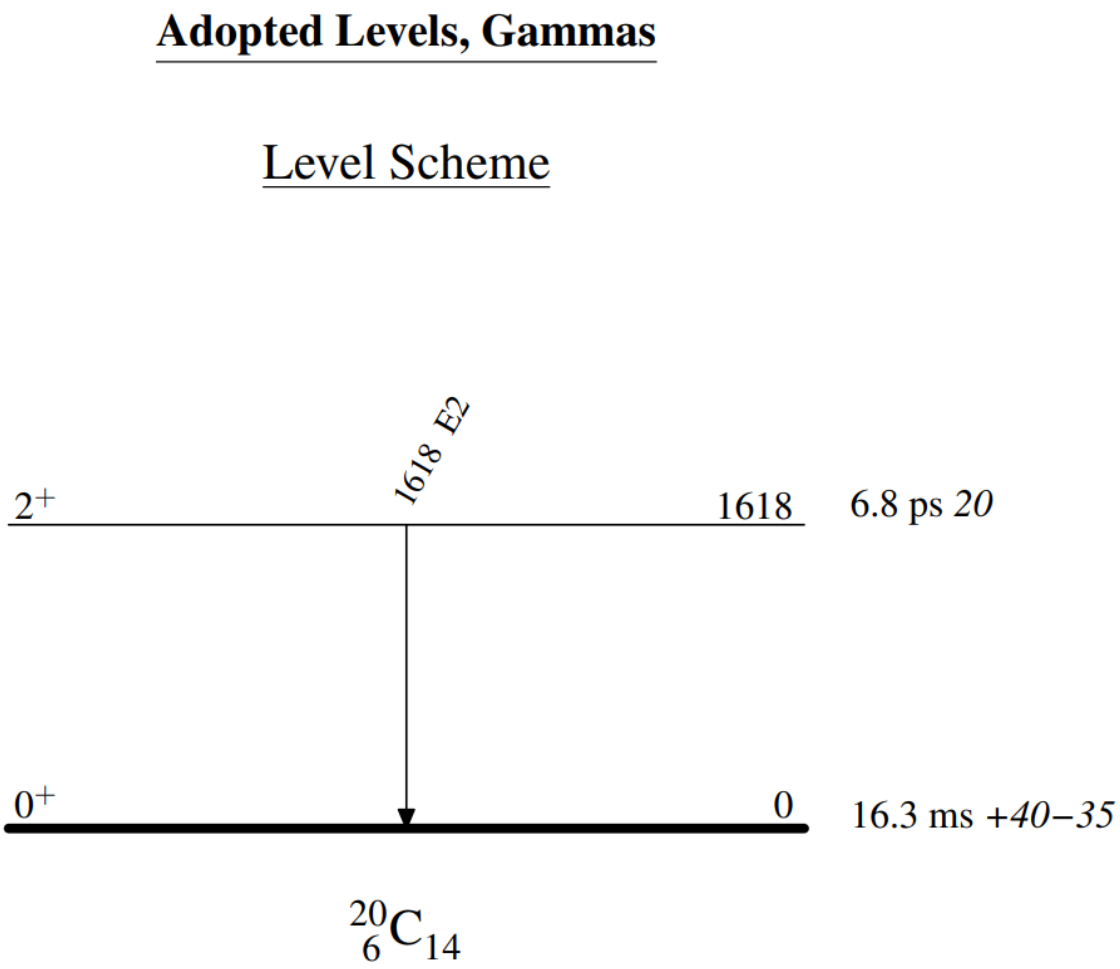

Figure 5.2: The level scheme for ^{20}C, from the NNDC database [71].

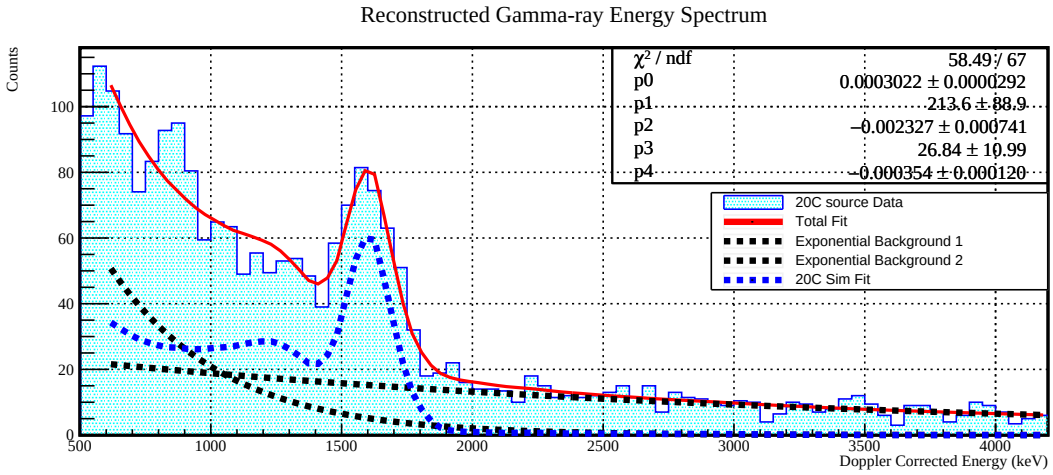

Figure 5.3: The DALI2 spectrum for ^{20}C, fitted with the simulated response for the central energy shown in figure 5.1. The p0 fitting parameter represents the scaling of the simulated response function. It is this value which is used to determine the amount of ^{20}C produced in the 2^+ state.

low energy region, which has higher counts, and one for the higher energy region which has fewer counts.

The EventBuilder stage is similar to the EventBuilder parameters used in simulating the stationary sources which were used to validate the simulation. The only difference is the beta (velocity as a percentage of the speed of light of the outgoing fragment) resolution parameter, which was determined using the FWHM of the beta peak for outgoing ^{20}C. The Reconstructor stage of the simulation sets an energy threshold of 300 keV. The beta value was determined using the experimental value, this is used for the Doppler correction.

The two data sets are then fitted using the result of the GEANT4 simulation, with an exponential background. The p0 value, which represents the scaling of the simulation is then multiplied by the number on incoming ions, in this case 10 million. This value is then taken to be the number of ^{20}C ions produced in the 2^+ state. In the case of the second data set, DALI2 is downscaled by a factor of four, therefore the value produced by the fitting has to be multiplied by four to recover the original counts of ^{20}C produced in the 2^+ state. After this, the method used to determine the inclusive cross section was followed to calculate the exclusive cross section of the 2^+ state, with the only difference being the amount of incoming ^{21}N. This is taken to be the ^{21}N measured using the downscaled beam, multiplied by the downscaling factor. The data was fitted between the range of 600-4200 keV, with a binning of 50 keV/bin. This was done as it minimised the fitting uncertainty. An example of the fitting is shown in figure 5.3.

The result of the fitting for each data set is shown in table 5.4, with a final value determined to be $\mathbf{1.47 \pm 0.08}_{stat} \pm \mathbf{0.02}_{sys}$ **mb**.

Data Set	Incoming ^{21}N	Outgoing ^{20}C	Outgoing ^{20}C Uncertainty	Exclusive Cross Section (mb)	Statistical Uncertainty (mb)	Systematic Uncertainty (mb)
Data Set 1, Structure 1	10083000	1155	139	1.58	0.19	0.04
Data Set 1, Structure 2	16190000	1743	198	1.48	0.17	0.04
Data Set 2, Structure 1	65931800	7066	827	1.48	0.17	0.04
Data Set 2, Structure 2	118324800	12088	1168	1.40	0.13	0.04
Weighted average	-	-	-	**1.47**	**0.08**	**0.02**

Table 5.4: The exclusive cross section for each data set used to calculate the final exclusive cross section note that for the incoming and outgoing ions, the values are multiplied by the downscale values, 1000 for data set 1 and 200 for data set 2.

5.3 Proton Amplitude

In order to determine the proton amplitude of the 2^+ state in ^{20}C, the exclusive cross section of the ground state (see equation 3.5), the exclusive cross section of the 2^+ state and the inclusive cross section are needed. The exclusive cross section of the ground state is given by equation 5.5.

$$\sigma_{G.S.} = \sigma_{Inclusive} - \sigma_{2^+} \tag{5.5}$$

The cross section of the ground state was determined to be $\mathbf{4.27 \pm 0.27}_{stat} \pm \mathbf{0.06}_{sys}$ **mb**. The proton amplitude is determined by taking the ratio of the cross section of the 2^+ state to the cross section of the ground state. This is given by equation 5.6.

$$\beta^2 = \frac{\sigma_{2^+}}{\sigma_{G.S.}} \div \frac{5}{2} \tag{5.6}$$

Taking all of the data into account, the proton amplitude is determined to be $\mathbf{13.73 \pm 1.16}_{stat} \pm \mathbf{0.26}_{sys}$ %. A comparison of this value with previous work and lighter isotopes of even-even carbon isotopes is shown in figure 5.4.

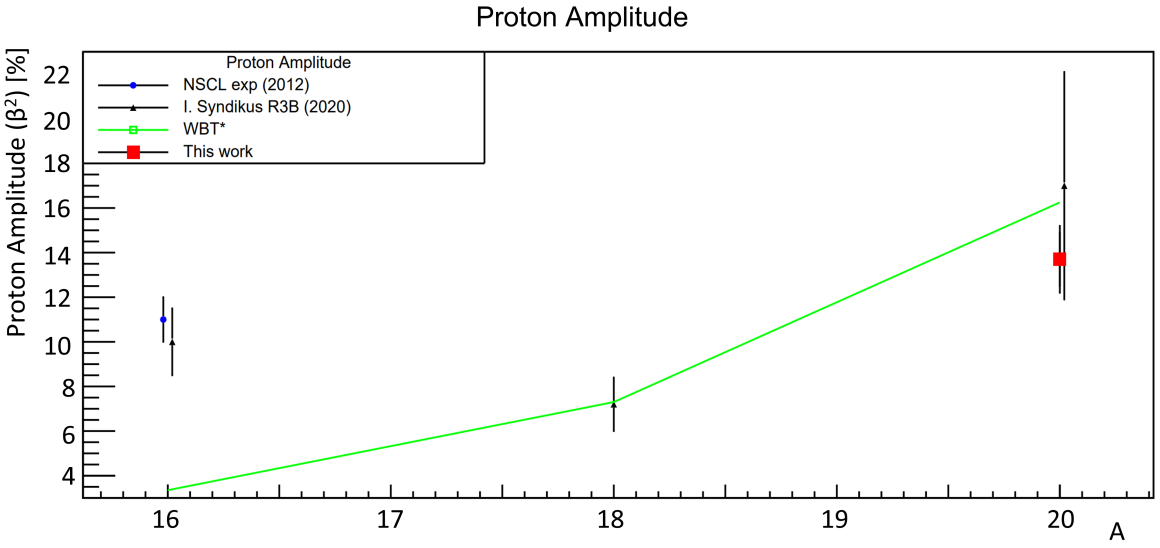

Figure 5.4: The proton amplitude for ^{20}C measured in this work, show in red, plotted in relation to previous work showing the proton amplitude of ^{16,18,20}C [42][33]. Theoretical values for the proton amplitude were determined with shell-model calculations using the WBT* interaction, seen in green, in reference [18] and [41].

Chapter 6

Discussion and conclusion

6.1 Interpretation of Proton Amplitude

The proton amplitude was determined to be $\beta^2 = 13.73 \pm 1.16_{stat} \pm 0.26_{sys}$ %. The largest source of uncertainty came from the statistical uncertainty, of which the two largest sources were the measurement of ^{20}C (see table 5.1), and the fitting of the 2^+ peak (see table 5.4). As discussed in section 1.3.2, previous work has indicated the prevalence of the Z=6 sub-shell closure towards the neutron drip line, including ^{20}C, as seen in figure 1.7. However, as mentioned previously this has been called into question by the study of B(E2) values for ^{16,18,20}C. In the case of ^{16,18}C, the B(E2) values are consistently low indicating a low proton excitation, which indicates the sub-shell closure. In the case of ^{20}C, the B(E2) value shows a moderate increase indicating more proton excitations [32]. Similarly, previous measurements of the proton amplitude of ^{16}C by Petri et al. [42] and ^{16,18,20}C by Syndikus et al. [33] have shown low values for the proton amplitude in ^{16}C and ^{18}C, with an increase in the proton amplitude for ^{20}C. This again shows that the contribution of proton excitations for the 2^+ state in ^{16}C and ^{18}C is small. The only measurement of the proton amplitude of ^{20}C by Syndikus et al [33]. was determined to be 17.0 ± 5.1%, which suggests there may be an increase in the proton excitation compared to ^{16,18}C. However, this value has a large uncertainty, dominated by the low statistics in that measurement. The new measurement of the proton amplitude shown in this work is in agreement, whilst also having less uncertainty due to the better statistics. A summary of the proton amplitudes for even-even carbon isotopes is seen in table 6.1.

The new proton amplitude of ^{20}C that has been determined in this work is lower than the previous measurement, although it is still in agreement with the value determined by Syndikus et al [33]. When compared to the lighter isotopes of ^{16,18}C, the proton amplitude of ^{20}C suggests a moderate increase in its value, although with an overlap in the uncertainties. This result suggests that there is a modest increase in the proton contribution to the 2^+ state,which signals a modest reduction in the spin orbit splitting of the $1p_{1/2} - 1p_{3/2}$ gap as the

Isotope	^{16}C [42]	^{16}C [33]	^{18}C [33]	^{20}C [33]	**^{20}C This work**
Proton Amplitude	11(1.0)%	10.0(1.5)%	7.2(1.2)%	17.0(5.1)%	**13.73(1.42)%**

Table 6.1: A summary of the proton amplitude for even-even carbon isotopes, using previous work by [42] and [33] with the new value determined in this work.

neutron drip line is approached. The value determined is also significantly lower than that predicted by theory, ≥ 30% [32]. This result suggests that the reduction in the Z=6 sub-shell closure is smaller than previously indicated.

6.2 Future prospectives

6.2.1 Unbound states

The main focus of future work will be on the unbound states in ^{20}C. As discussed previously, the removal of a proton in the $p_{3/2}$ shell can result in the population of a 2^+ state or a 1^+ state. The main focus however would be on searching for the second unbound 2^+ state as predicted earlier, which has not been seen experimentally before. This would be expected to be at an energy of approximately 7 MeV, as guided by the proton dominated 2^+ state seen in ^{14}C. The discussion around the energies of the second excited state is discussed in section 3.5, and shown visually in figure 3.1.

With the energy of the 2^+_2 state expected to be found at 7 MeV, the state will be unbound. Therefore, the state will immediately decay with the emission of a neutron with the decay of ^{20}C shown in figure 6.1, which shows how the unbound second 2^+ state may decay to ^{18}C and two neutrons. The neutron separation energy of ^{20}C is 2.980 MeV [14], which forms an unbound state in ^{19}C well above the low neutron separation energy of $S_n = 580$ keV [14]. This results in the population of ^{18}C, which has a neutron separation energy of 4.18 MeV, with a second neutron being emitted. With such a high neutron separation energy in ^{18}C, it is expected that the excited state will decay to ^{18}C. Therefore, in order to analyse the 2^+_2 state in ^{20}C, it will be necessary to observe ^{18}C in the HODOSCOPE, two neutrons in NEBULA, and potential gamma decays from ^{18}C.

It is expected that the neutron emitted from ^{20}C will only carry away some of the energy, resulting in the population of an unbound state in ^{19}C, which will result in the emission of a second neutron. The energy carried away by the neutron is given by 6.1.

$$E_{neutron\ ^{20}C} = Ex\left(^{20}C\left(2^+_2\right)\right) - S_n\left(^{20}C\right) - Ex\left(^{19}C\right) \tag{6.1}$$

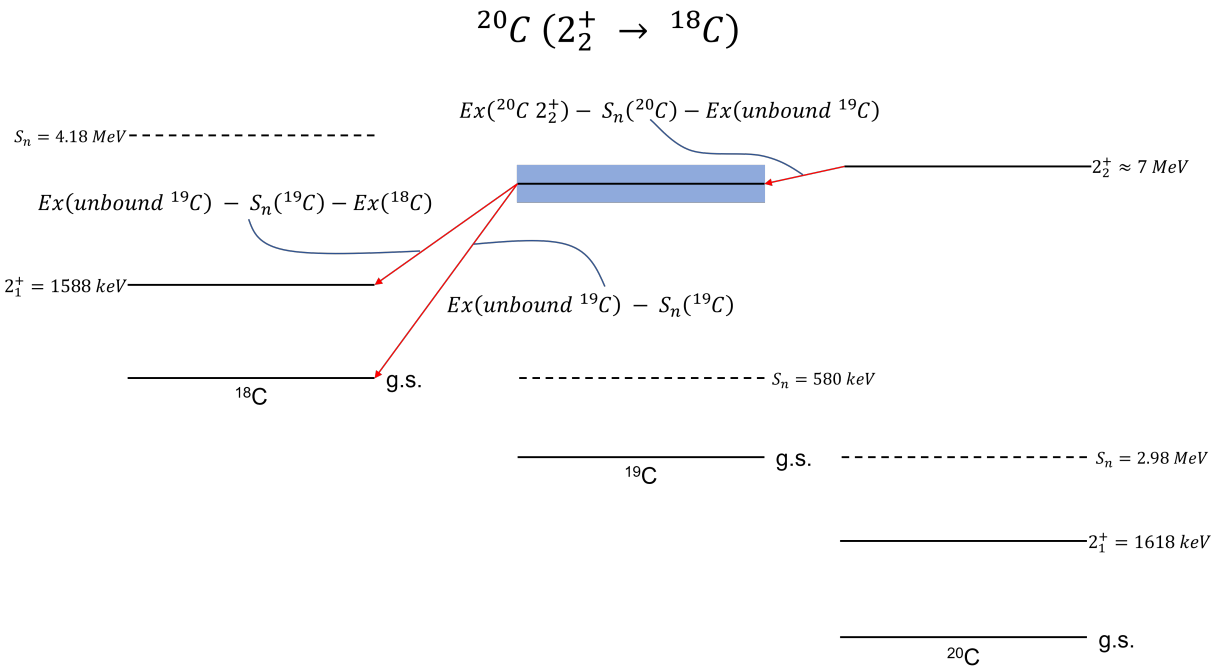

Figure 6.1: The expected energy of the second 2^+ state in ^{20}C is approximately 7 MeV. With the ≈3 MeV neutron separation in ^{20}C combined with the very low neutron separation energy in ^{19}C (580 keV [14]), it is expected that the unbound state will decay to an ^{18}C fragment, which will potentially be in an excited state, and two neutrons.

Where $Ex(^{19}C)$ is the energy of the unbound state in ^{19}C. The population of an unbound state in ^{19}C will result in the emission of a second neutron. The neutron separation energy of ^{18}C is 4.18 MeV, therefore with the second 2^+ state in ^{20}C expected to be at 7 MeV, it is not expected that an unbound state in ^{18}C will be produced. Therefore the second neutron that is emitted from ^{19}C could follow one of two scenarios. The neutron could either carry away all the energy from the unbound state, resulting in the population of the ground state of ^{18}C and the neutron carrying away an energy given by equation 6.2. The other option is that it may populate a bound state in ^{18}C that is lower in energy than the energy of the unbound state, as shown in equation 6.3.

$$E_{neutron\ ^{19}C} = Ex(unbound^{19}C) - S_n(^{19}C) \tag{6.2}$$

$$E_{neutron\ ^{19}C} = Ex(unbound^{19}C) - S_n(^{19}C) - Ex(^{18}C) \tag{6.3}$$

Based on this, the population of the second 2^+ state can be estimated. The proton amplitude of the 2_1^+ state was determined to be $\beta^2 = 13.73 \pm 1.42$ %. As the proton and neutron components of the 2^+ state are orthogonal, it is expected that the 2_2^+ state will be populated with $\alpha^2 = 86.27 \pm 1.42$ %. Therefore comparing the two values, it is expected that the cross

section of the 2_2^+ state would be approximately 6.3 ($^{86.27}/_{13.73} \approx 6.3$) times greater than the cross section of the 2_1^+ state. Therefore, the cross section of the 2_2^+ state (considering the error propagation) is expected to be $\sigma_{2_2^+} = 9.3 \pm 1.2\ mb$. By taking the downscaled beam and multiplying by the downscale factors, the amount of incoming ^{21}N is estimated to be approximately twenty one million. Depending on the outcome, it is possible to estimate the number of decays that will be observed.

The first case that needs to be accounted for is the population of an unbound state in ^{19}C, resulting in the emission of a second neutron. In this scenario, the second neutron carries away the all the energy of the unbound state, resulting in no gamma rays and needing to take the two neutron efficiency of NEBULA into account, which is 12% [52]. The transmission efficiency of ^{19}C or ^{18}C is assumed to be at least the same as ^{20}C. This is because ^{20}C is positioned well within the limits of the HODOSCOPE, and the position of the HODOSCOPE was chosen so that an A/Z=3 (which is the A/Z of ^{18}C) was centred, therefore the transmission would be expected to be greater than or equal to the transmission of ^{20}C, which was 81%. In the second case, the second neutron carries away only some of the energy, resulting in the population of a bound state in ^{18}C, which will decay via the emission of a gamma ray. In this case, the efficiency of DALI2 was taken to be the same as the efficiency of DALI2 in the bound state of ^{20}C as the 2^+ state in ^{18}C is at approximately the same energy. This efficiency is 11%. A summary of the number of decays expected to be seen in each scenario is shown in table 6.2.

Scenario	Expected Decays	Uncertainty
2 neutrons, no gamma ray	189,750	24,721
2 neutrons, with gamma ray	20,873	2,719

Table 6.2: A summary of the estimated number of decays observed from the second 2^+ state in ^{20}C.

Referring to the work on the exclusive cross section of the 2_1^+ state in ^{20}C (see section 5.2), the number of decays observed was just over 22,000. In the worst case scenario, where the two neutron efficiency of NEBULA and the efficiency of DALI2 needs to be taken into account, the number of decays that are expected to be observed for the second 2^+ state is similar to that seen in the bound 2^+ state. In the other case the number of decays expected to be observed only goes up.

In order to work on the unbound state, it will be necessary to use the NEBULA neutron detector. Details on the calibration that have already been performed can be seen in the appendix, in section B.2. As the state is unbound, the work relies on using invariant mass spectroscopy, which is detailed in section B.1. To perform this analysis, it will be necessary to measure the energy and momentum of the ^{18}C or ^{19}C fragment, and the one or two neutron

as well as any gamma rays that may be emitted. For the measurement of the gamma rays, an approach similar to that used in the bound state can be used. If there is an obvious gamma ray observed, the energy can be measured using a gaussian fit with exponential background, as seen in figure 5.1 in section 5.2. Once this has been performed, the response of DALI2 can be simulated using the GEANT4 simulation used previously. An improvement to the previously used method would be to simulate the response of DALI2 in 0.5-1 keV increments around the energy determined using the gaussian fit. These simulations could then be fitted to the data, and the fit with the lowest fitting uncertainty would be used as the determined energy, as well as for extracting the scaling of the simulation. This method could also be performed on the bound 2^+ state to reduce the uncertainty further. Furthermore, addback could be utilised to improve the statistics of DALI2.

6.3 Summary

In this thesis, the analysis of the proton amplitude of ^{20}C following a one-proton knockout reaction from ^{21}N was presented. In order to achieve this, a ^{48}Ca primary beam was delivered by the RIBF facility, and impinged on a Be primary target to produce a cocktail beam. The BigRIPS separator was used to identify incoming ^{21}N ions, which were transported to the SAMURAI spectrometer for secondary reactions on a carbon target, producing ^{20}C among other reaction products.

Using the model of two state mixing [32], introduced in section 3.5, the proton amplitude was determined by measuring inclusive and exclusive cross sections. From this, the proton amplitude of the 2^+ state of ^{20}C was determined to be $\beta^2(^{20}C_{2^+}) = 13.73 \pm 1.42\%$. This signals an increase in the amount of proton excitations, relative to other neutron rich, even-even carbon isotopes. This increase can be interpreted as a decrease in the gap between the $1p_{3/2}$ and $1p_{1/2}$ orbits, as more neutrons in the $1d_{5/2}$ orbit has a repulsive effect on the $1p_{3/2}$ proton orbit.

Finally, the cross section and possible decay statistics were discussed for the second, unbound 2^+ state according to different possible decay possibilities, based on the determined proton amplitude.

Appendix A

A.1 Electronics Schemes

The electronics schemes used in the Day-One campaign are shown in figures A.1, A.2, A.3, A.4 and A.5.

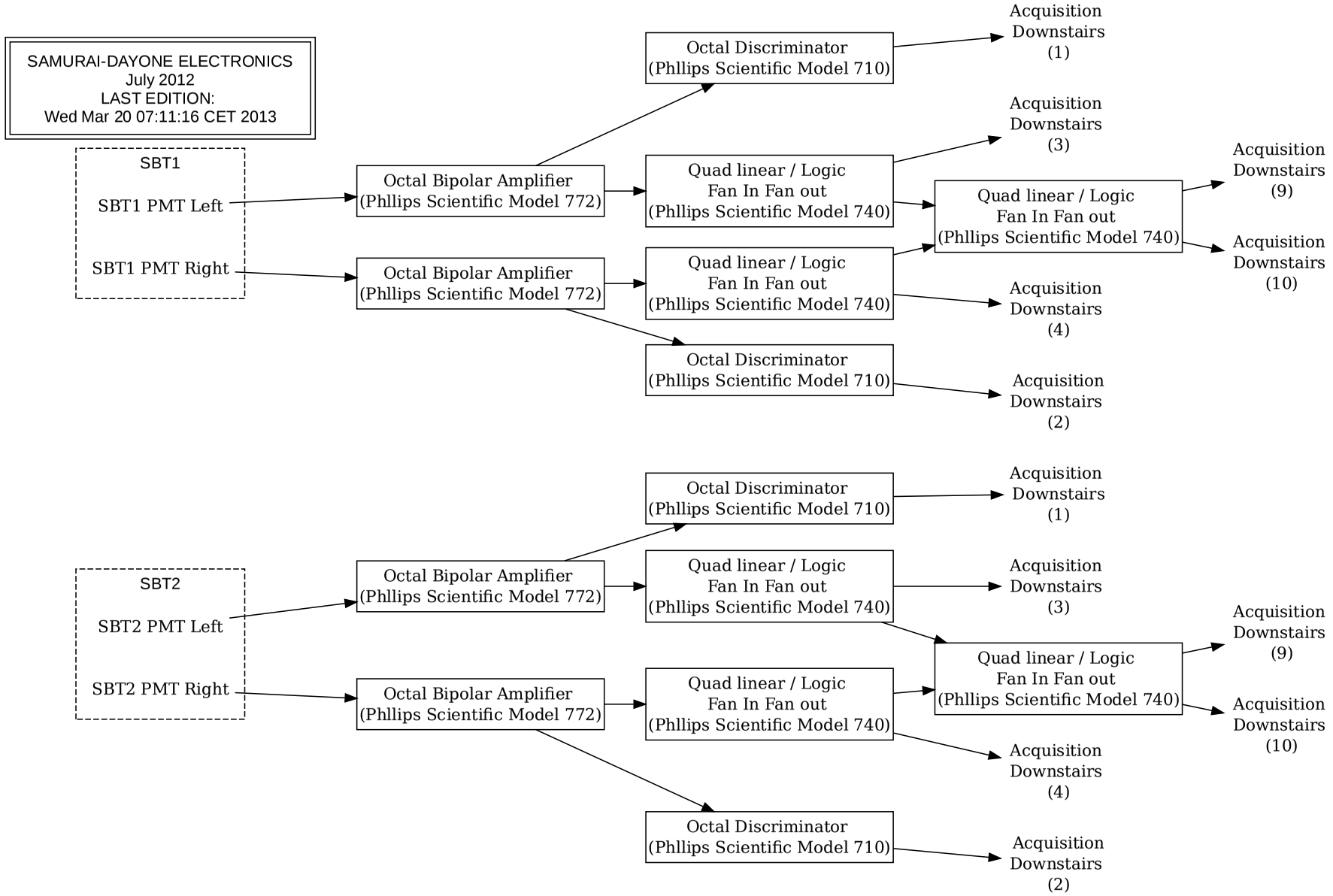

Figure A.1: The SBT electronics scheme, adopted from [72].

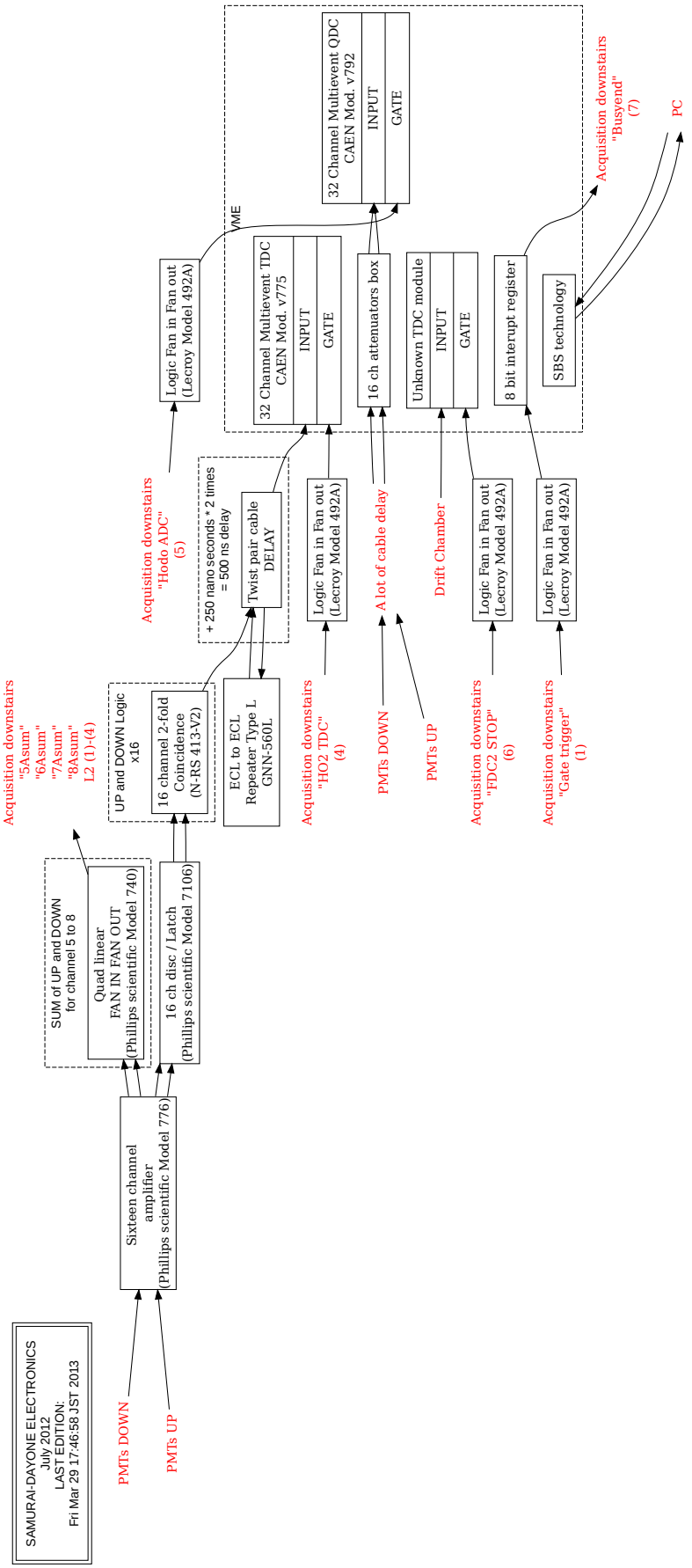

Figure A.2: The HODOSCOPE electronics scheme, adopted from [73].

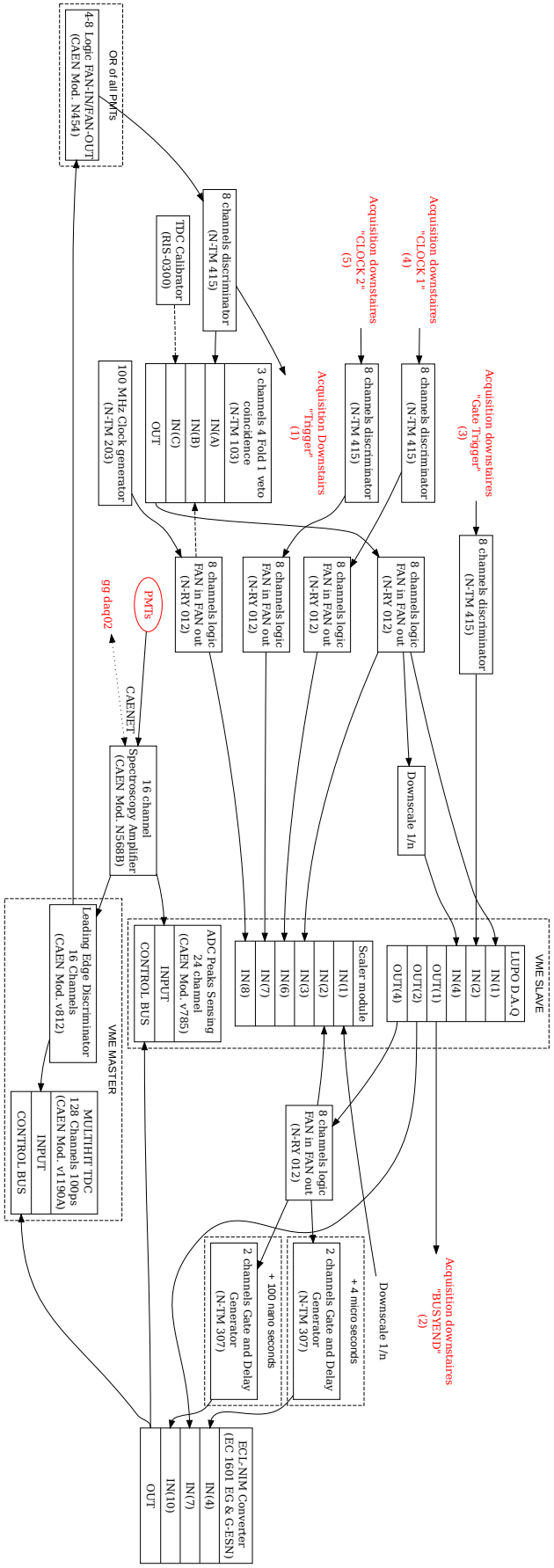

Figure A.3: The DALI2 electronics scheme, adopted from [74].

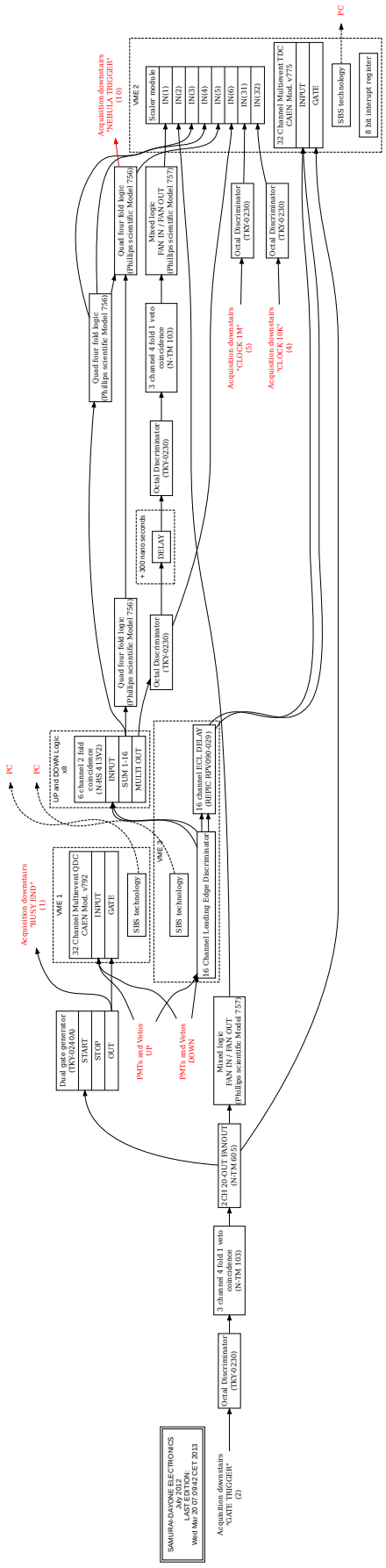

Figure A.4: The NEBULA electronics scheme, adopted from [75].

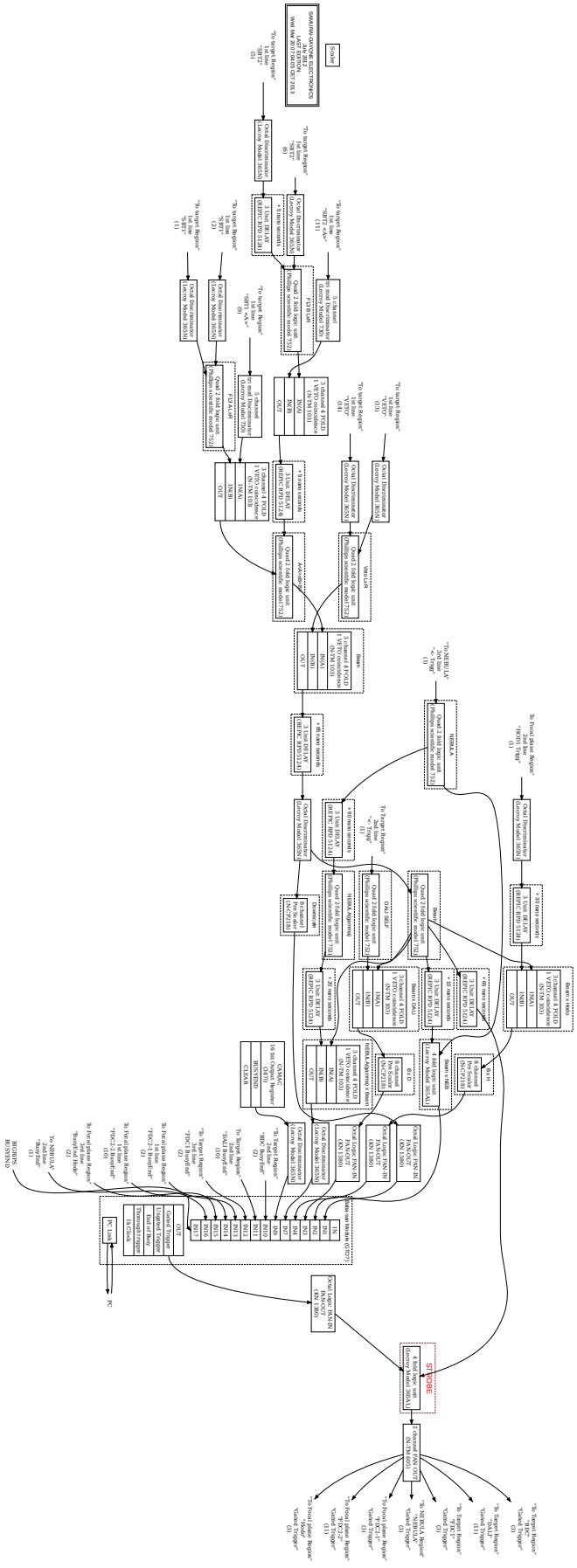

Figure A.5: The strobe electronics scheme, adopted from [76].

Appendix B

B.1 Invariant mass spectroscopy

In order to determine the energy of an unbound state, the invariant mass method can be used. This is useful for the study of unbound states as it accounts for the momentum of the daughter nucleus and the neutron. The invariant mass is given by equation B.1.

$$E_{inv} = \sqrt{(E_f + E_n)^2 + (P_f + P_n)^2} \tag{B.1}$$

Where E_f and P_f is the energy and momentum of the heavy fragment respectively and E_n and P_n is the energy and momentum of the neutron. From this, the relative energy of the unbound state can be calculated using equation B.2.

$$E_{rel} = E_{inv} - (M_f + M_n) \tag{B.2}$$

From this, the excitation energy (E_x) of the state can be calculated using equation B.3.

$$E_x = E_{rel} + S_n(+E_\gamma) \tag{B.3}$$

Where S_n is the neutron separation energy, and E_γ is the energy of any emitted gamma ray. In the context of this reaction, ^{20}C is formed in the unbound 2^+ state and immediately decays to ^{19}C, a neutron, and a gamma ray may also be emitted. Depending on the energy carried away by the neutron emitted from ^{20}C, it is possible an unbound state in ^{19}C will be populated, resulting in the emission of a second neutron and ^{18}C.

B.2 NEBULA

B.2.1 Light Output Calibration

As discussed previously, NEBULA is made up of 120 plastic bars, coupled to a photomultiplier tube at either end. Therefore each of the 240 PMTs need to be calibrated. In order to

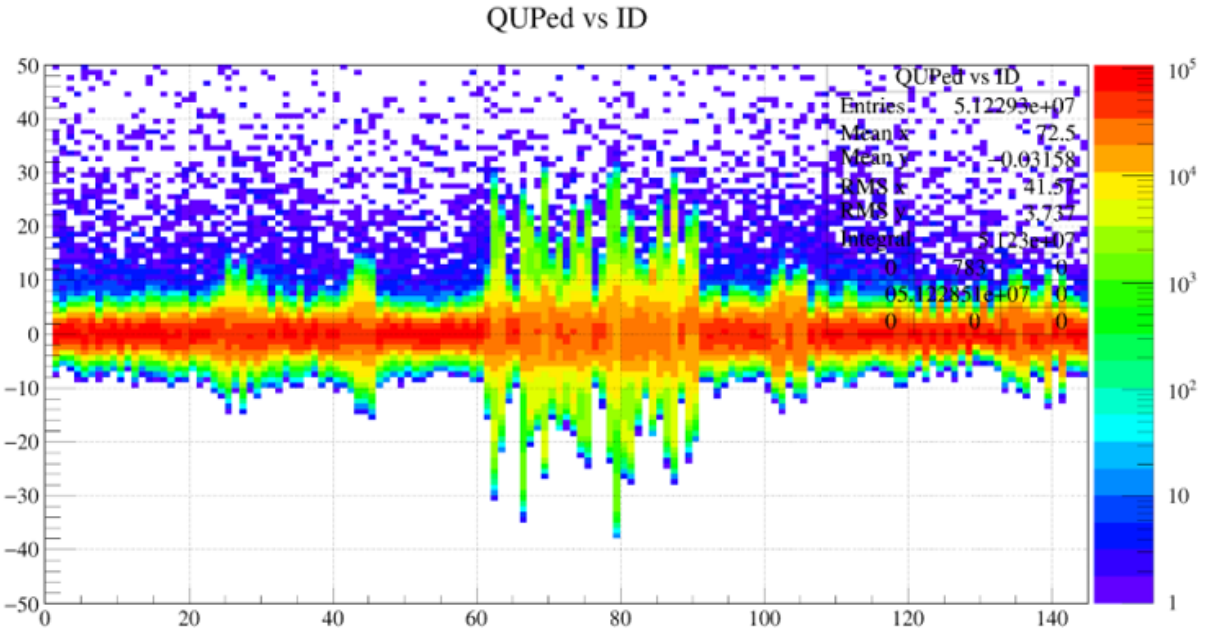

Figure B.1: The NEBULA pedestal, calibrated to be centred around an energy of 0.

do this the pedestal and two sources (with different energies) are used to calibrate NEBULA. In addition to this, there are two veto layers used to identify charged fragments entering NEBULA. Each layer comprises of 12 wider but thinner paddles, coupled to photomultiplier tubes at either end.

B.2.2 Pedestal

The first calibration that is performed is the pedestal calibration. This is because the pedestal is the minimum signal observed when there is no radiation. Therefore this pedestal value corresponds to the signal equal to an energy of 0. This is seen in figure B.1.

B.2.3 AmBe source

The AmBe source produces γ-rays at an energy of 4.4 MeV. This is used as a lower energy source in comparison to the cosmic rays that will be discussed later. The calibration of NEBULA using the AmBe source relies on the determination of the compton edge. This is because the the cross section of the photoelectric effect is very low, but the compton edge is fixed. The compton edge can be determined using equation B.4 [77].

$$E_{edge} = \frac{E_\gamma}{\frac{mc^2}{2E_\gamma} + 1} = 4.158\ MeV \tag{B.4}$$

In order to determine the mid-point of the slope, which corresponds to the compton

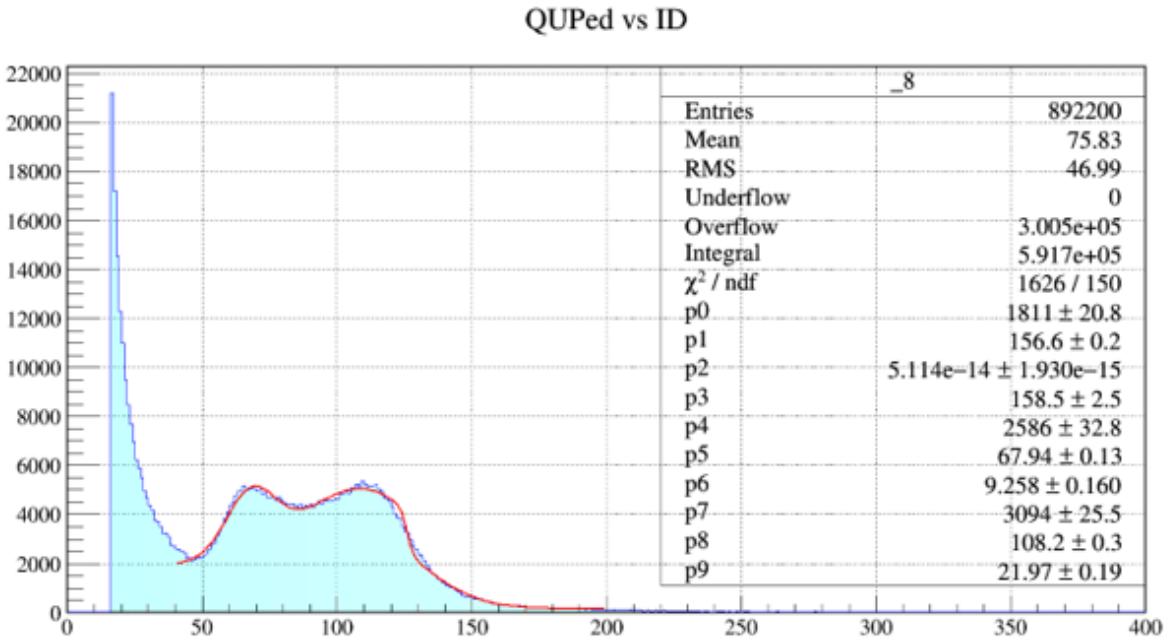

Figure B.2: The response of NEBULA with an AmBe source, fitted with a convolution of a fermi fit plus two gaussians to determine the compton edge.

edge, with an ADC channel corresponding to an energy of 4.158 MeV, a fermi function was used, shown in equation B.5. The data was fitted using this fermi function, convoluted with two gaussian peaks in order to better match the line shape of the signal, shown in figure B.2.

$$f(E) = \frac{p_0}{1 + e^{\left(\frac{E - E_{CE}}{p_1}\right)}} + p_2 \tag{B.5}$$

In equation B.5, p_0, p_1 and p_2 are parameters, and E_{CE} is the parameter that represents the compton edge. E represents the ADC channel. The convolution of the fermi function with the two gaussians is shown in equation B.6, where the first term is the fermi function, and the second and third terms are the gaussian fits.

$$f(E) = \left(\frac{p_0}{1 + e^{(E - E_{CE}/p_1)}} + p_2\right) + \left(p_3 \times e^{\left(-(x-p_4)^2/2p_5^2\right)}\right) + \left(p_6 \times e^{\left(-(x-p_7)^2/2p_8^2\right)}\right) \tag{B.6}$$

An example of the fitting, using equation B.6 to determine the compton edge of the AmBe source is seen in figure B.2.

B.2.4 Cosmic rays

Cosmic rays are used to calibrate NEBULA with a higher energy. The collision of cosmic rays within the atmosphere creates muons, which have an energy of approximately 4 GeV at the earths surface. These 4 GeV muons deposit approximately 29.9 MeV in the plastic paddles of NEBULA [77]. This is then fitted using a Landau fit, convoluted with an exponential back-

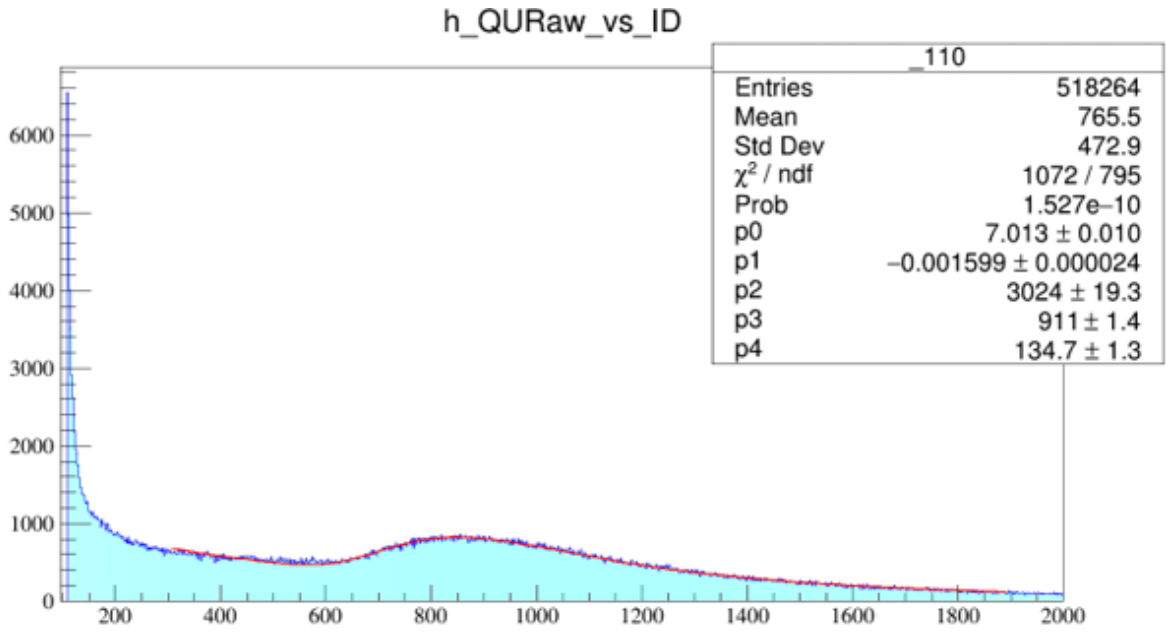

Figure B.3: The response of NEBULA with a muon produced by the interaction of a cosmic ray in the atmosphere, fitted with a convolution of a landau function plus an exponential.

ground, shown in figure B.3.

Using these three points, the energy deposited in each PMT was determined using equations B.7 and B.8.

$$Q_{ped} = Q_{raw} + A \tag{B.7}$$

$$Q_{cal} = B \times Q_{ped} \tag{B.8}$$

Knowing the calibrated energy in each PMT, the total energy deposited is then calculated using the geometric average of both PMTs, which is given by equation B.9.

$$Q_{total} = \sqrt{Q_{up} \times Q_{down}} \tag{B.9}$$

B.2.5 Time Calibration

The calibration of the time that neutrons arrive in the HODOSCOPE can be used as a first method of determining the energy of neutrons. This is because the energy of a neutron is directly related to the velocity, and therefore time of flight, of the neutron.

B.2.6 TDC Calibration

The first step in calibrating the time of flight is to convert from the raw TDC, to real time. This is done in the same way as the SBTs, using a pulser. The run used was dayone0435, which has a range of 320 ns and emits pulses which are separated by 10 ns. These peaks were then

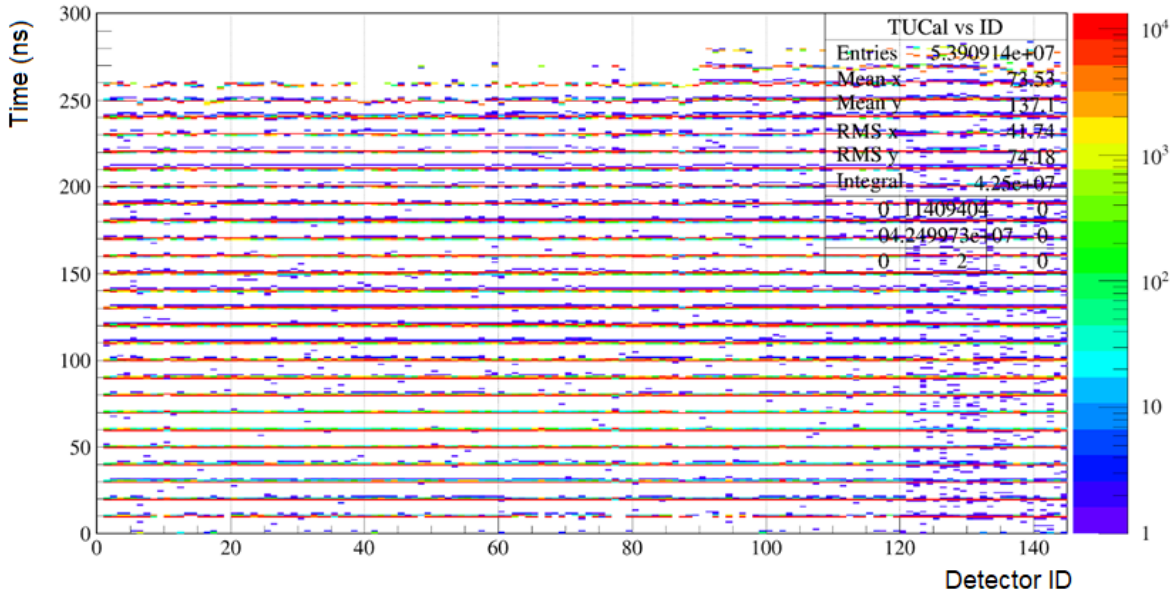

Figure B.4: The aligned pulses in NEBULA, separated by 10 ns produced by the pulser.

found using a peak detection algorithm, and then converted to real time. The result is shown in figure B.4.

B.2.7 Time of Flight of Neutrons

The construction of NEBULA uses 120 thick plastic scintillators, coupled to photomultiplier tubes at the top and bottom. Similarly the veto layers consist of two sets of 12 wider and thinner plastic scintillators coupled to photomultiplier tubes. As a result, in order to determine the time in a paddle, the average time is used, shown in equation B.10.

$$Time = \frac{T_{up} + T_{down}}{2} \tag{B.10}$$

Whilst the time has been converted from raw TDC signals to real time, using the pulser run, the time in a paddle is still not properly known. In order to determine the time, gamma rays are used. To do this high intensity gamma rays are generated by impinging a ^{15}C beam on to a thick aluminium target. This was performed in runs dayone0049-dayone0054. As the geometry of the SAMURAI spectrometer is known, the distance between the target and each individual NEBULA plastic paddle can be determined.

The interaction of this beam and target produces high intensity gamma rays and also neutrons. As the gamma rays travel at the speed of light, the distribution of the gamma peak will produce a sharp peak, which can be fitted using a gaussian peak. The neutrons that are also produced, will have a distribution of energies. As the velocity of the neutrons is related to the energy, this will produce a broad distribution of times for the neutrons. With

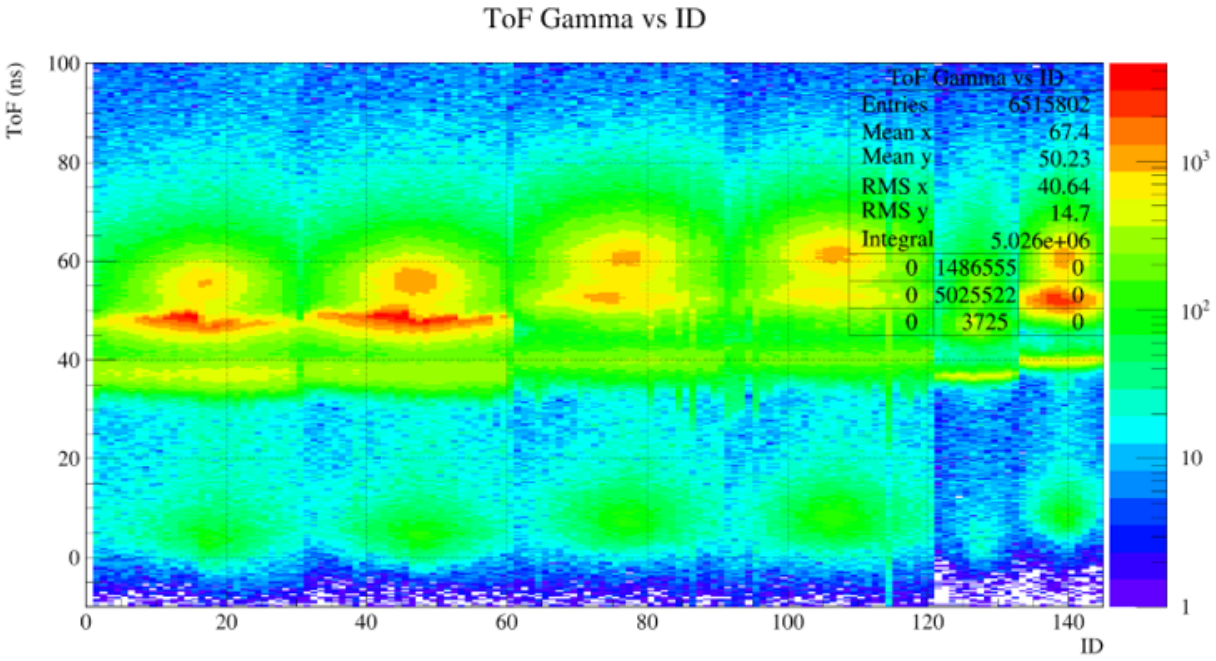

Figure B.5: The aligned time of flight in NEBULA.

this information, it is possible to determine the time of flight, which is done by taking the distance between the target and each NEBULA paddle, dividing by the speed of light and converting to nano seconds.

Taking the calibrated time, which initially is the pedestal time, the sharp gamma ray peak is fitted using a gaussian fit. With this the difference between this time, and the calculated time can be determined. This time difference is an offset that is then applied to get a calibrated time. The result of this calibration is shown in figure B.5, which shows a peak between 35-40 ns, which correspond to the time of flight of the gamma rays, while the broad distribution above 45 ns represent neutrons.

B.2.8 Position calibration

The position of neutrons in NEBULA is assumed to be in the center for the X position. Therefore the X position of neutrons is determined by the position of the paddle relative to the target, and therefore, as the paddles have a width of 12 cm, the X resolution is ± 6cm. The Y position of neutrons in NEBULA cannot however be assumed to be in the center of the paddle. This is because each paddle has a length of 1.8 m. As a result the Y position has to be determined using the difference in time between the PMTs at either end of the paddle. Using this, the Y position of the neutrons can be determined, knowing that T_{up}=T_{down} corresponds to the center of the paddle, and the limits of the time corresponds to the extreme limits of the paddle, ± 900 mm. Knowing this, the Y position can be determined from the

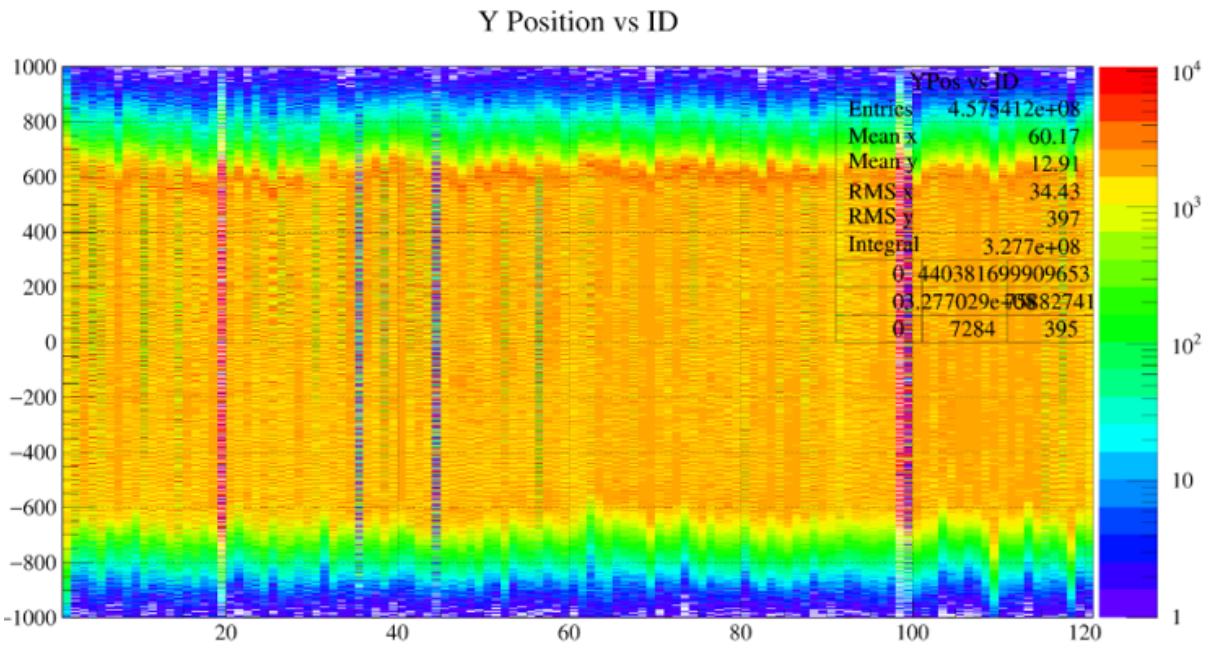

Figure B.6: The Y Position of events within NEBULA.

time of the neutrons in the paddles, which is shown in figure B.6.

Appendix C

C.1 DALI2 Additional Analysis

C.1.1 Addback Analysis

Addback analysis is a technique used to improve the detection efficiency. This is because there are three ways that a gamma ray can deposit energy within a crystal, and these processes compete with each other. The first process in which a gamma ray can deposit energy is the photoelectric effect, which is dominant at low energies (<500 keV). In the photoelectric effect, an electron gains kinetic energy, equal to the energy of the photon. This electron then deposits its energy within the crystal, emitting light which is measured by the photomultiplier tube. The second process in which a gamma ray can deposit energy is compton scattering. This process is similar to the photoelectric effect, however instead of depositing all of the photons energy into the electron, it only deposits part of the energy. The scattered photon can then go on to have further interactions, possibly in other crystals. It is also possible that the scattered gamma ray will leave DALI2 without further interactions. The final interaction method is pair production, which occurs when the incoming gamma ray has an energy greater than 1022 keV, which is twice the rest mass of an electron (511 keV). In pair production, an electron positron pair is created. When this happens, the positron will annihilate with an electron. This then results in two 511 keV photons being produced, after which there are three possible outcomes. The first situation is that both 511 keV gamma rays are detected, the second is that only one 511 keV photon is detected, so the energy observed is proportional to the incoming photon minus 511 keV. The final situation is where none of the 511 keV photons are observed, so the energy observed is proportional to the incoming photon minus 1022 keV.

In the case of DALI2, for 1 MeV γ rays, with a β of 0.5, the detection efficiency can be improved by 30% [55]. The principle used to produce this increase in detection efficiency is that for an incoming γ ray, most of the energy will be deposited within an initial detector, but subsequent Compton scattered events will then be detected in nearby detectors. This

cluster of events is then used to determine the add backed energy. To do this, the sum of the energies in the laboratory frame is taken, and then from this the detector with the highest energy is then used to get the angle information for the Doppler correction. In the code, a cluster is defined as any crystal within a 20 cm range of the detector with the highest energy deposited.

The method used to show the addback method is shown in figure C.1. As discussed earlier, when a reaction product passes through DALI2, it may emit one or more gamma rays. Each gamma ray may deposit all of the energy in a single crystal. However it is also possible for a gamma ray to only deposit part of its energy in a crystal, with processes such as compton scattering resulting in other nearby crystals being triggered. In the analysis, all the triggered detectors are found, and the triggered detectors are sorted from highest to lowest energy. The crystals within 20 cm of the highest energy detector are then identified. If any of the triggered detectors are within this 20 cm range, then the energy is added to the energy of the crystal with the highest energy. If there are crystals that are left over after the addback analysis, the process is repeated with the remaining triggered detectors until the crystals have been added together or identified as only interacting with a single crystal.

Figure C.2 shows the effect of the addback for ^{88}Y calibration source that was used. It shows that there is a clear increase in the number of counts. The effect can also be seen for the beam data, shown in figure C.3. Table C.1 shows the percentage change in the integral of the peaks for different sources. Using this information, the percentage increase with this data at 1 MeV is expected to be 9.26%, and for the beam data, the percentage increase at 1600 keV is expected to be 25.22%.

Source	Original Counts	Addback Counts	Percentage increase
^{22}Na 511 keV	4464254	4090793	-8.37%
^{88}Y 898 keV	1717656	2050109	19.36%
^{22}Na 1274 keV	1367624	1450021	6.02%
^{88}Y 1836 keV	1047842	1401922	33.79%

Table C.1: The change in the integral of the peaks when comparing the original energy to the addback energy.

C.1.2 DALI2 Simulation Verification - Addback

As seen in section 4.4.4, it is important to verify the simulation works for addback analysis. This was done following the same method previously used, and again the ^{88}Y source and simulation is used, with an energy threshold of 300 keV and an addback range of 20 cm. The fitting can be seen in figure C.4.

Again the P0 value, representing the scaling of the ^{88}Y simulation is approximately one,

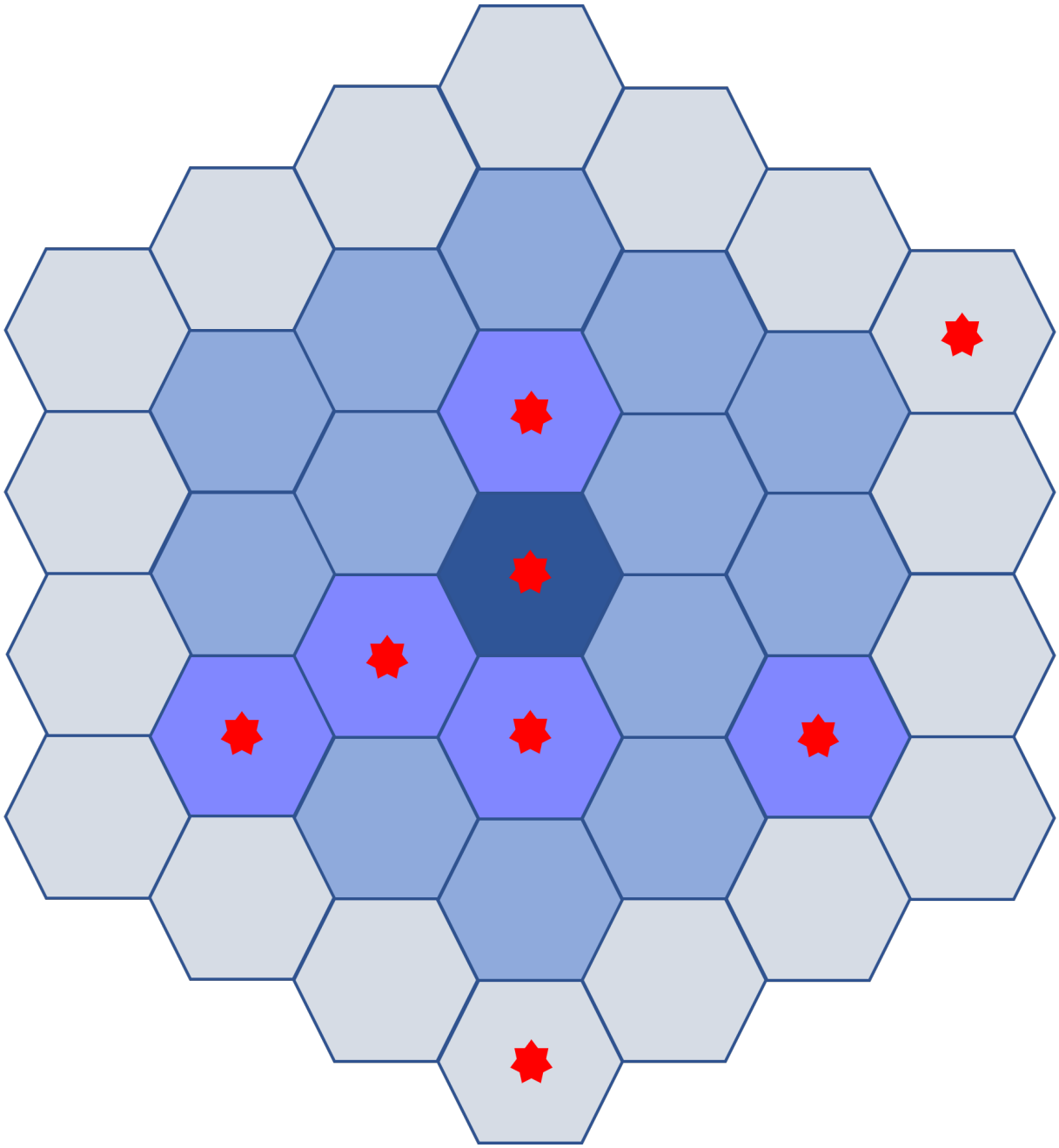

Figure C.1: In this figure, the darkest blue hexagon in the centre represents the crystal hit by the gamma ray with the highest energy deposited. All crystals which record a hit have a red star. The lighter shaded blue hexagon represent crystals within a 20 cm range of the central hit crystal. The grey hexagons represent crystals outside of the 20 cm range from the central crystal. Note that the setup does not use hexagonal crystals as shown, however this figure has been drawn to demonstrate clearly how this method works.

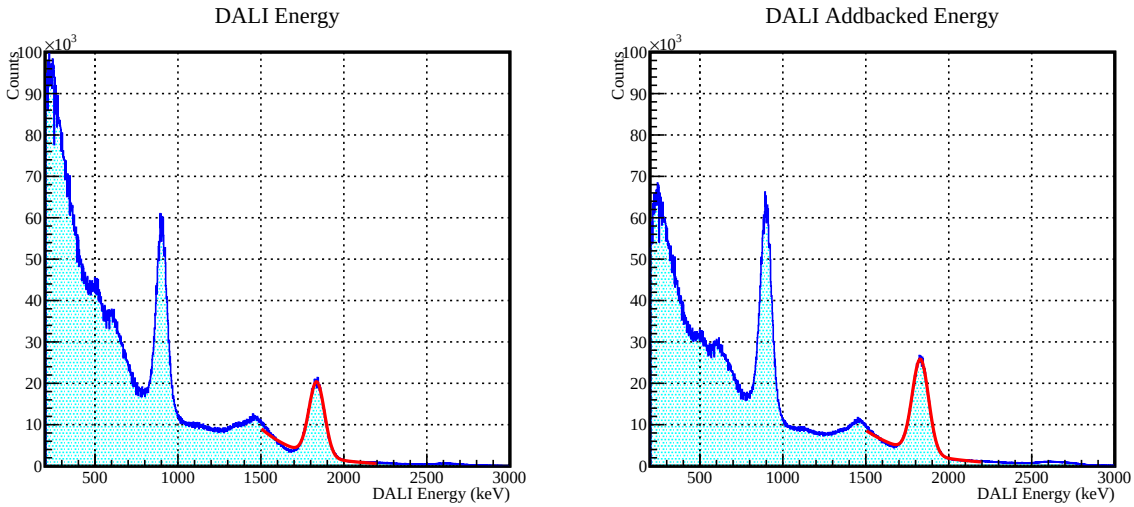

Figure C.2: The left panel shows the energy spectrum for an ^{88}Y source, while the right panel shows the addbacked energy spectra for ^{88}Y. It can be seen that there is an increase in counts for the peaks, while the number of counts at low energy decreases.

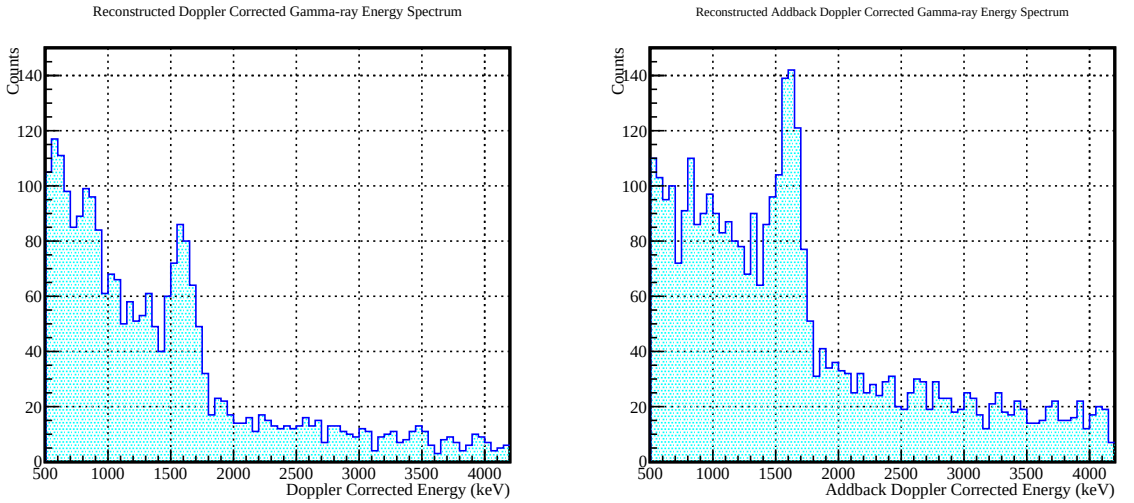

Figure C.3: The left panel shows the Doppler corrected energy spectrum for the ^{20}C fragments, while the right panel shows the addbacked Doppler corrected energy spectra for ^{20}C. It can be seen that there is an increase in counts for the gamma ray produced by the decay of the 2^+ state, while the number of counts at low energy decreases.

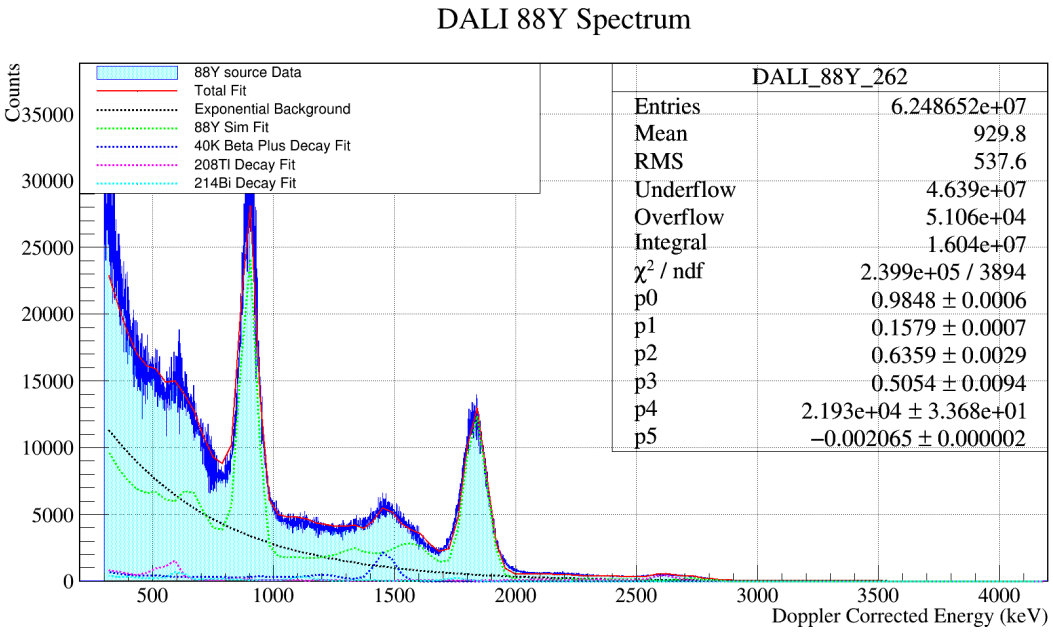

Figure C.4: The fitting of the addback energy from an ^{88}Y source, placed at the target position within DALI2 using a GEANT4 simulated response.

with a value of 0.9848±0.0007, within the uncertainty of the source. Therefore the simulation can be verified for the addback case in the case of stationary sources.

Bibliography

[1] J. J. Thomson, "On the structure of the atom: an investigation of the stability and periods of oscillation of a issue of corpuscles arranged at equal intervals around the circumference of a circle; with application of the results to the theory of atomic structure," *The London, Edinburgh, and Dublin Philosophical Magazine and Journal of Science*, vol. 7, pp. 237–265, 1904. [Online]. Available: https://doi.org/10.1080/14786440409463107

[2] E. Rutherford, "The Scattering of alpha and beta Particles by Matter and the Structure of the Atom," *Philosophical Magazine*, vol. 21, pp. 669–688, 1911. [Online]. Available: https://doi.org/10.1080/14786440508637080

[3] ——, "Collision of alpha particles with light atoms iii. nitrogen and oxygen atoms," *The London, Edinburgh, and Dublin Philosophical Magazine and Journal of Science*, vol. 37, pp. 571–580, 1919. [Online]. Available: https://doi.org/10.1080/14786440608635918

[4] ——, "Bakerian lecture: Nuclear constitution of atoms," *Proceedings of the Royal Society of London. Series A, Containing Papers of a Mathematical and Physical Character*, vol. 97, pp. 374–400, 1920. [Online]. Available: https://doi.org/10.1098/rspa.1920.0040

[5] W. Bothe and H. Becker, "Künstliche Erregung von Kern-γ-Strahlen," *Zeitschrift für Physik*, vol. 66, pp. 289–306, 1930. [Online]. Available: https://doi.org/10.1007/BF01390908

[6] J. Chadwick, "Bakerian lecture: The neutron," *Proceedings of the Royal Society of London. Series A, Containing Papers of a Mathematical and Physical Character*, vol. 142, pp. 1–25, 1933. [Online]. Available: https://doi.org/10.1098/rspa.1933.0152

[7] K. S. Krane, *Introductory Nuclear Physics*. Wiley, 2005.

[8] R. D. Woods and D. S. Saxon, "Diffuse surface optical model for nucleon-nuclei scattering," *The Physical Review*, vol. 95, pp. 577–578, 1954. [Online]. Available: https://doi.org/10.1103/PhysRev.95.577

[9] M. Mayer, "On Closed Shells in Nuclei," *The Physical Review*, vol. 74, pp. 235–239, 1948. [Online]. Available: https://doi.org/10.1103/PhysRev.74.235

[10] T. Otsuka, A. Gade *et al.*, "Evolution of shell structure in exotic nuclei," *Reviews of Modern Physics*, vol. 92, p. 015002, 2020. [Online]. Available: https://doi.org/10.1103/RevModPhys.92.015002

[11] "Nuclear Force between two nucleons calculated using the Reid potential by Bdushaw," url = " https://commons.wikimedia.org/wiki/File:ReidPotential.jpg/media/File:ReidPotential.jpg", accessed: 2023-01-03.

[12] M. Thoennessen, "Reaching the limits of nuclear stability," *Reports on Progress in Physics*, vol. 67, pp. 1187–1232, 2004. [Online]. Available: https://doi.org/10.1088/0034-4885/67/7/R04

[13] M. Pfützner, M. Karny, L. V. Grigorenko, and K. Riisager, "Radioactive decays at limits of nuclear stability," *Reviews of Modern Physics*, vol. 84, pp. 567–619, 2012. [Online]. Available: https://doi.org/10.1103/RevModPhys.84.567

[14] M. Wang, G. Audi, F. G. Kondev, W. J. Huang, S. Naimi, and X. Xu, "The AME2016 atomic mass evaluation (II). Tables, graphs and references," *Chinese Physics C*, vol. 41, p. 030003, 2017. [Online]. Available: https://doi.org/10.1088/1674-1137/41/3/030003

[15] X. X. Sun, J. Zhao, and S. G. Zhou, "Study of ground state properties of carbon isotopes with deformed relativistic Hartree-Bogoliubov theory in continuum," *Nuclear Physics A*, vol. 1003, p. 122011, 2020. [Online]. Available: https://doi.org/10.1016/j.nuclphysa.2020.122011

[16] P. G. Thirolf, B. V. Pritychenko *et al.*, "Spectroscopy of the 2_1^+ state in ^{22}O and shell structure near the neutron drip line," *Physics Letters B*, vol. 485, pp. 16–22, 2000. [Online]. Available: https://doi.org/10.1016/S0370-2693(00)00720-6

[17] M. Stanoiu, F. Azaiez *et al.*, "Study of drip line nuclei through two-step fragmentation," *European Physical Journal A*, vol. 20, pp. 95–96, 2004. [Online]. Available: https://doi.org/10.1140/epja/i2002-10329-8

[18] M. Stanoiu, D. Sohler *et al.*, "Disappearance of the N=14 shell gap in the carbon isotopic chain," *Physical Review C*, vol. 78, p. 034315, 2008. [Online]. Available: https://doi.org/10.1103/PhysRevC.78.034315

[19] D. Sohler, M. Stanoiu *et al.*, "In beam γ-ray spectroscopy of the neutron-rich nitrogen isotopes $^{19-22}$N," *Physical Review C*, vol. 77, pp. 1–8, 2008. [Online]. Available: https://doi.org/10.1103/PhysRevC.77.044303

[20] A. H. Wuosmaa, B. B. Back *et al.*, "^{15}C$(d,p)^{16}$C Reaction and Exotic Behavior in ^{16}C," *Physical Review Letters*, vol. 105, p. 132501, 2010. [Online]. Available: https://doi.org/10.1103/PhysRevLett.105.132501

[21] S. Fujii, T. Mizusaki *et al.*, "Microscopic shell-model description of the exotic nucleus ^{16}C," *Physics Letters B*, vol. 650, pp. 9–14, 2007. [Online]. Available: https://doi.org/10.1016/j.physletb.2007.04.067

[22] W. Horiuchi and Y. Suzuki, "Structure of and E2 transition in ^{16}C in a ^{14}C+n+n model," *Physical Review C*, vol. 73, p. 037304, 2006. [Online]. Available: https://doi.org/10.1103/PhysRevC.73.037304

[23] K. Hagino and H. Sagawa, "Three-body model calculations for the ^{16}C nucleus," *Physical Review C*, vol. 75, p. 021301, 2007. [Online]. Available: https://doi.org/10.1103/PhysRevC.75.021301

[24] D. T. Tran, H. J. Ong *et al.*, "Evidence for prevalent Z = 6 magic issue in neutron-rich carbon isotopes," *Nature Communications*, vol. 9, pp. 1–7, 2018. [Online]. Available: https://doi.org/10.1038/s41467-018-04024-y

[25] D. R. Tilley, H. R. Weller *et al.*, "Energy levels of light nuclei a = 16-17," *Nuclear Physics, Section A*, vol. 564, pp. 1–183, 1993. [Online]. Available: https:doi.org/10.1016/0375-9474(93)90073-7

[26] F. Ajzenberg-Selove, "Energy levels of light nuclei A = 13-15," *Nuclear Physics A*, vol. 523, pp. 1–196, 1991. [Online]. Available: https:doi.org/10.1016/0375-9474(91)90446-D

[27] H. J. Ong, N. Imai *et al.*, "Lifetime measurements of first excited states in ^{16,18}C," *Physical Review C*, vol. 78, p. 014308, 2008. [Online]. Available: https://doi.org/10.1103/PhysRevC.78.014308

[28] S. Terashima, I. Tanihata *et al.*, "Proton radius of ^{14}Be from measurement of charge-changing cross sections," *Progress of Theoretical and Experimental Physics*, vol. 2014, 2014. [Online]. Available: https://doi.org/10.1093/ptep/ptu134

[29] A. Estradé, R. Kanungo *et al.*, "Proton radii of $^{12-17}$B define a thick neutron surface in ^{17}B," *Physical Review Letters*, vol. 113, p. 132501, 2014. [Online]. Available: https://doi.org/10.1103/PhysRevLett.113.132501

[30] R. Kanungo, W. Horiuchi *et al.*, "Proton Distribution Radii of $^{12-19}$C Illuminate Features of Neutron Halos," *Physical Review Letters*, vol. 117, p. 102501, 2016. [Online]. Available: https://doi.org/10.1103/PhysRevLett.117.102501

[31] D. T. Tran, H. J. Ong *et al.*, "Charge-changing cross-section measurements of $^{12-16}$C at around 45A MeV and development of a Glauber model for incident energies 10A-2100A MeV," *Physical Review C*, vol. 94, p. 064604, 2016. [Online]. Available: https://doi.org/10.1103/PhysRevC.94.064604

[32] A. O. Macchiavelli, M. Petri *et al.*, "Phenomenological analysis of $B(E2)$ transition strengths in neutron-rich carbon isotopes," *Physical Review C*, vol. 90, p. 067305, 2014. [Online]. Available: https://doi.org/10.1103/PhysRevC.90.067305

[33] I. Syndikus, M. Petri *et al.*, "Probing the Z = 6 spin-orbit shell gap with (p,2p) quasi-free scattering reactions," *Physics Letters B*, vol. 809, p. 135748, 2020. [Online]. Available: https://doi.org/10.1016/j.physletb.2020.135748

[34] A. Ozawa, O. Bochkarev *et al.*, "Measurements of interaction cross sections for light neutron-rich nuclei at relativistic energies and determination of effective matter radii," *Nuclear Physics A*, vol. 691, pp. 599–617, 2001. [Online]. Available: https://doi.org/10.1016/s0375-9474(01)00563-2

[35] N. Kobayashi, T. Nakamura *et al.*, "One- and two-neutron removal reactions from the most neutron-rich carbon isotopes," *Physical Review C*, vol. 86, p. 054604, 2012. [Online]. Available: https://doi.org/10.1103/PhysRevC.86.054604

[36] J. D. Stevenson and P. B. Price, "Production of the neutron-rich nuclides ^{20}C and ^{27}F by fragmentation of 213 MeV/nucleon ^{48}Ca," *Physical Review C*, vol. 24, pp. 2102–2105, 1981. [Online]. Available: https://doi.org/10.1103/PhysRevC.24.2102

[37] J. C. Jacmart, F. Pougheon *et al.*, "Measurement and QRPA Calculation of the β-delayed neutron emission of ^{21,22}N and ^{23,24}O," *Nuclear Physics A*, vol. 513, pp. 1–10, 1990. [Online]. Available: https://doi.org/10.1016/0375-9474(90)90338-M

[38] M. Petri, P. Fallon *et al.*, "Lifetime Measurement of the 2_1^+ state in ^{20}C," *Physical Review Letters*, vol. 107, p. 102501, 2011. [Online]. Available: https://doi.org/10.1103/PhysRevLett.107.102501

[39] G. Jansen, J. Engel, G. Hagen, P. Navratil, and A. Signoracci, "*Ab Initio* Coupled-Cluster Effective Interactions for the Shell Model: Application to Neutron-Rich Oxygen and Carbon Isotopes," *Physical Review Letters*, vol. 113, p. 142502, 2014. [Online]. Available: https://doi.org/10.1103/PhysRevLett.113.142502

[40] B. Brown, "Status Of The Nuclear Shell Model," *Annual Review of Nuclear and Particle Science*, vol. 38, pp. 29–66, 1988. [Online]. Available: https://doi.org/10.1146/annurev.nucl.38.1.29

[41] E. K. Warburton and B. A. Brown, "Effective interactions for the $0p1s0d$ nuclear shell-model space," *Physical Review C*, vol. 46, pp. 923–944, 1992. [Online]. Available: https://doi.org/10.1103/PhysRevC.46.923

[42] M. Petri, S. Paschalis *et al.*, "Structure of ^{16}C: Testing shell model and *ab initio* approaches," *Physical Review C*, vol. 86, p. 044329, 2012. [Online]. Available: https://doi.org/10.1103/PhysRevC.86.044329

[43] C. Yuan, T. Suzuki *et al.*, "Shell-model study of boron, carbon, nitrogen, and oxygen isotopes with a monopole-based universal interaction," *Physical Review C*, vol. 85, p. 064324, 2012. [Online]. Available: https://doi.org/10.1103/PhysRevC.85.064324

[44] C. Forssén, R. Roth *et al.*, "Systematics of 2^+ states in C isotopes from the no-core shell model," *Journal of Physics G: Nuclear and Particle Physics*, vol. 40, p. 055105, 2013. [Online]. Available: https://doi.org/10.1088/0954-3899/40/5/055105

[45] L. Coraggio, A. Covello *et al.*, "Fully microscopic shell-model calculations with realistic effective hamiltonians," *Journal of Physics: Conference Series*, vol. 312, p. 092021, 2011. [Online]. Available: https://doi.org/10.1088/1742-6596/312/9/092021

[46] Y. Kanada-En'yo, F. Kobayashi *et al.*, "Cluster and deformation in carbon isotopes," *AIP Conference Proceedings*, vol. 1491, pp. 5–9, 2012. [Online]. Available: https://doi.org/10.1063/1.4764190

[47] Y. Kanada-En'Yo, "Proton radii of Be, B, and C isotopes," *Physical Review C*, vol. 91, p. 014315, 2015. [Online]. Available: https://doi.org/10.1103/PhysRevC.91.014315

[48] G. Thiamova, N. Itagaki *et al.*, "Systematic analysis of neutron-rich carbon isotopes," *Nuclear Physics A*, vol. 719, pp. 312–315, 2003. [Online]. Available: https://doi.org/10.1016/S0375-9474(03)00939-4

[49] J. W. Hwang, S. Kim *et al.*, "Single-neutron knockout from ^{20}C and the structure of ^{19}C," *Physics Letters, Section B*, vol. 769, pp. 503–508, 2017. [Online]. Available: http://doi.org/10.1016/j.physletb.2017.04.019

[50] T. Kubo, D. Kameda *et al.*, "BigRIPS separator and ZeroDegree spectrometer at RIKEN RI Beam Factory," *Progress of Theoretical and Experimental Physics*, vol. 2012, 2012. [Online]. Available: https://doi.org/10.1093/ptep/pts064

[51] T. Ohnishi, T. Kubo *et al.*, "Identification of New Isotopes ^{125}Pd and ^{126}Pd Produced by In-Flight Fission of 345 MeV / nucleon ^{238}U: First Results from the RIKEN RI Beam Factory," *Journal of the Physical Society of Japan*, vol. 77, p. 083201, 2008. [Online]. Available: https://doi.org/10.1143/JPSJ.77.083201

[52] T. Kobayashi, N. Chiga *et al.*, "SAMURAI spectrometer for RI beam experiments," *Nuclear Instruments and Methods in Physics Research, Section B: Beam Interactions with Materials and Atoms*, vol. 317, pp. 294–304, 2013. [Online]. Available: http://doi.org/10.1016/j.nimb.2013.05.089

[53] H. Sato, T. Kubo *et al.*, "Superconducting Dipole Magnet for SAMURAI Spectrometer," *IEEE Transactions on Applied Superconductivity*, vol. 23, p. 4500308, 2013. [Online]. Available: https://doi.org/10.1109/TASC.2012.2237225

[54] S. Kim, "Spectroscopy of ^{17}C via one-neutron knockout reaction," Ph.D. dissertation, Seoul National University, 2015.

[55] S. Takeuchi, T. Motobayashi *et al.*, "DALI2: A NaI(Tl) detector array for measurements of γ rays from fast nuclei," *Nuclear Instruments and Methods in Physics Research, Section A: Accelerators, Spectrometers, Detectors and Associated Equipment*, vol. 763, pp. 596–603, 2014. [Online]. Available: https://doi.org/10.1016/j.nima.2014.06.087

[56] "Samurai day-one logbook 1," *Unpublished*, p. 1, 2012.

[57] C. Santamaria, "Quest for new nuclear magic numbers with MINOS," Ph.D. dissertation, UNIVERSITÉ PARIS-SUD XI, 2015.

[58] P. Doornenbal, "In-beam gamma-ray spectroscopy at the RIBF," *Progress of Theoretical and Experimental Physics*, vol. 2012, 2012. [Online]. Available: https://doi.org/10.1093/ptep/pts076

[59] F. Ajzenberg-Selove, "Energy levels of light nuclei A = 18-20," *Nuclear Physics A*, vol. 475, pp. 1–198, 1987. [Online]. Available: https://doi.org/10.1016/0375-9474(87)90205-3

[60] M. Wang, G. Audi *et al.*, "The Ame2012 atomic mass evaluation," *Chinese Physics C*, vol. 36, no. 12, p. 1603, 2012. [Online]. Available: https://doi.org/10.1088/1674-1137/36/12/003

[61] M. A. Firestone, J. Janecke *et al.*, "The ^{16}O(d,^{3}He)^{15}N reaction at 29 MeV: Reaction mechanism and nuclear structure," *Nuclear Physics A*, vol. 258, pp. 317–340, 1976. [Online]. Available: https://doi.org/10.1016/0375-9474(76)90009-9

[62] M. Wiedeking, P. Fallon *et al.*, "Lifetime measurement of the first excited 2^+ state in ^{16}C," *Physical Review Letters*, vol. 100, p. 152501, 2008. [Online]. Available: https://doi.org/10.1103/PhysRevLett.100.152501

[63] T. Wakasa, K. Ogata, and T. Noro, "Proton-induced knockout reactions with polarized and unpolarized beams," 2017. [Online]. Available: https://doi.org/10.1016/j.ppnp.2017.06.002

[64] R. F. Casten, *Nuclear Structure From A Simple Perspective*. Oxford University Press, 1990.

[65] I. J. Syndikus, "Proton-Knockout Reactions from Neutron-Rich N Isotopes," Ph.D. dissertation, Technische Universitat Darmstadt, 2018.

[66] J. Hwang, "Study of 19 C by One-Neutron Knockout Reaction with a Carbon Target," Ph.D. dissertation, College of Natural Sciences, Seoul National University, 2015.

[67] A. Gerrard and J. M. Burch, *Introduction to matrix methods in optics*, 1st ed. Dover Publications, Inc., 1994, p. 28–29.

[68] E. Süli and D. F. Mayers, *An introduction to numerical analysis*. Cambridge: Cambridge University Press, 2003, p. 328.

[69] P. Doornenbal, "Manual of a GEANT4 Simulation Code for γ -Ray Detectors used in the RIKEN-RIBF Facility," 2011.

[70] "Sunflower Collaboration γ sources in RIBF," url = " https://www.nishina.riken.jp/collaboration/SUNFLOWER/misc/util/rarfsource.php", accessed: 2022-08-08.

[71] N. N. D. C. B. N. Laboratory, "Nudat (nuclear structure and decay data)," March 18, 2008.

[72] "SBT DayOne Electronics Scheme," url = " http://be.nucl.ap.titech.ac.jp/ smdayone/moin.cgi/Materials?action=AttachFiledo=view target=SBT_DAYONE_ElectronicScheme.pdf", accessed: 2022-08-08.

[73] "HODOSCOPE DayOne Electronics Scheme," url = " http://be.nucl.ap.titech.ac.jp/ smdayone/moin.cgi/Materials?action=AttachFiledo=view target=Hodoscope_%28s008%29_ElectronicScheme.pdf", accessed: 2022-08-08.

[74] "DALI2 DayOne Electronics Scheme," url = " http://be.nucl.ap.titech.ac.jp/ smdayone/moin.cgi/Materials?action=AttachFiledo=view target=DALI2_DAYONE_ElectronicScheme.pdf", accessed: 2022-08-08.

[75] “NEBULA DayOne Electronics Scheme,” url = "
http://be.nucl.ap.titech.ac.jp/ smdayone/moin.cgi/Materials?action=AttachFiledo=view
target=NEBULA_DAYONE_ElectronicScheme.pdf", accessed: 2022-08-08.

[76] “Strobe DayOne Electronics Scheme,” url = "
http://be.nucl.ap.titech.ac.jp/ smdayone/moin.cgi/Materials?action=AttachFiledo=view
target=STROBE_DAYONE_ElectronicScheme.pdf", accessed: 2022-08-08.

[77] B. M. Godoy, “Structure and neutron decay of the unbound Beryllium isotopes 15,16Be,” Ph.D. dissertation, Université de Caen Normandie, 2019.